Quantitative Interpretation of Magnetic Field Measurements in Eddy Current Defect Detection

Anthony Simm

A thesis submitted for the degree of Doctor of Philosophy

School of Electrical and Electronic Engineering

Newcastle University

December 2012

Abstract

For many years, the theoretical and experimental study of eddy current non-destructive evaluation (NDE) has been conducted separately, as most models were not suited to practical industrial applications. The aim of this work is to bridge this gap by investigating the relationship between magnetic fields and defects using both modelling and experimental study and to link these results to quantitative NDE.

In this work, 3D FEM numerical simulations are used to predict the response of an eddy current probe being scanned over the area of a defect and understand the underlying change in magnetic field due to the presence of the defect.

Experimental investigations are performed to study the feasibility of the proposed magnetic field measurement techniques for defect detection. This experimental work investigates the inspection of both surface and subsurface defects, the use of rectangular (directional) probes and the measurement of complex magnetic field values, as the response in these cases has been found to have a greater correlation with the shape of the defect being studied.

As well as the detection of defects, both frequency spectrum and transient information from pulsed eddy current responses are used to reconstruct the profile (depth and width) of a slot shaped defect.

The work concludes that the use of magnetic field measurements provides useful information for defect detection and quantification. This will have applications in both industrial and research areas, including visualisation of defects from magnetic field measurements, which can be applied to the monitoring of safety critical components.

Acknowledgements

I would like to express my gratitude to the number of people who have helped me during my PhD study. Firstly, thanks to my supervisor Prof. Gui Yun Tian for supervising the work and his guidance throughout the project. I would also like to thank Assoc. Prof. Theodoros Theodoulidis of the University of Western Macedonia, Greece for his help and advice and giving me the opportunity to work with him (and Assoc. Prof. Nikolaos Poulakis) in Greece on a research visit.

I would like to thank the colleagues I have worked with during this research, Dr. Yong Li (now of Xi'an Jiaotong University, China), Dr Ilham Abidin (now of Malaysia Nuclear Agency), visitors to the group who I worked with, Dr Jingzhou Wang (Huaihai Institute of Technology, China), Dr Yating Yu (University of Electronics Science and Technology of China, China), Dr Yunze He (National University of Defense Technology, China) and all my other colleagues the Sensor Technology Research Group at Newcastle University for useful discussions and advice. I would also like to thank the technicians in the School of Electrical and Electronic Engineering for assistance with the experimental work.

I would like to thank the Engineering and Physical Sciences Research Council for financial support through EP/E010458/1 "Bridge the gap of theoretical and experimental eddy current NDT".

I dedicate this thesis to my parents and my brothers, for supporting me throughout my education.

Table of Contents

List of Figures

List of Tables

Nomenclature

Symbol	Quantity	Unit
$\overline{A}$	Magnetic Vector Potential	T/m
$\overline{B}$	Magnetic Flux Density	T
c	Speed of light $\left(2.998\times10^{-8}\right)$	m/s
$\overline{D}$	Electric Flux Density	C/m^2
$\overline{E}$	Electric Field	V/m
ε_0	Permittivity $\left(8.854\times10^{-12}\right)$	F/m
$\overline{H}$	Magnetic Field	A/m
$\bar{J}$	Current Density	A/m^2
L	Inductance	H
μ_0	Permeability of free space $\left(4\pi\times10^{-7}\right)$	H/m
μ_r	Relative Permeability	
μ	Permeability $\left(\mu_0\cdot\mu_r\right)$	H/m
σ	Conductivity	S/m
ω	Angular Frequency $\left(2\pi f\right)$	rad/s
R	Resistance	Ω
X_L	Inductive Reactance	Ω
Z	Impedance $\left(\sqrt{R^2+X_L^2}\right)$	Ω

List of Abbreviations

AMR	Anisotropic Magnetoresistive
EDM	Electro-Discharge-Machining
ENDE	Electromagnetic Non-destructive Evaluation
ETREE	Extended Truncated Region Eigenfunction Expansion
FEM	Finite Element Method
FFT	Fast Fourier Transform
GMR	Giant Magnetoresistive
ID	Inner Diameter
$\mathfrak{Im}$	Imaginary component
IFFT	Inverse Fast Fourier Transform
MFL	Magnetic Flux Leakage
MSE	Mean Squared Error
NDE	Non-destructive Evaluation
NDT	Non-destructive Testing
OD	Outer Diameter
PEC	Pulsed Eddy Current
QNDE	Quantitative Non-destructive Evaluation
$\mathfrak{Re}$	Real component
SQUID	Superconducting Quantum Interference Device
TREE	Truncated Region Eigenfunction Expansion

Chapter 1 Introduction

1.1 Chapter Introduction

This chapter gives an overview into the area of study, objectives, and an outline of the research work.

1.2 Background

Non-destructive evaluation (NDE)[1] has applications in many safety-critical industries. Established NDE technologies such as eddy current, ultrasonics, radiography and thermography have been extensively used over the past five decades. Although NDE is now a relatively mature field, increased safety expectations mean that there is a requirement for regular, low-cost accurate inspections, and that we should be able to detect sub-surface defects and defects with complex geometries.

Amongst all of the available NDE methods, electromagnetic NDE (ENDE) methods are the most common for the inspection of metallic components. This is based on the interaction of electromagnetic fields with the inspected conductive specimens. The electromagnetic methods include eddy current, pulsed eddy current (PEC) and magnetic flux leakage (MFL). These are useful in any application where we measure changes in electromagnetic properties of specimens, such as defect detection, conductivity measurement and thickness measurement.

One of the recent trends of NDE is the requirement for quantitative as well as qualitative assessment of materials. As we are evaluating the condition of the material, this is known as quantitative non-destructive evaluation (QNDE). Knowledge of quantitative defect information (size, shape, etc.) is useful in predicting the lifetime of the specimen under examination and monitoring its condition over time (i.e. Structural Health Monitoring). This is especially vital in monitoring safety critical components.

[1] There is some overlap in terminology in the literature. NDT is commonly used in industry; academia commonly uses NDE, which will be used throughout this thesis.

The use of simulation models, which allow the analysis of the electromagnetic fields within the NDE process, are useful in cooperation with experimental results (where experimental results are used to validate the modelling) and assist in the design of experiments (selection of probe types, excitation frequency, etc.). These models can broadly be classified as either analytical or numerical solutions to the Maxwell's equations [1]. In general, analytical models are limited to canonical geometries (cartesian, cylindrical or spherical) but are more computationally efficient and provide a closed-form solution to the problem (a closed-form solution can be expressed by elementary functions, such as arithmetic or logarithmic functions). Numerical models are more flexible and are not limited by geometry or material nonlinearities; however, they are slower than analytical models and give a numerical approximation, rather than an "exact" solution to the problem.

This work will use experimental magnetic field measurements and compare these with modelling results for ENDE. For magnetic field measurement, various sensor types can be used such as the Hall sensor or Giant Magnetoresistive (GMR) sensor. One drawback of these is the small sensing area, which has lead to the development of sensor arrays for magnetic field imaging. The sensor array gives simultaneous magnetic field measurements at different spatial points, which can be used to build up images of the magnetic field distribution.

1.3 Thesis Aims

The aim of this work is to bridge the gaps of theoretical (modelling) and experimental investigation of the eddy current NDE inspection process. Usually the study of theoretical and experimental methods in NDE has been separate, as industrial applications were concerned with the use of experimental methods, rather than modelling, plus available models were too simple to solve complex industrial problems. This project will combine modelling and experimental study, measuring the magnetic field response from an eddy current test, due to the presence of defects. Both single scans and area scans are used for improved defect visualisation (QNDE). Finite Element Method (FEM) numerical simulations are performed to acquire magnetic field distribution response due to the presence of a defect in the specimen under investigation.

The results of this study will be then be used to quantitatively evaluate (i.e. size and location) any defects present (defect reconstruction), bridging the gaps in NDE between

experiment design (forward problem) and the characterisation of materials (inverse problem), which will be achieved by.

1. Undertake Literature Survey

   Undertake a comprehensive literature survey on various NDE techniques and the numerical and analytical modelling of eddy current phenomena.

2. Modelling

   2D and 3D FEM simulations will be performed to study the interaction of eddy currents (and the resulting magnetic field) with defects (i.e. forward modelling). Analytical models based on Dodd and Deeds and the Truncated Region Eigenfunction Expansion (TREE) will be studied for PEC response and spatial field measurement.

3. Experimental studies of magnetic field response to defects.

   An experimental test setup will be developed, including coil excitation, *x*-*y* scanning system and data acquisition. A variety of experimental scenarios will be investigated: surface and subsurface defects, directional excitation and complex magnetic field measurements. This will link theoretical and experimental study in NDE.

4. Defect profile reconstruction from transient (PEC) eddy current measurements

   Transient and frequency spectrum measurements from the PEC response will be used to reconstruct the profile of slot shaped defects (width and height).

5. Dissemination of results

   The results of this work have been presented at university postgraduate conferences and international conferences in the fields of NDE and visualisation. Results from the experimental work have been published in academic peer reviewed journals.

1.4 Objectives

The objectives of the research are as follows.

1. Numerical and analytical modelling to simulate the eddy current NDE process.

   The FEM simulations will be used to predict the magnetic field response when a probe is scanned over a defect. The progression of work related to this field is shown in figure 1.1.

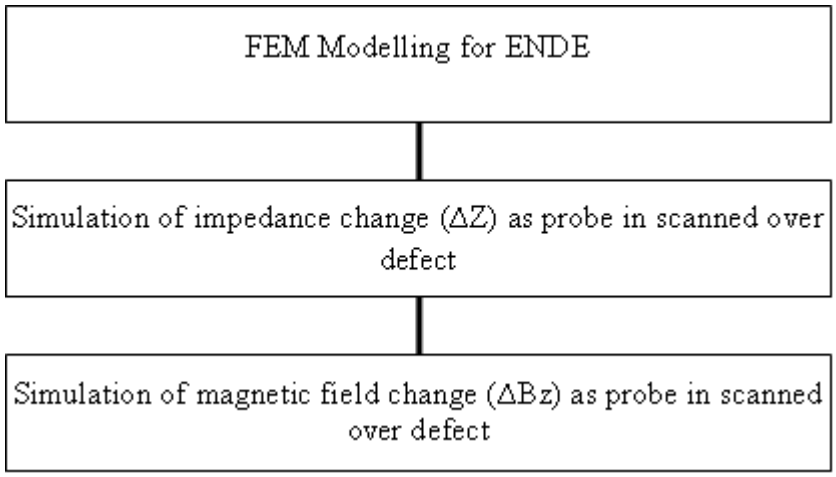

Figure 1.1 Study of numerical modelling in eddy current NDE

2. The Truncated Region Eigenfunction Expansion (TREE) method will be extended to predict the PEC response and measure the spatial magnetic field.

   The work in this area is shown in figure 1.2.

3. Experimental studies of magnetic field response to defects.

   This experimental investigation will be used to link the theoretical and experimental study in NDE. Two studies will be performed.

   a. Investigation of the magnetic field response to an artificial surface defect and subsurface defect (EDM slot) using a single scan.

   b. Investigation of the magnetic field response to an artificial (slot) defect, using both the real and imaginary components of the magnetic field measurements. The response using both a circular and rectangular (directional) probe will be compared.

The work in this area is shown in figure 1.3.

4. Defect profile reconstruction from transient (PEC) eddy current measurements.
    a. Reconstruction of defect profile from frequency spectrum response.
    b. Reconstruction of defect profile from transient response.

    The work in this area is shown in figure 1.4.

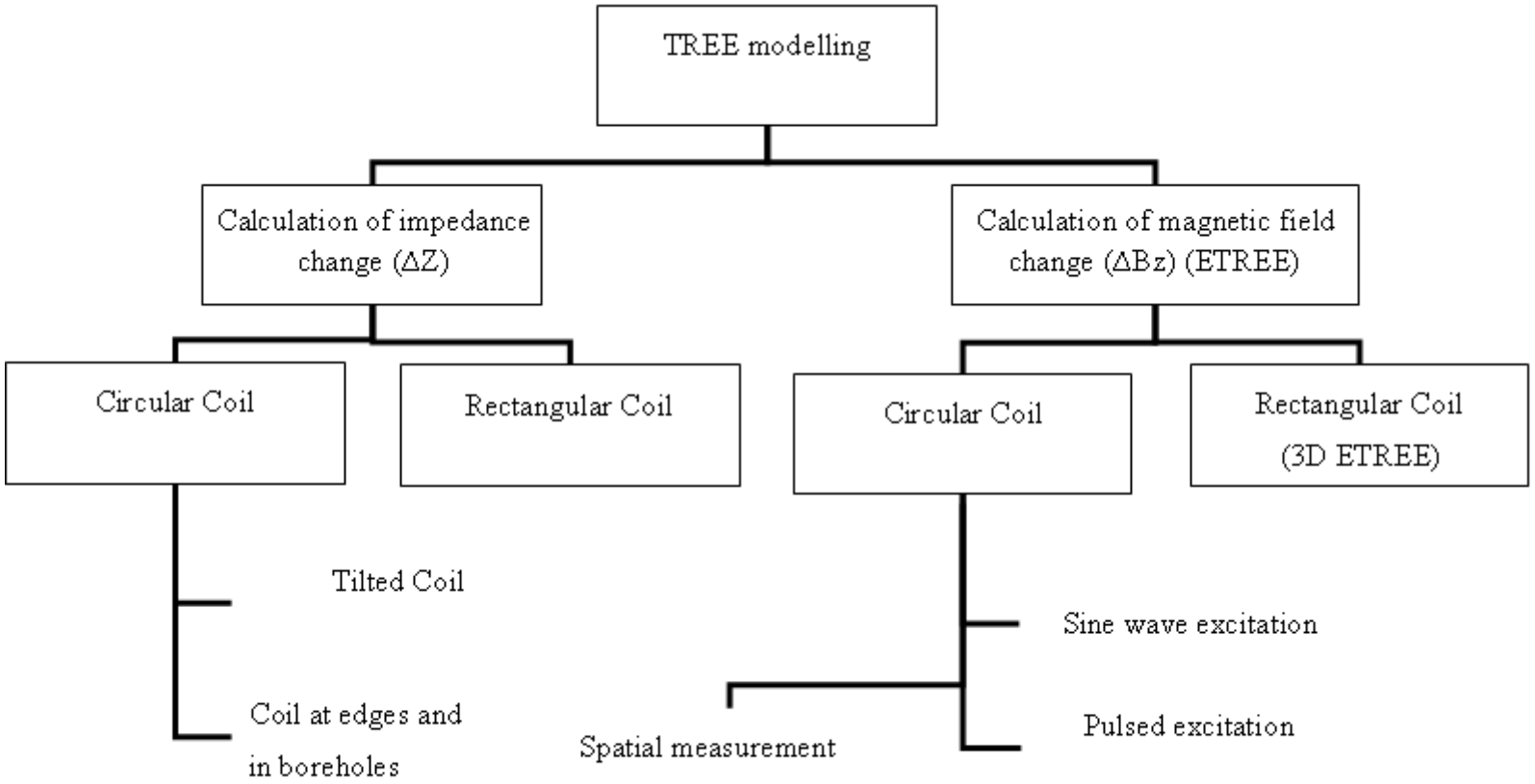

Figure 1.2 Study of TREE modelling

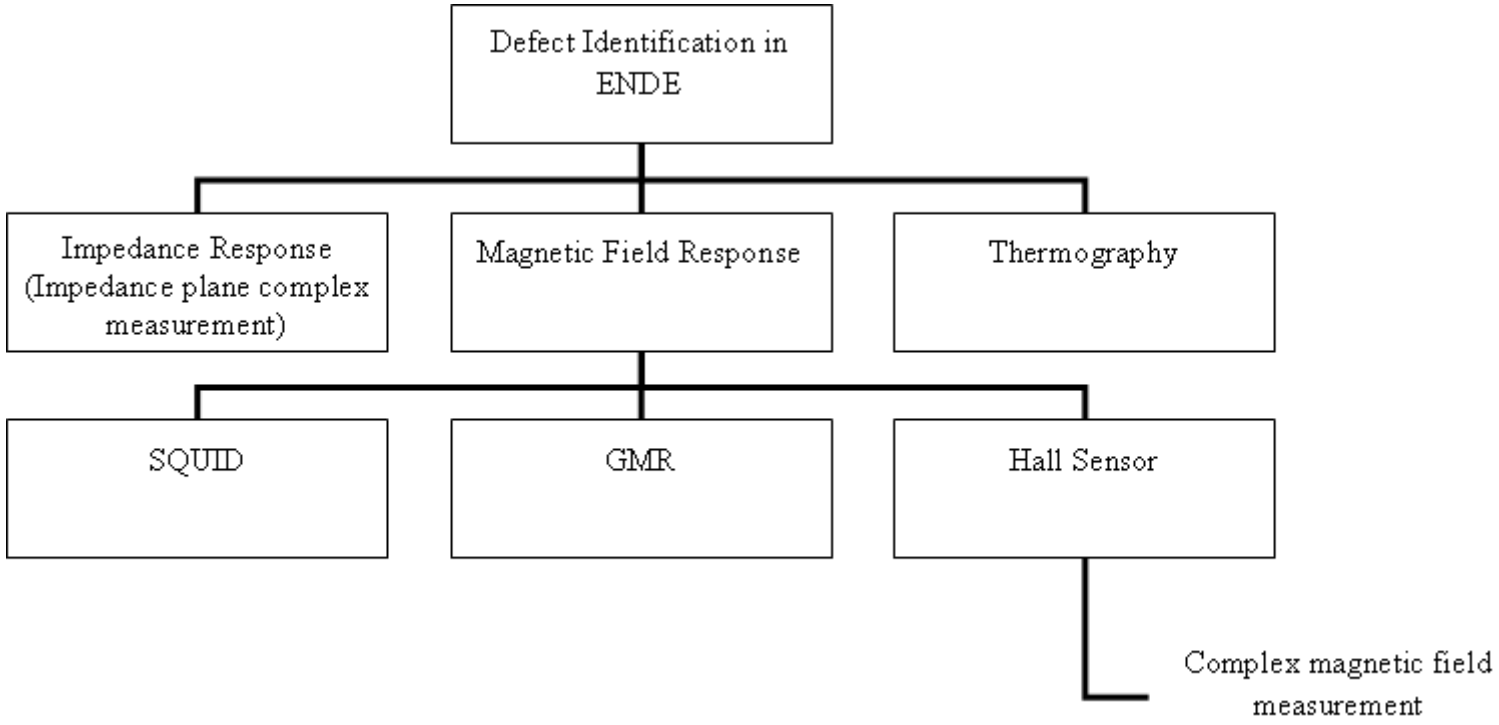

Figure 1.3 Study of defect identification in ENDE

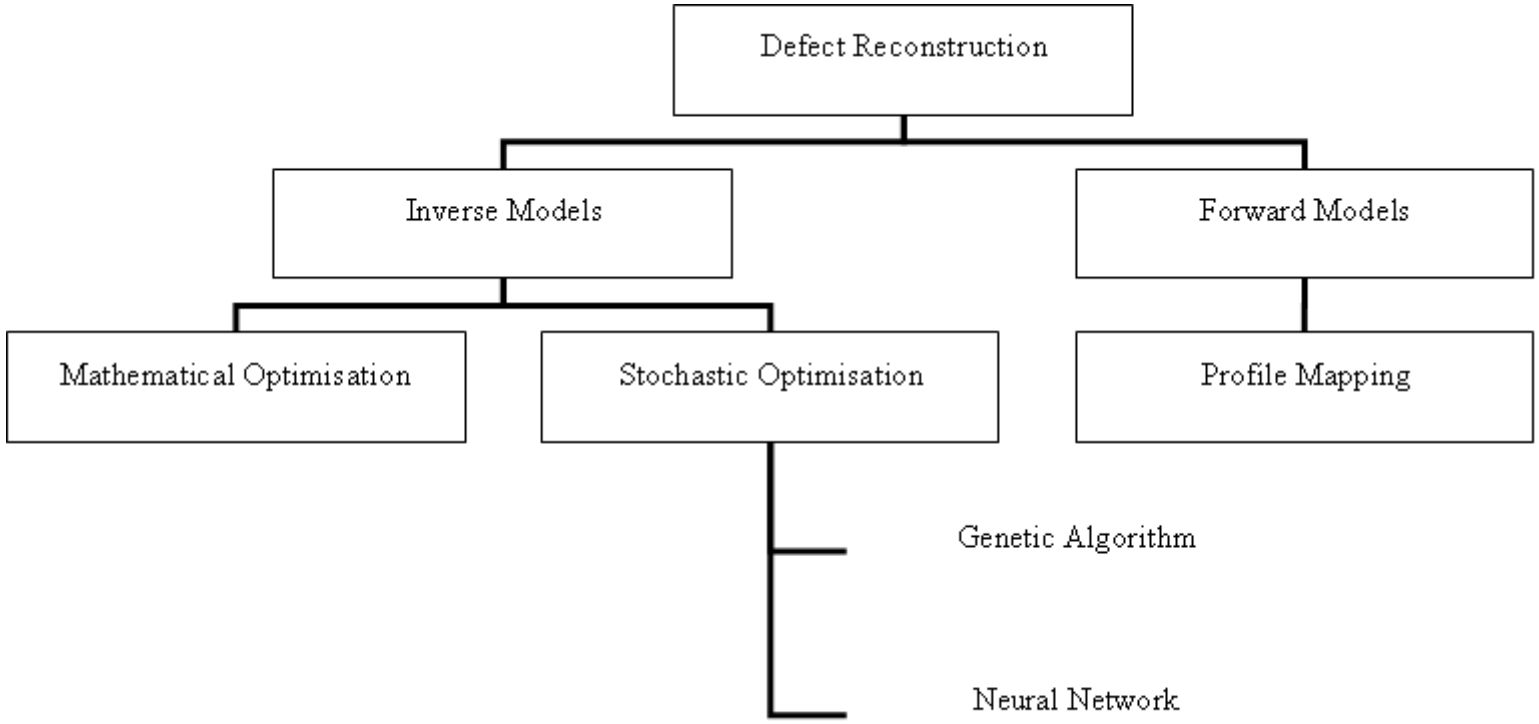

Figure 1.4 Study of defect reconstruction methods

1.5 Main Achievements

The main achievements (i.e. results of the research objectives) of the research work include (see **List of Publications** for details of the journal and conference publications referenced here).

1. Simulation and visualisation of eddy current NDE phenomena published in [J.1], [J.2] and [C.2].

2. Extension of TREE method for spatial field measurement, published in [C.1].

3. Investigation of the magnetic field response to defects through both FEM simulations and experimental work, published in [J.1] and [J.2]. The outcomes of this are.

    a. Provides an alternative to the existing impedance plane measurements where the magnetic field response is measured directly. The use of magnetic field measurements is common in eddy current NDE, however this is when pulsed excitation is used and the transient response measured.

    b. Magnetic field response provides a useful indication of the presence of both surface and subsurface defects. In an advance from measuring the amplitude of the magnetic field change due to the presence of a defect, the use of complex (real and imaginary) magnetic field measurements with a combination of circular and rectangular probes has also been investigated. These have been found to give improved correlation with the shape of the defect, especially when combined with directional excitation (using a rectangular excitation coil).

4. Mapping of magnetic field distribution for an eddy current probe experimentally using a sensor array and through modelling studies (analytical and numerical), published in [C.1].

5. Reconstruction of defect profiles using features from transient eddy current measurements. Information from the frequency spectrum response and the transient response has been used to reconstruct the profile (depth and width) of a simulated defect (slot).

1.6 List of Publications

The following publications have been produced during this research.

Journal Papers

[J.1] A. Simm and G. Y. Tian, "Investigation of directional eddy current complex measurements for defect mapping" *Insight - Non-Destructive Testing and Condition Monitoring,* vol. 52, pp. 320-325, June 2010.

[J.2] A. Simm, T. Theodoulidis, N. Poulakis, and G. Tian, "Investigation of the magnetic field response from eddy current inspection of defects" *The International Journal of Advanced Manufacturing Technology,* vol. 54, pp. 223-230, April 2011.

Conference Papers

[C.1] A. Simm, Y. Li, G. Y. Tian, and T. Theodoulidis, "Verification of an eddy current probe magnetic field" in *NDT 2008* Macclesfield, Cheshire, UK: The British Institute of Non-Destructive Testing, 2008.

[C.2] A. Simm, I. Z. Abidin, G. Y. Tian, and W. L. Woo, "Simulation and Visualisation for Electromagnetic Nondestructive Evaluation" in *14th International Conference Information Visualisation (IV)*, London, UK, 2010, pp. 515-520.

1.7 Benefits to the NDE Community

The benefits to the NDE community of the research findings are.

1. Experimental study to analyse the magnetic field distribution due to the presence of defects in conductive materials using complex magnetic field measurements and the use of directional excitation as an alternative to traditional impedance measurements;

2. Numerical modelling to predict the magnetic field signals from sensors, to develop an understanding of the interaction of the magnetic field with defects;

3. Reconstruction of defect profiles using PEC measurements (both transient and frequency spectrum);

This bridges the gap between experimental results and modelling through the increased understanding of the underlying electromagnetic phenomena, modelling for experimental design, the prediction of results and defect reconstruction, see figure 1.5.

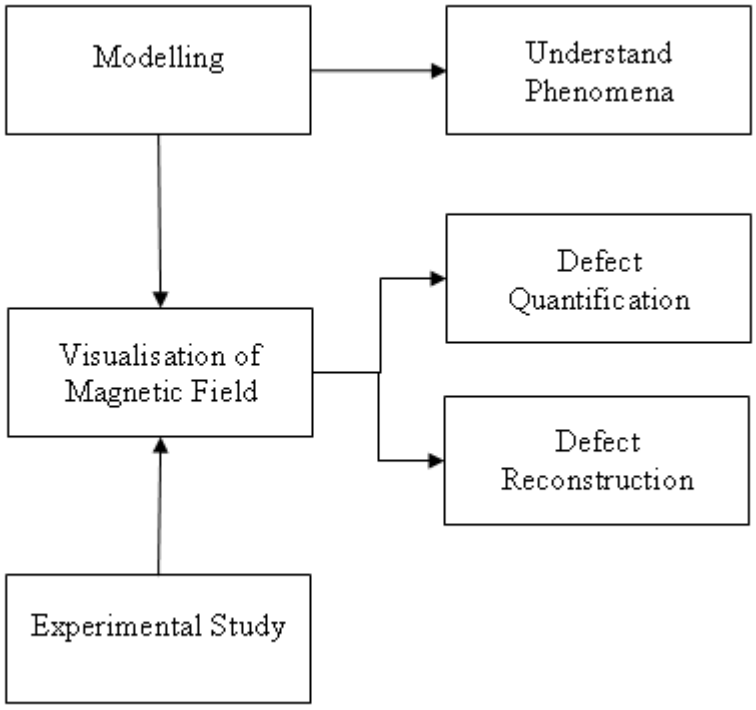

Figure 1.5 Bridge the gap between theoretical and experimental eddy current NDE

1.8 Thesis Layout

Chapter 2 reports the findings of the literature survey undertaken on eddy current NDE and defect modelling.

Chapter 3 presents an overview of common NDE techniques used in industry and academia, with emphasis on eddy current testing.

Chapter 4 details eddy current modelling methods, both numerical methods (Finite Element Method) and details the analytical modelling method proposed by Dodd and Deeds [2] and the Truncated Region Eigenfunction Expansion method proposed by Theodoulidis [3, 4].

Chapter 5 presents experimental results on the magnetic field response to defects. This compares simulation and experimental results for the purposes of defect characterisation. Further discussion also details the advantages of using a rectangular coil over circular coils. The use of sensor arrays for spatial magnetic field measurement and visualisation is also discussed

Chapter 6 reports on the application of PEC measurements to reconstruct the profile of a defect (slot width and height).

Chapter 7 outlines the conclusions drawn from the research work and gives recommendations for future work.

1.9 Chapter Summary

Numerical and analytical methods have been used to solve ENDE problems since the late 1960's, the improvements in computing power has allowed for the simulation of more complex industrial problems. This study aims to look at the problem of the magnetic field response to the presence of defects using modelling and experimental work and the interpretation of those results for defect QNDE.

Investigation of experimental results allows the user to gain an insight into the underlying physical properties of the problem, as is the case when complex magnetic field measurements are used. Forward models also allow the mapping between the defect profile and PEC measurement as a means to predict the profile of a defect based on measurements in the frequency or time domain. The use of models together with experimental results provides a useful mechanism in evaluating the magnetic field response to the presence of defects.

This chapter has introduced the research topic and the aims and objectives of the research and main achievements are presented. Finally, a layout of the thesis is given with contents of each chapter.

Chapter 2 Literature Survey

2.1 Chapter Introduction

This chapter will give an overview of eddy current NDE and the modelling techniques to describe the underlying phenomena.

2.2 Eddy Current NDE

Non-destructive inspection techniques are employed to examine an object without impairing its future usefulness. The most common application of NDE is to detect and characterise defects to assess the structural integrity of materials. To fulfil this need, eddy current based inspection has proved to be useful for the detection of surface and subsurface defects in various sectors of engineering, including transportation [5]; aerospace [6-8] and petrochemical [9] industries.

Eddy current NDE is based on inducing currents in the material being inspected and observing the interaction between the currents and the material, which can be monitored by measuring the impedance of the probe coil. When an alternating current is applied to the probe coil, a primary magnetic field is established in an axial direction around the coil. If the coil is bought near an electrically conductive specimen, the magnetic field interacts with the specimen, causing an electrical current (eddy current) to flow in the material. This current then creates its own secondary magnetic field, which opposes the probe coil's magnetic field. The interaction of the two magnetic fields can be measured using a magnetic sensor, such as a Hall sensor [10-15] or magnetoresistive sensors [16-19]. The use of these magnetic sensors, instead of conventional eddy current probe coils, is more useful at low excitation frequencies as the field is measured directly rather than the rate of change of the field (impedance).

The excitation frequency for eddy current testing is based on the material and the depth of the defects to be detected. The single frequency (sinusoidal) technique is widely used for surface and near surface defect detection. As well as single frequency, multi or swept frequency techniques, which can detect a range of defect depths, can be used. An

advance from this, the pulsed eddy current (PEC) technique, which uses a pulsed excitation, can be used to examine deep subsurface defects.

The trend in ENDE is the move from defect detection (qualitative evaluation) towards quantitative evaluation to estimate defect shape, type, size, and position [11, 20-22]. To enhance the inspection and improve the quantitative evaluation of defects, the sensors can be combined into arrays [10, 11, 14, 19, 23, 24]. These give improved information on the location and orientation of a defect through mapping of the spatial magnetic field distribution, thus improving the probability of detection over the use of a single sensor, although they can be limited by the spatial resolution of the sensor array.

The use of magnetic sensors for the imaging of magnetic field distribution is also possible by using scanning based systems for inspection [12, 25, 26]. The combination of positional information with field measurements allows the recording of an "image" of the field distribution due to the presence of a defect, which is useful in defect quantification. Although this can take a long time if scans over a large area are required.

2.3 Modelling in Eddy Current NDE

Modelling is often used in to simulate eddy current phenomena and the eddy current NDE process; this can also be combined with experimental study to provide an understanding of experimental results. This can also be used to predict the response of a probe for a given type of defect or experimental condition, where this can be useful for designing experiments, optimising inspections or generating "signatures" for defects, which can be used for defect quantification.

The electromagnetic phenomena are governed by a set of equations, called Maxwell's equations [1]. These determine the magnetic field at a point based on the source current density. These can be solved using two methods, analytical models or numerical models. In analytical models, the equation is solved by separation of variables. Analytical models can be used on axi-symmetric, 2D and 3D problems as long as the geometry is simple, i.e. restricted to canonical problems (planar/cartesian, cylindrical or spherical). These solutions can be applied to a range of similar problems (i.e. coil over layered conductor), and give an exact solution.

Numerical models also solve the Maxwell's equations; however, they are an approximation rather than an exact solution. These have the advantage that they are not restricted to simple geometries.

2.3.1 Analytical modelling

Analytical modelling provides a 'closed-form' solution to the governing partial differential equations, which are derived from Maxwell's equations for electromagnetic phenomena. This has advantages over numerical models in providing a fast and accurate solution to many electromagnetic problems.

The application of this approach began with the analytical model developed by Dodd and Deeds [2] in the 1960's for eddy current inspection of a two layered plate and the inspection of an infinitely long conducting rod. They represented the governing equations of eddy current inspection in cylindrical coordinates and solved them using separation of variables. Fourier-Bessel equations were used to simplify the problem and determine the magnetic vector potential. These models have been very useful and are still used today to predict eddy current response.

This disadvantage of the Dodd and Deeds model is that it is time-consuming to calculate due to the presence of infinite integrals. To overcome this, the Truncated Region Eigenfunction Expansion (TREE) method has been developed by Theodoulidis [3, 4]. Here, the domain of interest is truncated into a region of finite dimensions and consequently the solution is reformulated as a series, resulting in a considerably reduced computation time. The TREE method has been applied to several eddy current inspection scenarios, including inspection of a right angled conductive wedge [27], the edge of a conductive plate [28], finite length coils and rods [29] and analysing the magnetic field in multilayered structures [30].

The initial work for modelling was for intact specimens, now modelling the effect due to defects in a specimen will be discussed. The initial theoretical work for modelling discontinuities came in the work by Burrows [31]. This said that a small spherical discontinuity within a metal plate produces a field, which is the same as a small dipole. In this case, the defect must be small compared to the depth of penetration. Burrows then derived the induced emf in the coil due to the presence of the defect. This has been extended to represent an arbitrarily shaped defect using a current dipole distribution. Early work using this technique was in the field of geophysics, for example, the work

by Raiche [32, 33], subsequently this was applied to eddy current testing by Dunbar [34, 35], McKirdy [36] and Bowler *et al.* [37].

As well as the volume integral method, Bowler and his colleagues modelled the response to a defect (crack) with a width approaching zero (a barrier to current), the so-called 'ideal crack' [38], as well as reconstructing the crack shape from the measurement data [39]. The work by Dezhi [40], extended the work in [38] by taking into account the thickness of the specimen under inspection (finite thickness plate). The next stage was the 'thin-skin' model, where the skin depth is much smaller than the defect (crack) dimensions (so it is limited to inspection at high frequencies) and the eddy currents are concentrated near the surface of the specimen under inspection and close to the surface of the defect. This has been applied to rectangular cracks [41, 42], elliptically shaped cracks [43] and determining the defect (crack) shape from measurement data [44].

More recently, Theodoulidis *et al.* [45] used the boundary element method (BEM) in conjunction with the TREE method to calculate the impedance change due to a defect. He then extended this model for elliptic shaped cracks [46], where the Green's function calculation is improved by using the Matrix Pencil method [47].

2.3.2 Numerical modelling

Numerical models are in general more powerful than analytical models, due to the flexibility to model complex geometrical components and material nonlinearity. The result in this case is a numerical approximation, rather than a 'closed-form' solution.

A common technique for solving these problems is the Finite Element Method (FEM) [48-50]. The solution requires discretisation of the region; however, there are no restrictions (apart from computing power) on the number of elements. FEM has been used in many eddy current NDE applications, Palanisamy and Lord [51] developed a two-dimensional axi-symmetric FEM model for predicting eddy current probe signals. Ida [52] developed a three-dimensional FEM model for eddy current NDE applications. The use of 3D FEM simulations is beneficial to the theoretical study of eddy current NDE, because the geometries of specimens are usually not axi-symmetrical due to the presence of defects. A drawback is that unlike analytical models, the solution is only applicable to a specific problem, if any aspect of the problem is changed then the model will need to be built again.

Several commercial packages for FEM are available, such as ANSYS©[1], Infolytica Magnet©[2], and the package used in this work COMSOL Multiphysics©[3], which combine state of the art modelling techniques, with the ease of use of a graphical interface and visualisation techniques.

2.4 Defect Reconstruction in Eddy Current NDE

The so-called inverse models, where we try to estimate the properties of a specimen under inspection based on measurements, are commonly used to reconstruct the unknown shape of defects. Common methods used for inversion are mathematical optimisation methods [39, 53-57], genetic algorithms [58] and neural networks [25, 59-62]. The drawback of these is that they are computationally expensive, as a model has to be solved at each step to predict the shape of the defect. A new solution will be investigated in this work, where properties of the response will be mapped to the defect profile, using a mapping function, removing the need for the inverse modelling process.

2.5 Research Gaps

In all NDE methods, and especially in eddy current testing, simulation models serve as useful tools for, amongst other things, gaining an understanding of the underlying physical processes, selecting an optimum set of test parameters and even calculating the probability of detecting a defect.

Modelling so far has been based on the measurement of impedance change, which is the quantity traditionally used in eddy current NDE. However, the need to detect subsurface defects, and therefore use a low frequency excitation, which penetrates, further into the specimen, has lead to the use of magnetic field measurements. This work seeks to model and analyse the magnetic field acquired from Hall sensors. The research aims to fill the gap where impedance plane measurements may not be suitable, such an in magnetic field visualisation and sensor arrays.

As well as numerical modelling, analytical modelling for the magnetic field response will be investigated. Previous research based on analytical modelling for eddy current testing, concentrated on simulating coil impedance changes and had problems

[1] ANSYS, Inc.
[2] Infolytica
[3] COMSOL AB

calculating the unbounded integral expressions within closed-form solutions [2]. The TREE method [3, 4] has been extended to model magnetic field signals [30, 63] which are measured using solid-state magnetic field sensors (such as Hall sensor). This has been extended to pulsed measurements and spatial field measurement.

The use of sensor arrays has become common in NDE for visualisation and mapping. A magnetic sensor array, which facilitates magnetic field sensing [10, 11, 64] will be used to provide information on the spatial distribution of the magnetic field from an eddy current probe.

As inverse modelling is a computationally expensive process, the use of magnetic field measurements for defect profile reconstruction, using a transformation or mapping function, will be investigated.

These points have illustrated the need to investigate the magnetic field response to defects in eddy current NDE. Results have shown that experimental measurements of the magnetic field give a clear indication of the presence of defects in the specimen under inspection. This is promising when compared to existing inspection methods. The use of a single sensor can also be extended to an array, obtaining simultaneous information about an area under inspection, leading to improved QNDE.

These approaches provide information on defect shape, size and location, for defect quantification and reconstruction, bridging the gap between theoretical and experimental study in NDE.

2.6 Chapter Summary

A literature survey of eddy current NDE has been performed. This is followed by summary of analytical and numerical methods used in eddy current NDE to predict the resulting signals associated with different experimental conditions. Investigating the interaction of magnetic fields with defects can provide information for defect characterisation. The measurements can then be used to reconstruct the profiles of defects under examination with the help of models and transformation matrices.

Chapter 3 Nondestructive Evaluation Methods

3.1 Chapter Introduction

In this chapter, the common NDE methods, particularly eddy current, are reviewed; their principles are briefly presented, followed by their applications to inspection.

3.2 Eddy Current Testing

Eddy current testing is one of the most widely used electromagnetic NDE techniques. It has applications in the inspection of conductive materials for crack detection, thickness measurement and conductivity measurement.

In eddy current testing, a probe coil is driven by a time varying current (usually a single frequency sine wave, but swept frequency excitation and pulse excitation are also used). This alternating current produces a time varying magnetic field axially around the coil. When the coil is placed near a conductive specimen, electromagnetic induction causes a current to be induced in the specimen (Faraday's Law), which in turn produces a secondary magnetic field (which opposes the primary field due to Lenz's Law). The principle is shown in figure 1.1 [65]. The interaction between the magnetic field generated by the coil and the magnetic field generated by the eddy currents can be measured using a pick up coil or magnetic sensor to give an indication of defects or any variation of material properties such as conductivity, of the specimen under examination. The coil excitation may range from a several Hz up to the MHz range. The frequency is selected based on the material of the specimen under test and the depth of the defect (see equation (3.3)).

Eddy current testing is used in the following applications [66].

1. Detecting material discontinuities such as cracks and holes.

2. Noncontact measurement of the thickness of metallic sheets, plates and tube walls.

3. Measurement of the thickness of coating of base materials, where the coating and base materials have different electrical or magnetic properties.

4. Identifying or separating materials

5. Determining the depth of case hardening

6. Locating hidden metallic objects such as pipes

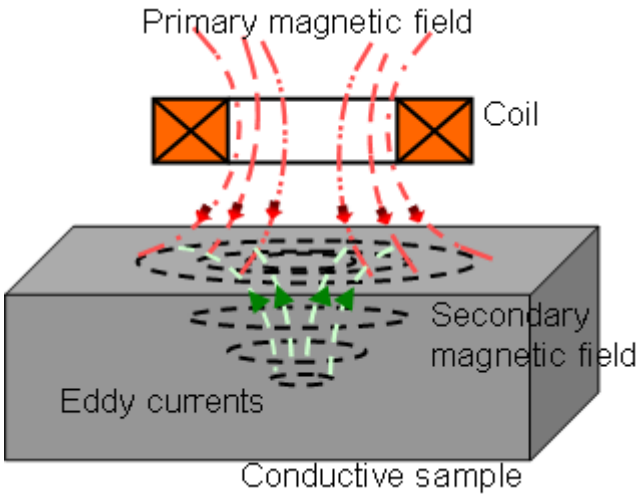

Figure 3.1 Principle of eddy current testing [65]

Eddy currents are most sensitive to surface or near-surface defects as the currents flow near the surface of the specimen (due to the skin effect) and decay exponentially. The flow of eddy current is given by equation (3.1) [67].

$$J_x = J_0 e^{-x\sqrt{(\sqrt{\pi f \sigma \mu})}} \qquad \textbf{(3.1)}$$

Where J_x is the eddy current density at depth x and J_0 is the surface current density, equation (3.1) can be written as equation (3.2).

$$J_x = J_0 e^{\left(-\frac{x}{\delta}\right)} \qquad \textbf{(3.2)}$$

Where δ is the standard depth of penetration, given by equation (3.3).

$$\delta = \frac{1}{\sqrt{\pi f \sigma \mu}} \qquad \textbf{(3.3)}$$

Here μ is magnetic permeability and σ is electrical conductivity. Eddy current density decreases rapidly with depth and the effective inspection depth is 3δ (where the eddy current density has reached ~5% of the surface value). The term $\left(\frac{x}{\delta}\right)$ denotes the increasing phase lag of the signal with depth (in radians).

Since the sensitivity of pickup coils is proportional to the excitation frequency, standard eddy current techniques (such as impedance measurement) are insufficient for deep, subsurface defect detection. In such cases, it is more advantageous the measure the magnetic field rather that its rate of change (the coil impedance change). In this work the magnetic field will be measured using a magnetic sensor, a Hall sensor [12, 68]. As well as the Hall sensor, GMR [23, 69] and SQUID [70-77] are becoming popular.

To obtain more information about the properties of the specimen, or defects embedded in the specimen, multi-frequency (or swept frequency) techniques can be used [78]. The disadvantage of this is the need to repeat the measurement at each frequency as opposed to a single measurement.

In order to counteract some of the limitations of single and multi-frequency eddy current testing, the PEC technique has been introduced. PEC testing is an extension of conventional eddy current testing where pulses or square waves are used to excite the probe coil, as opposed to sine wave excitation [79, 80]. The pulse is used as this contains a range of frequency components in the excitation, allowing information relating to a range of inspection depths and for the detection of deep subsurface defects. When a pulsed excitation is used, the transient (time) response is measured, as opposed to the frequency response. PEC has applications in the inspection of specimens with coatings [81], multilayered specimens [82] and subsurface defect detection [15].

Some advantages and disadvantages of eddy current testing are given in table 3.1.

Method	Advantages	Limitations
Eddy current testing (ECT)	Low cost Quick Versatile Can be non-contact Can penetrate through coatings (such as paint) Detection of subsurface defects	Material must be electrically conducting Shallow depth of penetration Lift-off effects

Table 3.1 Eddy current testing

3.3 Magnetic Flux Leakage Testing

Magnetic flux leakage (MFL) testing is a magnetisation-based technique for detection of corrosion, cracks, etc. in ferromagnetic materials [83, 84] with high magnetic permeability such as steel, using a strong magnet (permanent magnet or electromagnet). A defect in the material forces the applied magnetic field to leak outside the specimen around the defect. The leakage field can be detected using a magnetic field sensor, such as a Hall sensor. MFL is commonly used for inspection of rail-tracks [5, 85], pipelines [86, 87] and storage tanks [84, 88]. Advantages and disadvantages of magnetic flux leakage testing are given in table 3.2.

Method	Advantages	Limitations
Magnetic Flux Leakage testing (MFL)	Quick Inexpensive	Poor defect quantification Poor response for subsurface defects Inspection of ferromagnetic materials only

Table 3.2 Magnetic flux leakage testing

3.4 Microwave Testing

Microwave testing transmits electromagnetic waves (at a higher range than traditional eddy current testing) into dielectric materials, and maps the amplitude or phase of the reflected or transmitted wave using a receiver to create an image of the specimen under investigation [89]. This technique is useful in the inspection of modern materials such as composites, which are replacing metals in many applications. As well as composites, microwave testing allows the inspection of nonconductive materials [90] and inspection under paintwork [91], see figure 3.2 for a microwave image of corrosion under the paintwork of a steel specimen (where the dark area indicates the corrosion area) [92].

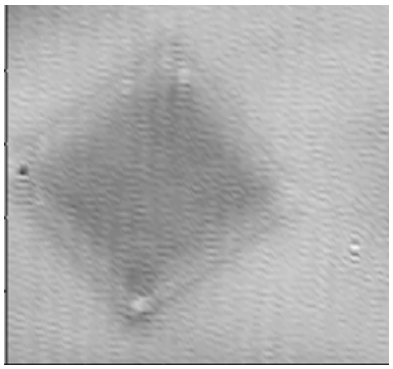

Figure 3.2 Corrosion under paintwork [92]

Some advantages and disadvantages of microwave testing are given in table 3.3.

Method	**Advantages**	**Limitations**
Microwave testing (MT)	Penetrate painted surfaces Non-contact Allows determination of dielectric properties.	Safety

Table 3.3 Microwave testing

3.5 Other Inspection Methods

This section gives an overview of other common inspection methods used in NDE.

3.5.1 Visual testing

The most basic NDE technique is visual inspection. Here the inspector looks for surface imperfections, which link to defective parts or components. Liquid penetrant testing is a widely used form of visual inspection, where the component under test is coated with a solution that contains a visible or florescent dye. Excess solution is then removed from the surface of the object; however, it is left behind in surface breaking defects.

Magnetic particle inspection (MPI) is another visual inspection technique, which can be used to detect surface and near-surface defects in ferromagnetic components and structures. Magnetic particles are applied to the surface of the material and a magnetic field is induced to flow in the component under inspection using permanent magnets or electromagnets. Discontinuities such as surface or near-surface defects cause the induced magnetic field to leak out of the material into the air. Figure 3.3 illustrates the principle of MPI [65].

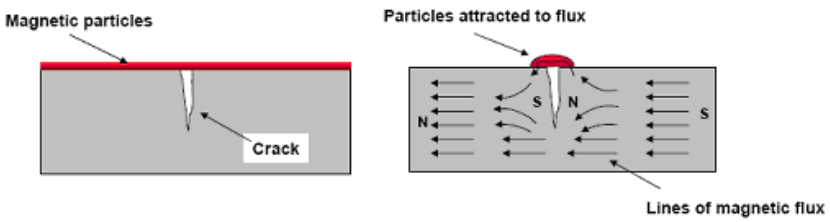

Figure 3.3 Magnetic particle inspection [65]

Magnetic particles, usually suspended in a suitable liquid carrier, are attracted to areas of magnetic flux leakage, providing a visual indication of the position of any defects. Some advantages and disadvantages of visual inspection methods are given in table 3.4.

Method	Advantages	Limitations
Visual Testing (VT)	Ease of testing No specific equipment required	Limited to size of defect observable by operator.

Table 3.4 Visual testing

3.5.2 Ultrasonic testing

In ultrasonic testing, piezoelectric transducers are used to transmit ultrasonic (sound) pulses into the material under test. The transmitted pulses are reflected by voids in the material due to discontinuities such as cracks, or material boundaries such as inclusions as shown in figure 3.4 [65].

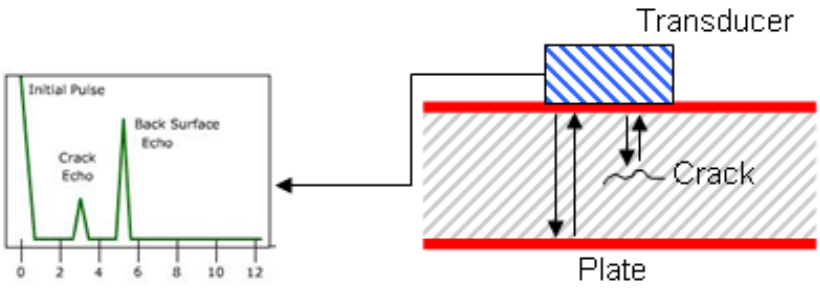

Figure 3.4 Ultrasonic testing [65]

Reflections are transmitted and received by the same transducer are analysed to distinguish between reflections from the material edges and sides and from defects. Some advantages and disadvantages of ultrasonics are given in table 3.5.

Method	Advantages	Limitations
Ultrasonic Testing (UT)	Works on a variety of media (solid and liquids) also metals and composites Accurate defect location Can determine physical properties, such as structure.	Requires couplant on surface Complex procedure Rough or irregular surfaces difficult to inspect

Table 3.5 Ultrasonic testing

3.5.3 Radiographic testing

The basic principle of radiography is that the attenuation of penetrating radiation in materials is a function of radiation energy, material density and material thickness. Defects in the test specimen cause variations in the transmitted radiation intensity. The transmitted radiation beam is then recorded by some means (film or digital detectors) which forms a radiographic image. Even though radiography is considered as one of the most commonly used techniques for weld inspection, the reliability of detection of defects using this technique relies on the capability in interpreting the radiographic images. Some advantages and disadvantages of radiographic testing are given in table 3.6.

Method	Advantages	Limitations
Radiographic Testing (RT)	Works on a variety of materials Detect internal defects Permanent record of inspection on film	As thickness of specimen increases, detection ability decreases Large amount of equipment Image interpretation Safety hazard

Table 3.6 Radiographic testing

3.5.4 Thermography testing

Thermographic NDE can be divided into two categories, passive and active. Passive tests materials, which are at different temperatures to ambient temperature (such as inspection of electrical circuits), while active uses an external heat source (lamp or eddy current) to heat the component and measure the change in temperature due to the presence of defects. In eddy current based thermography the specimen is heated by induction heating and the induced eddy currents are converted to heat through ohmic heating (Joule's law) [93]. As with eddy current NDE, defects disturb the current flow and change the temperature distribution. Results can then be immediately accessed using thermal imaging to provide an indication of any major faults. Some advantages and disadvantages of thermographic inspection methods are given in table 3.7.

Method	**Advantages**	**Limitations**
Thermography Testing (TT)	Use on a wide variety of materials. Inspect over a large area.	Expensive Infrared camera required for transient measurements. Thermal contrast required between specimen and defect.

Table 3.7 Thermography testing

The applicability of the NDE techniques given in this chapter are shown in table 3.8.

Technique	Materials	Detection Capability	Depth Evaluation	Numerical Modelling
Eddy Current	Conducting	Surface, Near Surface	Possible	Possible
Magnetic Flux Leakage	Ferromagnetic	Surface, Near Surface	Possible (Near Surface)	Possible
Microwave	Conducting and dielectric	Surface, Near Surface, Subsurface	Possible	Possible
Visual	All	Surface	Not Possible	Not Possible
Ultrasonic	All	Surface, Near surface, Subsurface	Possible	Possible
Radiographic	All	Surface, Near Surface, Subsurface	Possible	Possible
Thermography	Thermally conductive	Surface, Near Surface, Subsurface	Possible	Possible

Table 3.8 Applicability of NDE techniques

3.6 Chapter Summary

Various NDE techniques commonly used in industry have been outlined in this chapter. ENDE methods, such as eddy current, are widely used and are complementary to other techniques such as ultrasonics and radiography. All of the techniques seek to establish a relationship between the excitation (for example electromagnetic or acoustic wave) and the properties of the material, which is being examined. The advantages, disadvantages and applicability of the common inspection methods have been discussed.

Chapter 4 Eddy Current NDE Modelling Methods

4.1 Chapter Introduction

The chapter describes the theoretical background to eddy current NDE. The governing Maxwell's equations and numerical and analytical modelling methods are discussed, to show the fundamental theory on which this research is based.

Eddy current numerical modelling is performed to study eddy current testing phenomena and also the interaction of eddy currents (and the resulting magnetic field) with defects (forward model). These simulations can be used to predict the magnetic field response when a probe is scanned over a defect. As well as forward models, numerical or analytical models can be used to build an inverse model, where unknown specimen properties (such as thickness, conductivity or defect size) can be predicted from magnetic field measurements, see table 4.1.

Model Type	**Known Input**	**Predicts**
Forward	Specimen Properties	Magnetic Field
Inverse	Measured Magnetic Field	Specimen Properties

Table 4.1 Types of modelling

The measured signals are compared with the signals predicted by the theoretical models in terms of the properties of the specimen. This inverse process is iterative, the iteration will not stop until the minimum error between measured value and predicted value is reached.

These models are a valuable tool in visualising the magnetic field distribution around the eddy current probe and the specimen. This helps understanding not only of the underlying physics of the problem but is also useful in probe and experimental design.

4.2 Governing Equation for Eddy Current Phenomena

Electromagnetic phenomena are governed by a series of laws describing the relationships between electric and magnetic fields known as Maxwell's equations [94].

4.2.1 Maxwell's equations in differential form

Ampere's Law $$\nabla \times \overline{H} = \overline{J} + \frac{\partial \overline{D}}{\partial t} \quad \textbf{(4.1)}$$

Ampere's Law in differential form, equation (4.1), states that a circulating ($\nabla \times$ is the curl) magnetic field $\overline{H}$ is produced by an electric current density $\overline{J}$ [2].

Faraday's Law $$\nabla \times \overline{E} = -\frac{\partial \overline{B}}{\partial t} \quad \textbf{(4.2)}$$

Faraday's Law in differential form, equation (4.2), states that a changing magnetic flux density $\overline{B}$ produces a circulating electric field intensity, $\overline{E}$.

Gauss's Law (for magnetic fields) $$\nabla \cdot \overline{B} = 0 \quad \textbf{(4.3)}$$

Gauss's Law (for magnetic fields) in differential form, equation (4.3), states that the divergence of the magnetic flux density $\overline{B}$ at any point is zero.

4.2.2 Maxwell's equations in integral form

Ampere's Law $$\oint_C \overline{H} \cdot dl = \int_S \left(\overline{J} + \frac{\partial \overline{D}}{\partial t} \right) \cdot ds \quad \textbf{(4.4)}$$

Amperes Law on integral form, equation (4.4), states that a current flowing through a surface produces a circulating magnetic field $\overline{H}$ round that surface[2].

Faraday's Law $$\oint_C \overline{E} \cdot dl = -\frac{\partial}{\partial t} \int_S \overline{B} \cdot ds \quad \textbf{(4.5)}$$

Faraday's Law in integral form, equation (4.5), states that a changing magnetic flux density through a surface induces a circulating electromotive force (emf) on the

[2] For quasi-static phenomena where $(\sigma >> \omega\varepsilon_0)$, the displacement current term $(\overline{D})$ is neglected, so Ampere's Law is now $\nabla \times \overline{H} = \overline{J}$ or $\oint_C \overline{H} \cdot dl = \int_S \overline{J} \cdot ds$.

boundary of that surface. The negative sign shows that currents induced by a changing magnetic flux oppose the change in flux (Lenz's law).

Gauss's Law (for magnetic fields) $\oint_S \overline{B} \cdot ds = 0$ **(4.6)**

Gauss's Law (for magnetic fields) in integral form, equation (4.6), states that the net magnetic flux density passing out of a surface is zero.

For static phenomena (dc), such as magnetic flux leakage phenomena, all the time derivatives are zero (remove $\frac{\partial}{\partial t}$ term).

Here $\nabla \cdot \overline{A} = \left(\frac{\partial A_x}{\partial x} + \frac{\partial A_y}{\partial y} + \frac{\partial A_z}{\partial z} \right)$ is divergence in cartesian coordinates (which is zero as field lines go from positive to negative), $\nabla \times \overline{A} = \begin{vmatrix} \hat{i} & \hat{j} & \hat{k} \\ \frac{\partial}{\partial x} & \frac{\partial}{\partial y} & \frac{\partial}{\partial z} \\ A_x & A_y & A_z \end{vmatrix}$ is the curl operator in cartesian coordinates (measure of how the field circulates around a point). The following constitutive relationships, shown in equation (4.7) and equation (4.8), are used for linear materials.

$$\overline{B} = \mu_0 \mu_r \overline{H} = \mu \overline{H} \quad \textbf{(4.7)}$$

$$\overline{J} = \sigma \overline{E} \quad \textbf{(4.8)}$$

Where μ_r and μ_0 are the relative permeability and the permeability of free space, respectively. Equations (4.1), (4.7) and (4.8) can be used to find equation (4.9).

$$\nabla \times \overline{H} = \overline{J} = \sigma \overline{E} \quad \textbf{(4.9)}$$

The magnetic flux density can be calculated from equation (4.10).

$$\overline{B} = \nabla \times \overline{A} \quad \textbf{(4.10)}$$

4.2.3 Eddy current modelling

Now we will derive the governing equations for eddy current inspection from Maxwell's equations (quasi-static case). Substituting equation (4.10) into equation (4.2), we get equation (4.11).

$$\nabla \times \overline{E} = -\frac{\partial}{\partial t}\nabla \times \overline{A} = -\nabla \times \frac{\partial}{\partial t}\overline{A} = -\nabla \times \frac{\partial \overline{A}}{\partial t} \quad \textbf{(4.11)}$$

We can write E as equation (4.12)

$$E = -\frac{\partial \overline{A}}{\partial t} - \nabla \psi \quad \textbf{(4.12)}$$

Where ψ is the applied scalar potential. If we multiply both sides by σ, we get equation (4.13)

$$\sigma \overline{E} = -\sigma \frac{\partial \overline{A}}{\partial t} - \sigma \nabla \psi \quad \textbf{(4.13)}$$

If the coil is driven by a current density $\overline{J}$, rewrite equation (4.13) as equation (4.14).

$$\sigma \overline{E} = -\sigma \frac{\partial \overline{A}}{\partial t} + \overline{J} \quad \textbf{(4.14)}$$

Substituting equation (4.7) and equation (4.10) into the left side of equation (4.14), we get equation (4.15).

$$\nabla \times \left[\left(\frac{1}{\mu} \right) \nabla \times \overline{A} \right] = -\sigma \frac{\partial \overline{A}}{\partial t} + \overline{J} \quad \textbf{(4.15)}$$

Expanding $\left(\frac{1}{\mu} \right) \nabla \times \left(\nabla \times \overline{A} \right)$ in equation (4.15), using $\nabla \times \left(\nabla \times \overline{A} \right) = \nabla \left(\nabla \cdot \overline{A} \right) - \nabla^2 \overline{A}$, we get equation (4.16).

$$\left(\frac{1}{\mu} \right) \nabla \left(\nabla \cdot \overline{A} \right) - \left(\frac{1}{\mu} \right) \nabla^2 \overline{A} = -\sigma \frac{\partial \overline{A}}{\partial t} + \overline{J} \quad \textbf{(4.16)}$$

Using the Coulomb gauge, $\nabla \cdot \overline{A} = 0$, on equation (4.16), we get equation (4.17).

$$-\left(\frac{1}{\mu} \right) \nabla^2 \overline{A} = -\sigma \frac{\partial \overline{A}}{\partial t} + \overline{J} \quad \textbf{(4.17)}$$

Multiplying both sides of equation (4.17) by μ and simplifying, we get equation (4.18).

$$\nabla^2 \overline{A} = -\mu \overline{J} + \mu \sigma \frac{\partial \overline{A}}{\partial t} \quad \textbf{(4.18)}$$

Equation (4.18) is the equation for the magnetic vector potential in an isotropic, linear, homogeneous medium. This governs the underlying eddy current phenomena, where ∇^2 is the Laplace operator. If the coil is excited by a sinusoidal source $\left(\frac{\partial \overline{A}}{\partial t} = j\omega\overline{A}\right)$, $\omega = 2\pi f$ and $k^2 = j\omega\mu\sigma$, equation (4.18) becomes equation (4.19).

$$\nabla^2\overline{A} = -\mu\overline{J} + k^2\overline{A} \qquad \textbf{(4.19)}$$

In cylindrical coordinates and for a delta function coil with current I, equation (4.19) can be rewritten as equation (4.20).

$$\frac{\partial^2\overline{A}}{\partial r^2} + \left(\frac{1}{r}\right)\frac{\partial\overline{A}}{\partial r} + \frac{\partial^2\overline{A}}{\partial z^2} - \frac{\overline{A}}{r^2} - k^2\overline{A} + \frac{\mu I}{\delta(r-r_0)\delta(z-z_0)} = 0 \qquad \textbf{(4.20)}$$

From the magnetic vector potential, A, it is possible to calculate quantities such as the magnetic flux density, using equation (4.10). Equation (4.21) shows the value in cylindrical coordinates.

$$\overline{B} = \nabla \times \overline{A} = \left(-\frac{\partial A}{\partial z}\right)\hat{r} + \frac{1}{r}\left(\frac{\partial(rA)}{\partial r}\right)\hat{z} \qquad \textbf{(4.21)}$$

4.3 Forward Modelling for Eddy Current Testing

Three types of modelling will be discussed here, numerical modelling, which approximates the solution, analytical models, which provide an exact 'closed-form' solution and semi-analytical models which impose a boundary on the solution to simplify the calculation.

4.3.1 Numerical modelling

A common numerical modelling technique is finite element method (FEM), having the advantage of being able to model complex geometries. The solution requires the discretisation of the solution region, however, there are no restrictions (apart from computing power) on the size and number of the "finite elements". FEM has been used to solve both 2D [51] and 3D [52, 95] problems. A common technique in solving FEM is the use of an energy functionals. The energy functional for eddy current problems can be written as equation (4.22) [96].

$$F(A) = \int_V [E_s + E_i + E_d] dV \quad \textbf{(4.22)}$$

Where the energy due to the magnetic field is E_s, E_i is the input energy from the probe and E_d is the energy dissipated through eddy currents in the specimen. Equation (4.23) shows the energy functional for a 2D axi-symmetric problem [94].

$$F(A) = \int_V \left[\frac{1}{2\mu} \left(\left| \frac{\partial A}{\partial r} + \frac{A}{r} \right|^2 + \left| \frac{\partial A}{\partial z} \right|^2 \right) + \frac{j\omega\sigma}{2} |A|^2 - J_s \cdot A \right] dV \quad \textbf{(4.23)}$$

The solution can be found by minimising this functional throughout the region $\left(\frac{\partial F(A)}{\partial (A)} = 0 \right)$. Using interpolation functions $[N]$ to express the magnetic vector potential, A, at any point within an element as shown in equation (4.24).

$$A = \sum_{i=1}^{3} A_i N_i \quad \textbf{(4.24)}$$

The energy functional to be minimised for an element, can be written in terms of its unknown nodal values as shown in equation (4.25) [94]

$$\begin{bmatrix} S_{1,1} & S_{1,2} & S_{1,3} \\ S_{2,1} & S_{2,2} & S_{2,3} \\ S_{3,1} & S_{3,2} & S_{3,3} \end{bmatrix} \begin{bmatrix} A_1 \\ A_2 \\ A_3 \end{bmatrix} = \mu J \begin{bmatrix} d_1 \\ d_2 \\ d_3 \end{bmatrix} \quad \textbf{(4.25)}$$

Where the nodal values are shown in equation (4.26) and equation (4.27).

$$S_{i,j} = \int_V \left[\frac{\partial N_i}{\partial x} \frac{\partial N_j}{\partial x} + \frac{\partial N_i}{\partial y} \frac{\partial N_j}{\partial y} + j\omega\sigma\mu N_i N_j \right] dV \quad \textbf{(4.26)}$$

$$d_i = \int_V N_i dV \quad \textbf{(4.27)}$$

FEM approximates the solution rather than solving the partial derivatives in the problem, a numerical result rather than a ‘closed-form’ solution.

As computing power has advanced, FEM simulation has shifted from 2D modelling to 3D modelling, which is more suitable to handle asymmetric problems (these cannot be simplified to 2D by using azimuthal coordinates). 3D FEM simulation is useful in

modelling specimens containing defects, as the geometry will no longer be symmetric about the axis.

An application of 3D FEM modelling is in the use of forward modelling (predicting the response for known coils and specimens) in experimental design. The probe coil will be scanned across the simulated defect "slot", dimensions 30mm (l) × 1mm (w) × 5mm (h), in a plate, see figure 4.1.

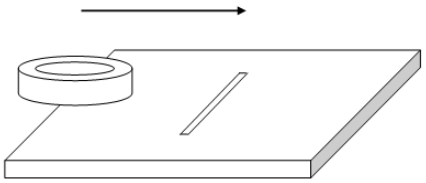

Figure 4.1 Scan across defect

The layout of the problem is shown in figure 4.2.

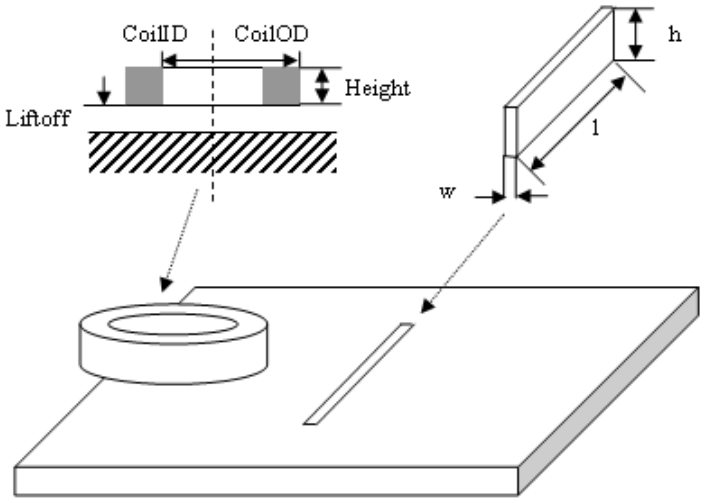

Figure 4.2 Problem layout

Details of the model setup are shown in table 4.2.

Scan	
Scan Step Size (mm)	0.5
Specimen	
Specimen Size (mm)	40×40×20
Specimen Conductivity (MS/m)	30
Defect Size (mm)	30×1×5
Probe	
Coil ID (mm)	18.6
Coil OD (mm)	36.8
Coil Height (mm)	9
Coil Turns	500
Excitation Current (mA)	500

Table 4.2 FEM simulation model setup

The following scenarios will be investigated.

1. Change of excitation frequency

   The effect of excitation frequency of 30Hz (5mm penetration depth), 150Hz (2.5mm penetration depth) and 500Hz (1.2mm penetration depth) was examined and the results shown in figure 4.3.

   As the frequency is increased, the eddy currents are increasingly concentrated near the surface of the specimen, and as the frequency is decreased, the eddy currents increase their penetration into the specimen. Employing a variety of frequencies to probe different depths in the specimen can be very useful for analyzing a greater volume of the specimen.

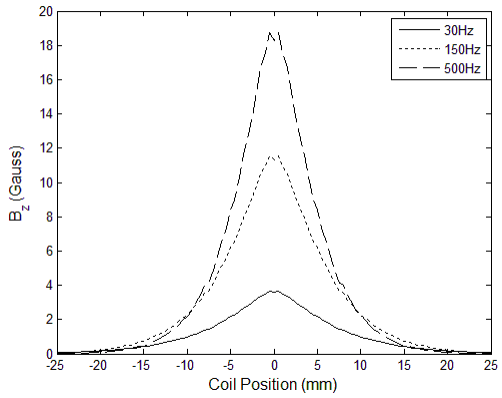

Figure 4.3 B_z for scan across the defect for excitation frequencies (FEM results)

2. Change in model setup

When approximating the solution domain using a mesh, the accuracy of the solution can be improved by using a greater number of elements (finer mesh), although this has the drawback of increased computation time. Details of the meshes used in solving the problem are shown in table 4.3, where elements are number of partitions the geometry has been divided into (the mesh) and the degrees of freedom is the number of functions used in the approximation. The calculation time shown is for each measurement step.

Mesh	**Number of Elements**	**Degrees of Freedom**	**Calculation Time (secs.)**
Size One	16300	131982	28
Size Two	7269	59433	12.5
Size Three	4135	34385	8.2

Table 4.3 Model mesh comparison

The results for the model for each mesh size are shown in figure 4.4, with the error caused by using the coarser meshes (Size Two and Size Three) shown in figure 4.5.

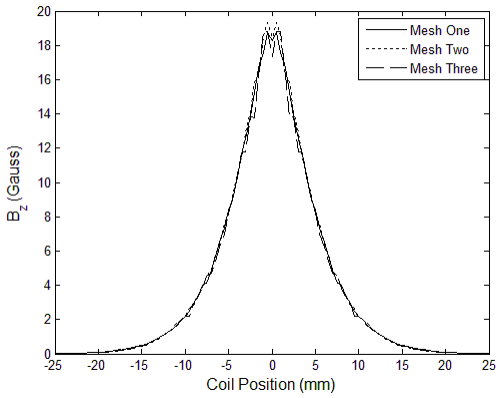

Figure 4.4 B_z for scan across the defect for different meshes (FEM results)

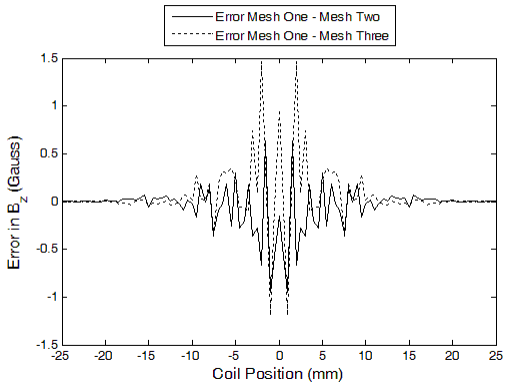

Figure 4.5 Discretisation error using a coarser mesh

4.3.2 Analytical modelling

Analytical modelling provides a 'closed-form' solution to the partial differential equations (in this case for the magnetic vector potential A), which are derived from Maxwell's equations. The application of these analytical models for eddy current testing began with Dodd and Deeds [2] analytical modelling of the eddy current inspection of a two layered plate or coil around an infinitely long conducting rod. With a delta-function coil (r_0, z_0), the potential in all regions will satisfy equation (4.19). This equation for the air region in figure 4.6 is shown in equation (4.28).

$$\frac{\partial^2 A}{\partial r^2} + \left(\frac{1}{r}\right)\frac{\partial A}{\partial r} + \frac{\partial^2 A}{\partial z^2} - \frac{A}{r^2} = 0 \qquad \textbf{(4.28)}$$

The equation in the conductor region in figure 4.6 is shown in equation (4.29).

$$\frac{\partial^2 A}{\partial r^2} + \left(\frac{1}{r}\right)\frac{\partial A}{\partial r} + \frac{\partial^2 A}{\partial z^2} - \frac{A}{r^2} - k^2 A = 0 \qquad \textbf{(4.29)}$$

Setting $A = R(r)Z(z)$, dividing by $R(r)Z(z)$ and setting $\frac{1}{Z(z)}\frac{\partial^2 Z(z)}{\partial z^2} = \text{"constant"}$, gives equation (4.30).

$$\frac{1}{R(r)}\frac{\partial^2 R(r)}{\partial r^2} + \frac{1}{rR(r)}\frac{\partial R(r)}{\partial r} + k^2 - \frac{1}{r^2} = 0 \qquad \textbf{(4.30)}$$

The general solution of this equation has the form of equation (4.31).

$$A(r,z) = \int_0^{\infty} [A(\kappa)J_1(\kappa r) + B(\kappa)Y_1(\kappa r)][C(\kappa)e^{\kappa z} + D(\kappa)e^{-\kappa z}]d\kappa \quad \textbf{(4.31)}$$

Where J_1 is a Bessel function of the first kind, Y_1 is a Bessel function of the second kind, A, B, C, D are coefficients to be determined, $k^2 = j\omega\mu\sigma$, κ is the separation constant and $\lambda = \sqrt{\kappa^2 + k^2}$. Here, $C = 0$ in region 1 (of figure 4.6) where z goes to $+\infty$. Due the divergence of Y_1 at the origin, $B = 0$ in all regions (of figure 4.6). Also, $D = 0$ in region 2 (of figure 4.6), where z goes to $-\infty$.

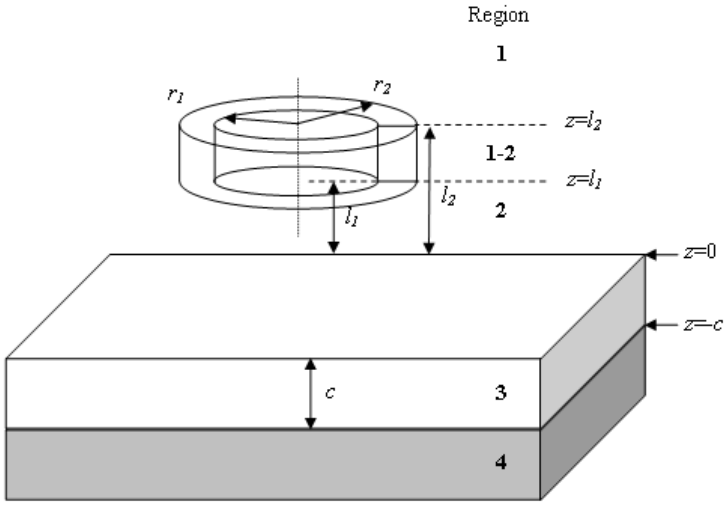

Figure 4.6 Problem regions in Dodd and Deeds analytical model

The solutions in each region (of figure 4.6), for a conductive half-space, are shown in equation (4.32) to equation (4.35) [2].

$$A^{(1)} = \frac{\mu_0 i_0}{2}\int_0^{\infty} J_1(\kappa r)e^{-\kappa z}\frac{\chi(\kappa r_1, \kappa r_2)}{\kappa^3}\left(e^{\kappa z_2} - e^{\kappa z_1}\right)d\kappa \quad \textbf{(4.32)}$$

$$A^{(2)} = \frac{\mu_0 i_0}{2}\int_0^{\infty} J_1(\kappa r)e^{\lambda z}\frac{\chi(\kappa r_1, \kappa r_2)}{\kappa^3}\left(e^{-\kappa z_1} - e^{-\kappa z_2}\right)d\kappa \quad \textbf{(4.33)}$$

$$A^{(1-2)} = \frac{\mu_0 i_0}{2}\int_0^{\infty} J_1(\kappa r)\frac{1}{\kappa^3}\chi(\kappa r_1, \kappa r_2)\left(2 - e^{\kappa(z-z_2)} - e^{-\kappa(z-z_1)}\right)d\kappa \quad \textbf{(4.34)}$$

$$A^{(3)} = \frac{\mu_0 i_0}{2}\int_0^\infty J_1(\kappa r)\frac{\chi(\kappa r_1, \kappa r_2)}{\kappa^3}\left(e^{-\kappa z_1} - e^{-\kappa z_2}\right)\frac{2\kappa\mu_r e^{\lambda z}}{\kappa\mu_r + \lambda}d\kappa \quad \textbf{(4.35)}$$

Where the current density is given by equation (4.36).

$$i_0 = \frac{NI}{\text{Coil Area}} = \frac{NI}{(r_2 - r_1)(z_2 - z_1)} \quad \textbf{(4.36)}$$

With the Fourier-Bessel integral $\chi(x_1, x_2)$, given in equation (4.37).

$$\chi(x_1, x_2) = \int_{x_1}^{x_2} xJ_1(x)dx = \frac{\pi}{2}x\left[J_0(x)H_1(x) - J_1(x)H_0(x)\right]_{x_1}^{x_2} \quad \textbf{(4.37)}$$

Where H_n is a Struve function of order n. This can also be solved using the summation relationship given in equation (4.38).

$$\int_{x_1}^{x_2} xJ_1(x)dx = \left[x_1 J_0(x_1) - 2\sum_{k=0}^{\infty} J_{2k+1}(x_1)\right] - \left[x_2 J_0(x_2) - 2\sum_{k=0}^{\infty} J_{2k+1}(x_2)\right] \quad \textbf{(4.38)}$$

The fact that the vector potential requires the calculation of Fourier Bessel integrals is a drawback to this method (which is addressed in the next section). The magnetic flux density in each region of figure 4.6, is given by equation (4.39) to equation (4.41).

$$B^{(1)} = \frac{\mu_0 i_0}{2}\int_0^\infty \frac{\chi(\kappa r_1, \kappa r_2)}{\kappa^2}\left(e^{\kappa z_2} - e^{\kappa z_1}\right)e^{-\kappa z}\left[J_1(\kappa r)\hat{r} + J_0(\kappa r)\hat{z}\right]d\kappa \quad \textbf{(4.39)}$$

$$B^{(2)} = \frac{\mu_0 i_0}{2}\int_0^\infty \frac{\chi(\kappa r_1, \kappa r_2)}{\kappa^2}\left(e^{-\kappa z_1} - e^{-\kappa z_2}\right)e^{\kappa z}\left[-J_1(\kappa r)\hat{r} + J_0(\kappa r)\hat{z}\right]d\kappa \quad \textbf{(4.40)}$$

$$B^{(1-2)} = \frac{\mu_0 i_0}{2}\int_0^\infty \frac{\chi(\kappa r_1, \kappa r_2)}{\kappa^2}\begin{bmatrix}\left(e^{\kappa(z-z_2)} - e^{-\kappa(z-z_1)}\right)J_1(\kappa r)\hat{r} \\ -\left(e^{\kappa(z-z_2)} - e^{-\kappa(z-z_1)}\right)J_0(\kappa r)\hat{z}\end{bmatrix}d\kappa \quad \textbf{(4.41)}$$

The field due to the coil is given by equation (4.42).

$$B^{(s)} = B^{(1)} + B^{(1-2)} + B^{(2)} \quad \textbf{(4.42)}$$

The total magnetic field above the conductor is given by equation (4.43).

$$B^{(1+2)} = B^{(s)} + \ldots$$
$$+ \frac{\mu_0 i_0}{2} \int_0^\infty \frac{\chi(\kappa r_1, \kappa r_2)}{\kappa^2} J_1(\kappa r)\left(e^{-\kappa z_1} - e^{-\kappa z_2}\right) e^{-\kappa z} \frac{\kappa\mu_r - \lambda}{\kappa\mu_r + \lambda}\left[J_1(\kappa r)\hat{r} + J_0(\kappa r)\hat{z}\right] d\kappa \tag{4.43}$$

The field in the conductor is given by equation (4.44).

$$B^{(3)} = \mu_0 i_0 \int_0^\infty \frac{\chi(\kappa r_1, \kappa r_2)}{\kappa^2}\left(e^{-\kappa z_1} - e^{-\kappa z_2}\right) e^{\lambda z} \frac{\mu_r}{\kappa\mu_r + \lambda}\left[-J_1(\kappa r)\lambda\hat{r} + J_0(\kappa r)\kappa\hat{z}\right] d\kappa \tag{4.44}$$

4.3.3 Semi-analytical modelling

In the Dodd and Deeds model, the boundary of interest goes to infinity and the electromagnetic fields are expressed in closed-form in terms of a Fourier-Bessel integral, which suffers from slow convergence, this problem will now be addressed using the semi-analytical TREE method [4]. For a coil in free-space, the magnetic vector potential can be found from the Biot-Savart law, shown in equation (4.45) [4].

$$A = \frac{\mu_0 I}{4\pi} \oint_l \frac{1}{|r - r_0|} dl \tag{4.45}$$

If we now truncate the region (along r) by imposing a magnetic insulation boundary at a radial distance h (in this case, $h = 30 \times$ coil outer radius r_2) from the source coil, the distance vector (distance between the source and field point) can now be written as (the space is bounded by a cylinder with radius $r = h$) equation (4.46) [4].

$$\frac{1}{|r - r_0|} = \frac{2}{h^2} \sum_{m=0}^{\infty} (2 - \delta_m) \cos[m(\varphi - \varphi_0)] \sum_{i=1}^{\infty} e^{-\kappa_i |z - z_0|} \frac{J_m(\kappa_i r) J_m(\kappa_i r_0)}{\kappa_i [J_{m-1}(\kappa_i h)]^2} \tag{4.46}$$

This can then be integrated, using equation (4.45), to find the magnetic vector potential. This series expansion $\left\{ \sum_{i=1}^{\infty} J_1(\kappa_i r) e^{\lambda_i z} \right\}$ is the basis of the TREE method, in practice this is a large series, for example, 300 terms. This results in a considerably reduced computation time, when compared with the integral expressions in the Dodd and Deeds method [2].

The effect of modifying the truncation limit (shown in terms on the coil outer radius r_2) and the number of terms in the series, when calculating the magnetic flux density from

an eddy current probe over a specimen, excited by a range of excitation frequencies, are shown in figure 4.7 and figure 4.8, respectively. The size of the truncation limit has little effect in this case. Once the number of terms in the series is above 300, there is also little change in the results.

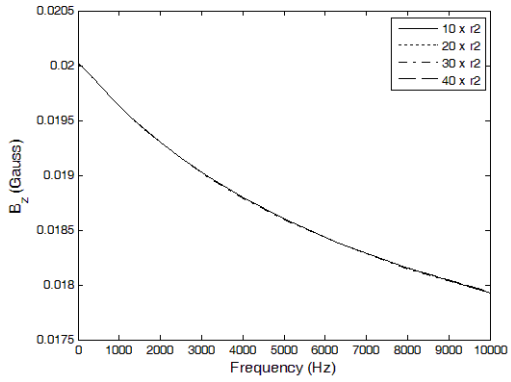

Figure 4.7 Modification of truncation limit *(h)* in TREE model

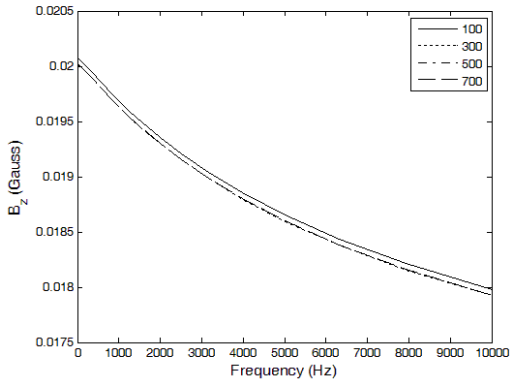

Figure 4.8 Modification of number of terms *(i)* of series in TREE model

The execution times for varying the truncation limit and for varying the number of terms in the series are shown in figure 4.9 and figure 4.10, respectively. As expected, the execution time is proportional to terms in the series. As the truncation length is increased, the integration limits for the Bessel integral function are reduced, speeding up the calculation.

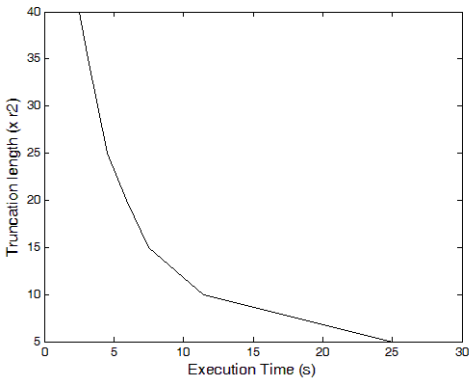

Figure 4.9 Execution time for modification of truncation limit *(h)* in TREE model

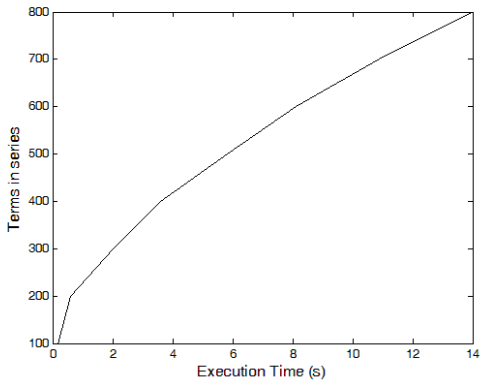

Figure 4.10 Execution time for modification of number of terms *(i)* of series in TREE model

A schematic diagram of the TREE model is shown in figure 4.11. The boundary condition $H(x \to \infty, z) = 0$ is replaced by $H(h, z) = 0$, where h is the truncation distance, r_2 is the coil outer radius, r_1 is the coil inner radius, z_1 is the lift-off, z_2 is the coil height + lift off .

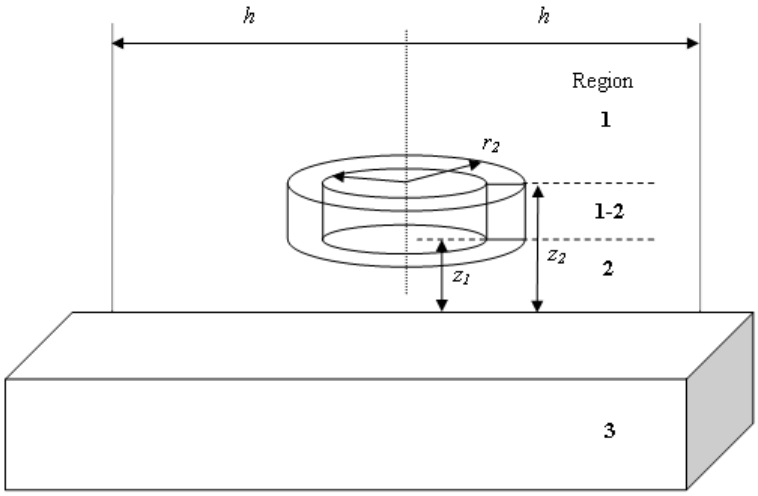

Figure 4.11 TREE formulation

The solution for a circular probe coil has the form given in equations (4.47) to (4.50), where the solutions in each region of figure 4.11, are as follows [4]. This can be compared with the Dodd and Deeds formulation shown in equations (4.32) to (4.35).

$$A^{(1)} = \mu_0 i_0 \sum_{i=1}^{\infty} J_1(\kappa_i r) e^{-\kappa_i z} \left[\left(e^{\kappa_i z_2} - e^{\kappa_i z_1} \right) + \left(e^{-\kappa_i z_1} - e^{-\kappa_i z_2} \right) \frac{\kappa_i \mu_r - \lambda_i}{\kappa_i \mu_r + \lambda_i} \right] \frac{\chi(\kappa_i r_1, \kappa_i r_2)}{\kappa_i^4 \left[h J_0(\kappa_i h) \right]^2}$$

(4.47)

$$A^{(2)} = \mu_0 i_0 \sum_{i=1}^{\infty} J_1(\kappa_i r) \left(e^{\kappa_i z} + e^{-\kappa_i z} \frac{\kappa_i \mu_r - \lambda_i}{\kappa_i \mu_r + \lambda_i} \right) \left(e^{-\kappa_i z_1} - e^{-\kappa_i z_2} \right) \frac{\chi(\kappa_i r_1, \kappa_i r_2)}{\kappa_i^4 \left[h J_0(\kappa_i h) \right]^2}$$

(4.48)

$$A^{(1-2)} = \mu_0 i_0 \sum_{i=1}^{\infty} \frac{J_1(\kappa_i r)}{\kappa_i^4 \left[hJ_0(\kappa_i h)\right]^2} \chi(\kappa_i r_1, \kappa_i r_2) \times \left[2 - e^{-\kappa_i (z-z_1)} - e^{-\kappa_i (z-z_2)} + \left[e^{-\kappa_i (z-z_1)} - e^{-\kappa_i (z-z_2)} \right] \frac{\kappa_i \mu_r - \lambda_i}{\kappa_i \mu_r + \lambda_i} \right] \quad \textbf{(4.49)}$$

$$A^{(3)} = 2\mu_0 \mu_r i_0 \sum_{i=1}^{\infty} J_1(\kappa_i r) e^{\lambda_i z} \left[\left(\frac{e^{-\kappa_i z_1} - e^{\kappa_i z_2}}{\kappa_i \mu_r + \lambda_i} \frac{\chi(\kappa_i r_1, \kappa_i r_2)}{\kappa_i^4 \left[hJ_0(\kappa_i h)\right]^2} \right) + \left(e^{-\kappa_i z_1} - e^{-\kappa_i z_2} \right) \right] \quad \textbf{(4.50)}$$

Here κ_i are the discrete eigenvalues and the *i*th zero (positive root) of the Bessel function $J_1(\kappa_i r)$, $\lambda_i = \sqrt{\kappa_i^2 + j\omega\mu_0\mu_r\sigma}$. The discrete eigenvalue has been introduced instead of the separation constant κ in the Dodd and Deeds model, due to the imposed Dirichlet boundary condition, $A(\pm h, z) = 0$, for the magnetic vector potential at $r = h$. The discrete eigenvalues are then calculated using equation (4.51) [3].

$$\begin{aligned} &J_1(\kappa_i h) = 0 \\ &J_1(x_i) = 0 \\ &\kappa_i = \frac{x_i}{h} \end{aligned} \quad \textbf{(4.51)}$$

Here the magnetic flux density, measured over the area of the sensor $(r_0 \times [c_2 - c_1])$, is given by equation (4.52) to equation (4.54) [30].

$$B^{(c)} = \frac{2\mu_0 i_0}{r_0 (c_2 - c_1)} \sum_{i=1}^{\infty} \frac{\chi(\kappa_i r_1, \kappa_i r_2) J_1(\kappa_i r_0)}{\left[hJ_0(\kappa_i h)\right]^2 \kappa_i^4} \int_{c_1}^{c_2} F(\kappa_i z_1, \kappa_i z_2, \kappa_i z) dz \quad \textbf{(4.52)}$$

$$\Delta B = \frac{2\mu_0 i_0}{r_0 (c_2 - c_1)} \sum_{i=1}^{\infty} \frac{\chi(\kappa_i r_1, \kappa_i r_2) J_1(\kappa_i r_0)}{\left[hJ_0(\kappa_i h)\right]^2 \kappa_i^5} \frac{U_1}{V_1} \left(e^{-\kappa_i c_2} - e^{-\kappa_i c_1} \right) \left(e^{-\kappa_i z_2} - e^{-\kappa_i z_1} \right) \quad \textbf{(4.53)}$$

Where

$$F(\kappa_i z_1, \kappa_i z_2, \kappa_i z) = \begin{cases} e^{\kappa_i (z_2 - z)} - e^{\kappa_i (z_1 - z)} & z \geq z_2 \\ 2 - e^{\kappa_i (z - z_2)} - e^{\kappa_i (z_1 - z)} & z_2 \geq z \geq z_1 \\ e^{\kappa_i (z - z_1)} - e^{\kappa_i (z - z_2)} & z_z \geq z \end{cases} \quad \textbf{(4.54)}$$

The total field is given by equation (4.55).

$$B = B^{(c)} + \Delta B \quad \textbf{(4.55)}$$

Where U and V are reflection coefficients for multilayered specimens [30, 97].

The series approach is a very fast computation method, since not only the eigenvalues κ_i but also other terms can be pre-computed. The most computationally demanding term is the Bessel integral $\chi(\kappa_i r_1, \kappa_i r_2)$, and for a specific coil can also be pre-computed since it depends only on r_1 and r_2, which is useful in inverse problem applications [3].

The TREE method has been extended to PEC [63] where the Fast Fourier Transform (FFT) is used to convert the pulse excitation current from the time to frequency domain and the calculation is performed as in the previous work [30], the Inverse FFT (IFFT) is then used to convert the response back to the time-domain. The calculation process in shown in figure 4.12.

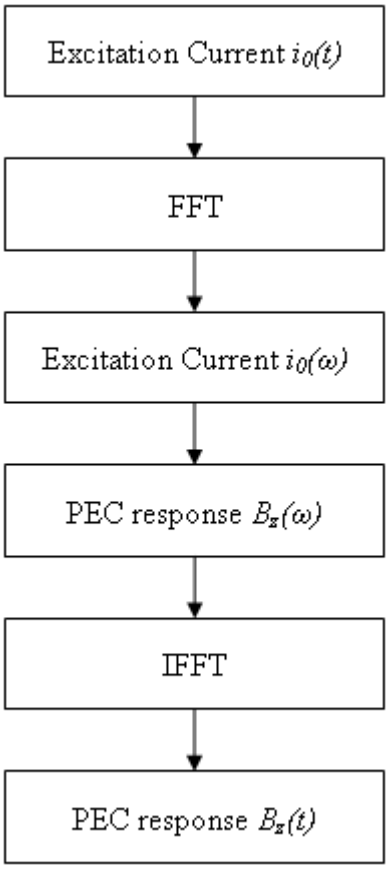

Figure 4.12 PEC TREE calculation process

This method of converting the pulse to the frequency domain is also discussed in the work on defect reconstruction.

A comparison of the two analytical modelling methods discussed in this chapter is given in table 4.4

	Dodd Deeds Integral Expression	**TREE**
Advantages	Simulate eddy current and PEC inspections for multilayered planar and cylindrical specimens	Integral expressions are replaced by a series of eigenfunction expansions, which improves computing time
Disadvantages	Closed-form solutions comprise of Bessel and exponential functions and infinite integrals, which have a long computation time	Accuracy depends on the width of truncated regions and number of expansions

Table 4.4 Comparison of analytical modelling methods

4.4 Chapter Summary

In this chapter, an introduction to Maxwell's equations, which govern electromagnetic phenomena, is given. These governing equations can be solved using numerical or analytical methods.

Numerical models are an approximation based on the discretisation of the domain. These are more powerful than the analytical models as they can be used for complex geometries and materials. In this work, the presence of a defect has been modelled using numerical (FEM) simulations to predict the magnetic field change as an eddy current probe is scanned over a defect.

Analytical models have been common since the pioneering work of Dodd and Deeds who proposed an integral solution to calculate the magnetic vector potential for various axi-symmetric geometries (coil over plate, coil between plates and coil encircling tube). This can then be used to predict the impedance change of the induction coil (probe). The analytical models of Dodd and Deed have been extended in the Truncated Region Eigenfunction Expansion (TREE) method by replacing the integral with series expressions. Following on from this, the Extended TREE (ETREE) method has been

developed to predict the magnetic field measurement using a solid-state sensor (Hall sensor).

Chapter 5 Eddy Current NDE Experimental Methods

5.1 Chapter Introduction

Although inspecting a single point of a specimen can give an indication of any change in properties (whether there is a crack present), in order to gain quantitative (spatial) information relating to a defect, it is necessary to obtain information over an area of the specimen. Experimental setups for eddy current NDE comprise an excitation source (normally a function generator/power amplifier/coil) for generating the electromagnetic field injected into specimen under evaluation, a sensor for measuring and quantifying the electromagnetic field, signal processing (data acquisition and visualisation), providing the results of the experimental measurement. The general eddy current inspection system, both modelling and experimental study, is shown in figure 5.1.

The first stage in experimental study is the design of the probe for eddy current excitation. The sensitivity of defect detection is influenced by both the parameters of the probe (inductance) and the geometry of the probe; these factors, which influence the probe design, are discussed. A magnetic field sensor (Hall sensor) is used to measure the change in magnetic field due to the presence of a defect (crack). A discussion of magnetic field sensors is presented, outlining their operation and applications.

The magnetic field measurements provide an alternative to the existing impedance plane measurements where the magnetic field response is measured directly. The use of magnetic field measurements is common in eddy current NDE, however this is when pulsed excitation is used and the transient response is measured. These measurements provide a useful indication of the presence of both surface and subsurface defects. In an advance from measuring the amplitude of the magnetic field change due to the presence of a defect, the use of complex (real and imaginary components) magnetic field measurements with a combination of circular and rectangular probes will be investigated.

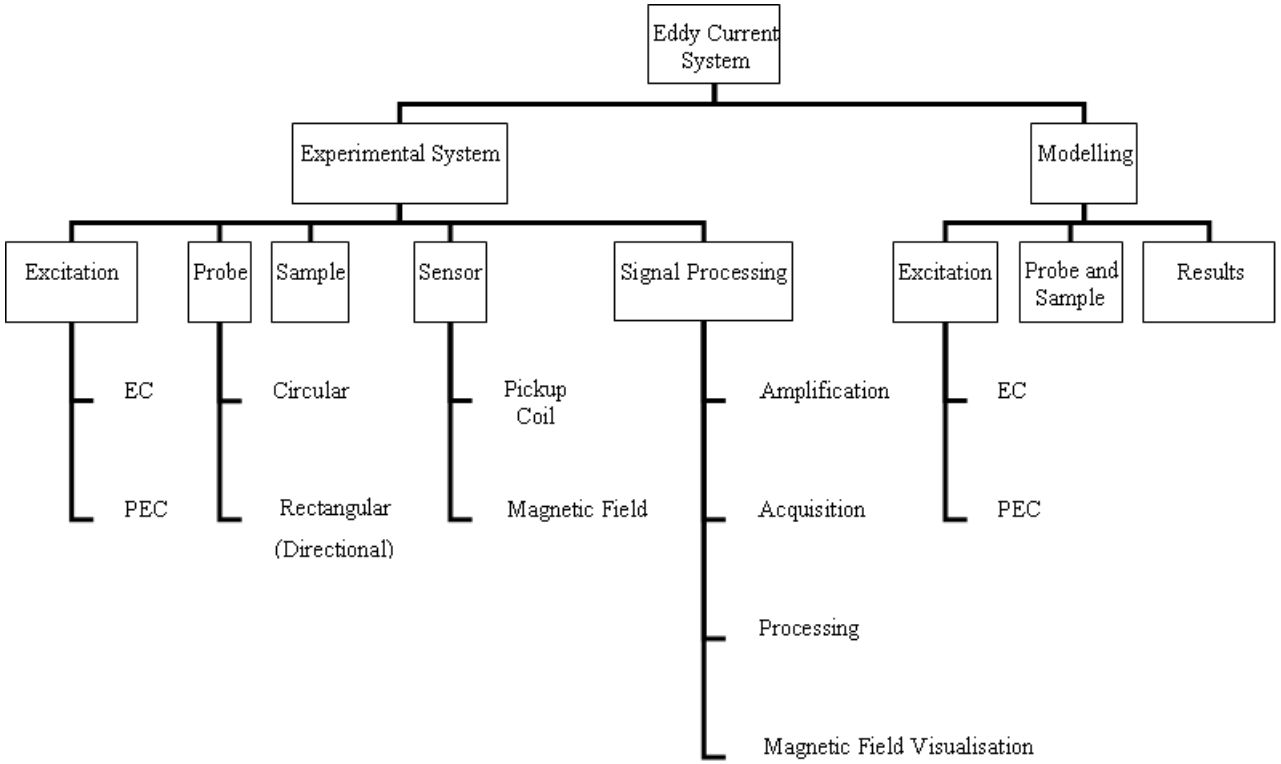

Figure 5.1 Eddy current system

Here, an X-Y scanner will be used to scan a sensor over the area of a defect and the change in magnetic field due to that defect will be measured. The goal here is to build a relationship between the magnetic field distribution and defect information (size, shape or location). The resulting data is presented in the form of an image [98]. The image provides easy interpretation of the presence of defects, and can be used to monitor defects over time.

Firstly, a single scan over an engineered defect (electro-discharge-machined (EDM) notch), will be performed to measure the magnetic field response. Secondly, the complex magnetic field response due to the presence of an engineered defect (milled slot), will be compared using both circular and directional (rectangular) eddy current probes for defect mapping.

As well as using an X-Y scanner to mechanically move the probe over a defect, the use of sensor arrays is becoming increasingly common to measure the spatial variation in magnetic field. This will be investigated to visualise and verify through modelling results, the magnetic field from an eddy current probe.

5.2 Probe Design

The first stage in experimental study is the design of the probe for eddy current excitation. The probes used in the experimental work in this chapter are existing probes used in the experimental inspection setup in the sensor technology research group laboratory (with the addition of a Hall sensor for magnetic field measurement). An overview of the effect of probe design on eddy current inspection is now given. Increasing the inductance of the coil (L), improves sensitivity in eddy current testing. This is related to the dimensions of the coil by equation (5.1) [99].

$$L = Kn^2\pi\left[\left(r_0^2 - r_c^2\right) + \mu_r r_c^2\right]\mu_0 \qquad \textbf{(5.1)}$$

Where the mean radius of the coil is r_0, r_c is the radius of the coil, n is the turns per unit length and K is a dimensionless constant based on the coil length and radius. The coil is wound onto a plastic former for stability, as these are dielectric, with magnetic permeability equal to air, for modelling purposes they can be regarded as air-cored coils. The winding is usually copper (or non-ferromagnetic material) to reduce magnetic hysteresis effects. Equation (5.1) shows that the inductance can be increased by increasing the cross sectional area of the coil, however this increased area reduces

the resolution for detection of small defects. Smaller diameter probes are more useful for inspection of small shallow defects on smooth surfaces (eddy currents concentrated in a small area) and larger diameter probes are more useful for inspection of larger defects or rough surfaces (eddy currents concentrated in a larger area). Optimum detection is achieved when the major axis of the defect is perpendicular to the direction of the eddy currents generated. Adding a ferrite core (increasing μ_r) can give a large increase in impedance and the use of shielded probed (cup-core) increases the sensitivity and concentrates the flux below the area of the coil.

5.3 Sensors

This section will give an overview of the magnetic field sensors used in this work. A Hall sensor is a rectangular section of semi-conductor material, placed in a magnetic field to measure flux density. The magnetic field develops a force on the charge carriers within the material causing them to move. This force is given by equation (5.2).

$$F_e = evB_n \qquad \textbf{(5.2)}$$

Where B_n is normal component of magnetic field, e is the electron charge (-1.6 × 10^{-19} C), F_e is the transverse force acting on the electrons and v is the velocity of the electrons along the wire. This force deflects the charge carriers leading to a defection of electric current flow in the material as shown in figure 5.2 and figure 5.3.

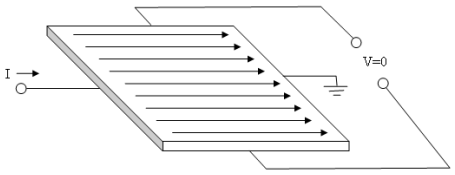

Figure 5.2 Hall probe with no magnetic field [100]

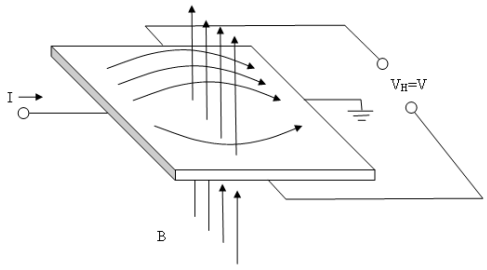

Figure 5.3 Hall probe with magnetic field present [100]

The effect of this is a potential difference at right angles to the current flow (Hall Effect). This potential difference, or Hall voltage V_H, is given by equation (5.3) [100].

$$V = R_H I \frac{B}{t} \quad \textbf{(5.3)}$$

Where R_H is the Hall coefficient (constant for a given material), t is the probe thickness and I is the current, so V is proportional to B (at a fixed temperature).

The use of Hall sensors, provide a cheap and effective way of investigating the presence of defects within materials by measuring the magnetic field change due to the disruption of eddy currents. Hall sensors are also more sensitive to low excitation frequencies than using impedance measurements and therefore more useful in detecting deep or subsurface defects.

5.4 Simulation of Magnetic Field Response to Defects

To investigate defect quantification using the magnetic field response, FEM simulations have been performed. The simulation was performed in COMSOL Multiphysics [101] and set up as shown in table 5.1. The mesh contained 13444 elements with 130108 degrees of freedom. The time taken on an Intel® Quad Core PC with 8GB RAM was approximately 50 seconds per step.

5.4.1 Magnetic field response to defect dimension changes

The change in magnetic field was measured for the following dimensions of defect, length 30mm, width 1mm and height [1,2,3,4] mm, where the probe is scanned across the defect as shown in figure 5.4. The change in real component, $\Re e(B_z)$, and imaginary component, $\Im m(B_z)$, values for the magnetic field due to the presence of the defect is shown in figure 5.5 to figure 5.6. Where it can be seen that the larger defect gives the largest change in magnetic field. To quantify the defects, two separate metrics will be studied.

(i) Height of the response, for both $\Re e(B_z)$, shown in figure 5.7, and $\Im m(B_z)$, shown in figure 5.8.

(ii) Gradient of the response, for both $\Re e(B_z)$, shown in figure 5.9, and $\Im m(B_z)$, shown in figure 5.10.

® Intel Corporation

Coil	
Coil ID	8.3mm
Coil OD	14.3mm
Coil Height	10mm
Turns	500
Coil Lift-off	1mm
Excitation Current	500mA
Excitation Frequency	1kHz
Specimen	
Dimension	400 x 400 x 20mm
Conductivity	17MS/m
Defect	
Length	30mm

Table 5.1 Defect quantification FEM simulation setup

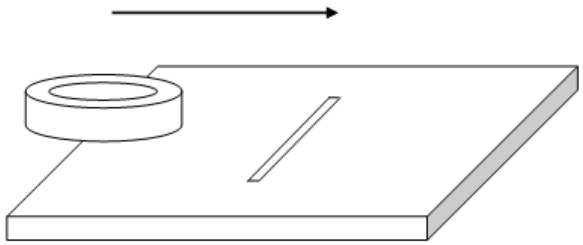

Figure 5.4 FEM geometry for scan across defect

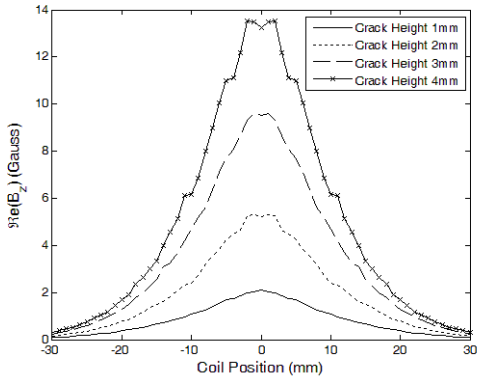

Figure 5.5 $\Re e(B_z)$ for variation in defect height (FEM model)

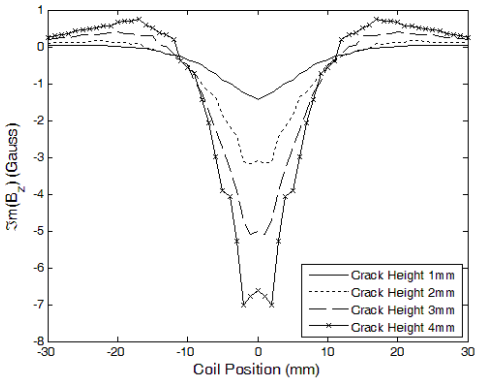

Figure 5.6 $\Im m(B_z)$ for variation in defect height (FEM model)

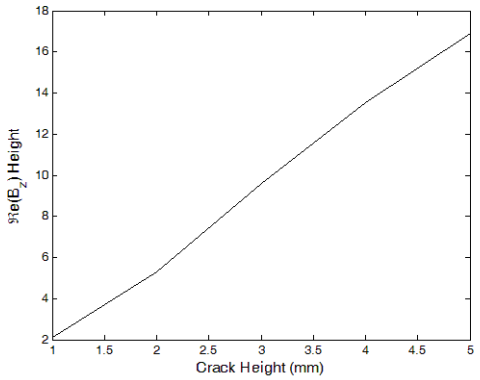

Figure 5.7 Change in height of $\Re e(B_z)$ for different defect heights (FEM model)

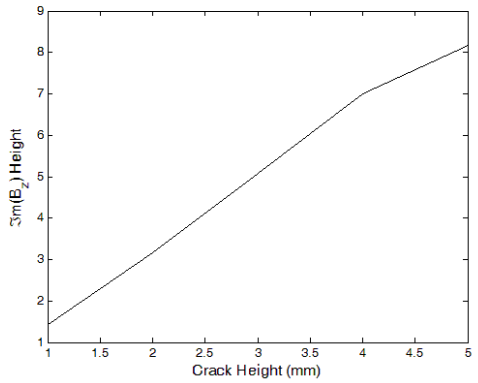

Figure 5.8 Change in height of $\Im m(B_z)$ for different defect heights (FEM model)

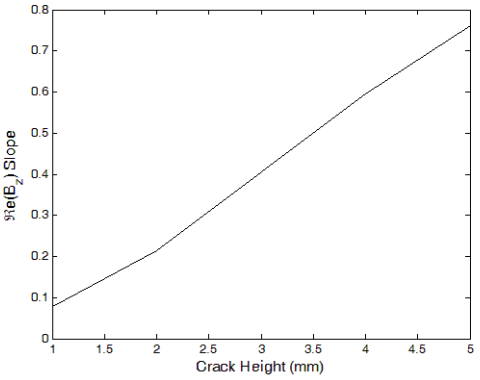

Figure 5.9 Change in slope of $\Re e(B_z)$ for different defect heights (FEM model)

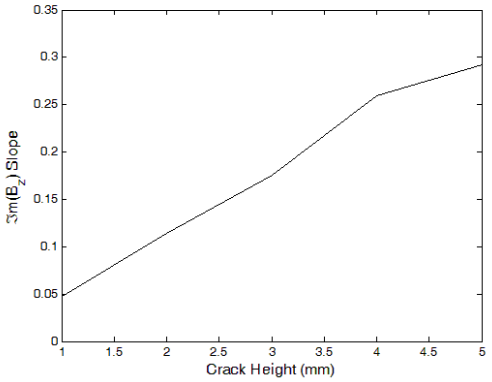

Figure 5.10 Change in slope of $\Im m(B_z)$ for different defect heights (FEM model)

These results show that using both the height and slope of the magnetic field response to defects can be a useful tool in identifying defect properties.

5.4.2 Magnetic field response to lift off changes

The change in magnetic field was measured for different probe lift-offs [1.0,1.5,2.0,2.5] mm. The coil is scanned both along (*y* direction) and across (*x* direction) the defect, as shown in figure 5.11.

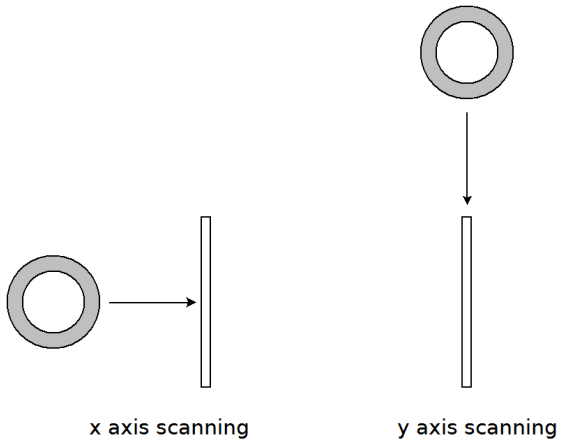

Figure 5.11 Scanning direction in relation to defect direction

Figure 5.12 to figure 5.15 show the effect of lift off on the resulting measured magnetic field measurements, both the real, $\Re e(B_z)$, and imaginary, $\Im m(B_z)$, components. The closer a probe coil is to the surface (smaller lift off), the greater the flux linkage between the coil and the specimen (largest change in magnetic field). The opposite is true as the coil is moved away from the specimen.

These results show that changes in lift off changes the amplitude of the response, however, the change in the field measurements (shape of the response) is constant. Features from the plots such as the slope (to quantify defect width) or the horizontal section of the response, as the coil passes over the edge of the defect (to quantify defect length), can still be used, irrespective of probe lift off.

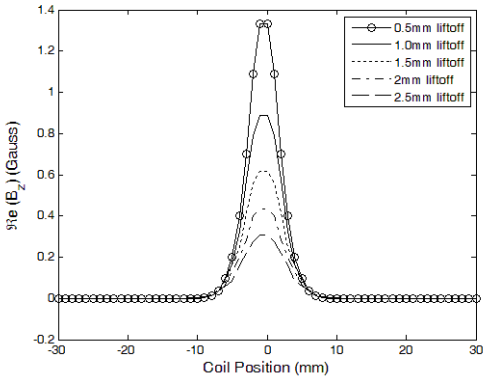

Figure 5.12 $\Re e(B_z)$ for variation in probe lift off for scan across defect – *x* direction (FEM model)

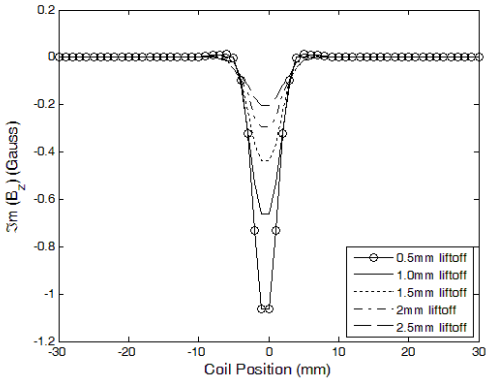

Figure 5.13 $\Im m(B_z)$ for variation in probe lift off for scan across defect – *x* direction (FEM model)

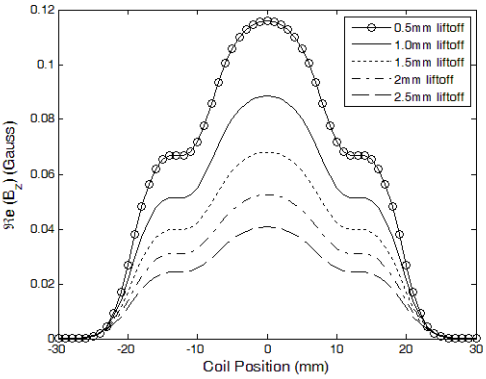

Figure 5.14 $\Re e(B_z)$ for variation in probe lift off for scan along defect – *y* direction (FEM model)

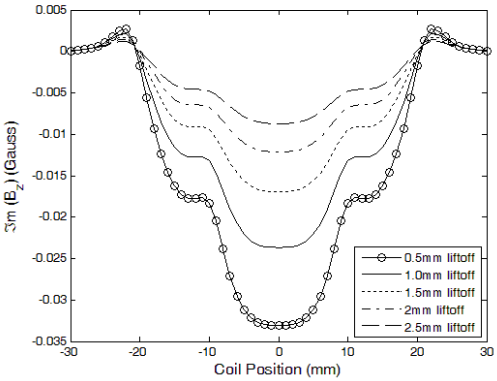

Figure 5.15 $\Im m(B_z)$ for variation in probe lift off for scan across defect – *y* direction (FEM model)

5.4.3 Complementary measurements

As well as displaying the real, $\Re e(B_z)$, and imaginary, $\Im m(B_z)$, components of the magnetic field, to link this study to standard eddy current methods, these will be compared to the resistance and inductance change for the coil being scanned over the defect (slot) as well as the amplitude and phase measurements, shown in table 5.2. This shows that the two types of measurements provide complementary information relating to the presence of a defect.

Measurement	Magnetic Field	Impedance
Real	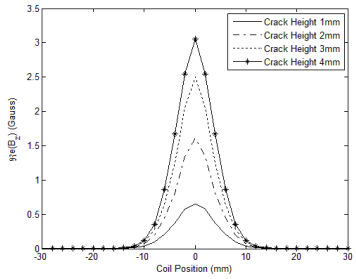	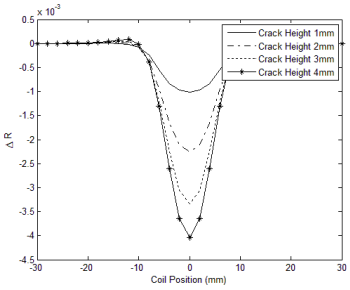
Imaginary	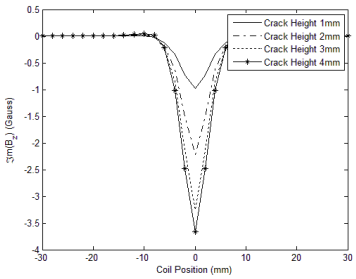	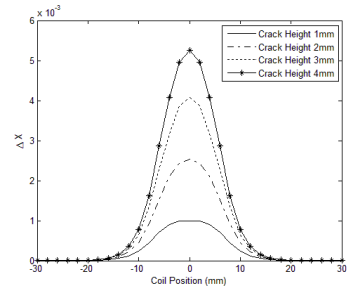
Amplitude	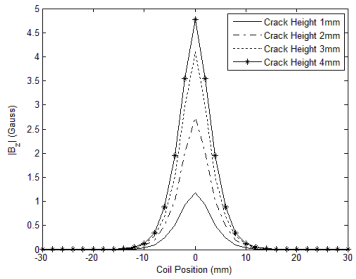	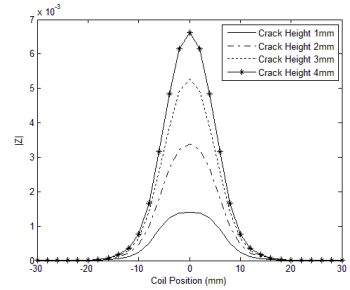
Phase	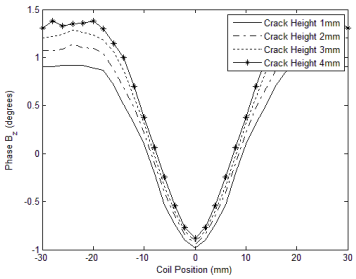	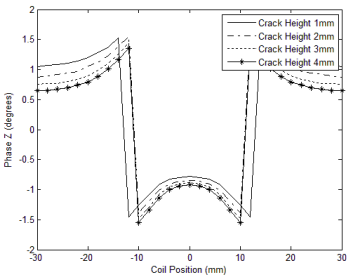
Complex Plane	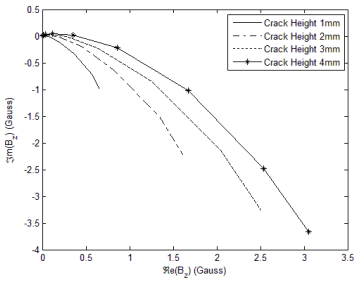	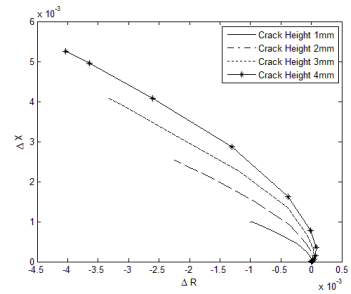

Table 5.2 Magnetic field and impedance complementary measurements

5.5 Magnetic Field Response to Defects using a Single Scan

Thin surface defects such as surface cracks, notches and slots are commonly encountered [21, 40] and this has been simulated using an EDM slot in a conductive (aluminium) plate. Magnetic sensing does not directly measure the physical property of interest, they detect disturbances in the magnetic field (due to the presence of a crack for example), and from the changes in magnetic field we can estimate the dimensions of the defect (as shown previously). This work compares experimental magnetic field measurements with numerical modelling to develop a forward model of the probe response for a defect of a known shape and size. These forward models can be used to create a database of responses for known defects, which can then be used in the inverse problem where a response for a known defect is compared against the response for an unknown defect, obtained from probe measurements (in this case the magnetic field). These measurements are obtained using a single sensor scanned over a defect (in this case the plate containing the defect is moved in relation to the sensor).

5.5.1 FEM simulation

The FEM mesh consists of 70059 elements (639722 degrees of freedom). For each simulation step (a single measurement point at a single frequency), the time-harmonic simulation took 380 seconds. The 3D FEM simulations were performed with a sine wave excitation to the probe and the magnetic field at the Hall sensor position was calculated as the defect (slot) was moved under the stationary coil.

5.5.2 Experimental work

When measuring the magnetic field in eddy current testing there are two magnetic fields present, which are superimposed. The first is the incident magnetic field from the excitation probe and the second is the reaction field associated with the induced eddy currents in the inspected specimen. The eddy current distribution is disturbed when the eddy currents are induced in a region containing a defect. The presence of a defect in conductive specimens can be detected by measuring the change in magnetic field as the sensor is moved from an un-flawed region to one containing a defect. This experimental work uses a Hall sensor to measure the magnetic field, complimentary to existing work using impedance measurements [38, 40, 45], or SQUID [73] to measure the defect response. Magnetic field sensors have a high spatial resolution as the

sensitive area of the sensor is less than 1mm across. This investigation will study two scanning directions to model the probe moving over the defect.

The experiment uses an X-Y scanner table to move a conductive specimen (aluminium plate) containing an EDM notch in relation to a stationary eddy current probe (excitation coil with a Hall sensor to measure magnetic field). The Hall sensor used is a Honeywell SS495A. The dimensions of the eddy current probe are shown in figure 5.16. The excitation current in the coil had the form of a 60mA sine wave excitation at 1 kHz, 2.5 kHz and 5 kHz frequencies. The speed and precision of eddy current inspections can be improved by the use of mechanical systems such as X-Y scanner tables used in these experimental studies.

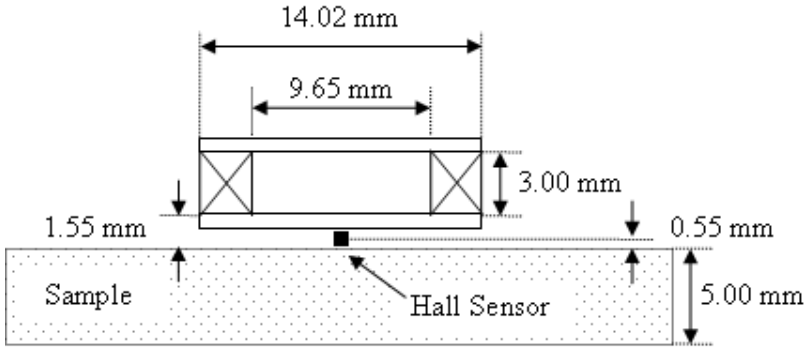

Coil Turns = 123
Coil Lift-off = 1.55 mm
Sensor Lift-off = 0.55 mm

Figure 5.16 Eddy current probe and specimen dimensions

Table 5.3 gives the details of the specimen under test. The X-Y scanner table is shown in figure 5.17 and a block diagram of the data acquisition system shown in figure 5.18.

Plate Material	2024_T3 Aluminium
Plate Thickness	5 mm
Defect (slot) Length	30.086 mm
Defect (slot) Width	0.234 mm
Defect (slot) Depth	4.107 mm
Conductivity	17MS/m

Table 5.3 Experimental specimen details

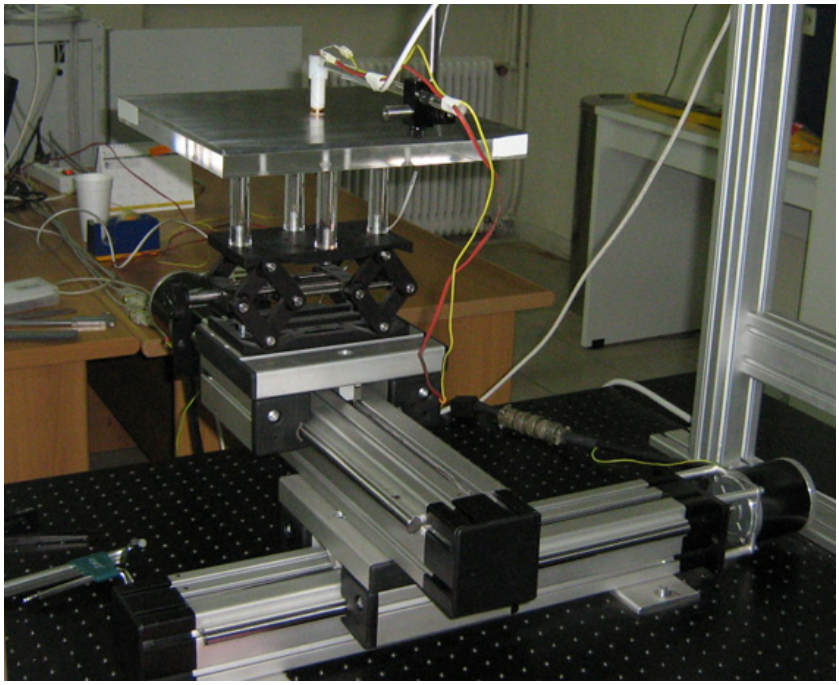

Figure 5.17 X-Y scanner table

For the experimental work, the step-size of the scan 1mm, with a scan length of 60mm (where the centre of defect is at 30mm). A signal generator generates a TTL signal as a frequency reference for the lock-in amplifier; this is then used to detect the voltage signal from the Hall sensor. The signal generator also generates a sine-wave excitation current to drive the eddy current probe coil. The eddy current probe coil is excited using a current source and function generator. At each step, the in-phase, $\Re e(B_z)$, and quadrature, $\Im m(B_z)$, components of the Hall-sensor output voltage along with the coil RMS current are recorded using the lock-in amplifier, where the movement of the X-Y

scanner table and the data acquisition are controlled using LabVIEW© software. These Hall sensor output values are then converted into magnetic flux density (Gauss), using the Hall sensor sensitivity value, Gauss=Voltage/(3.125×10^{-3}).

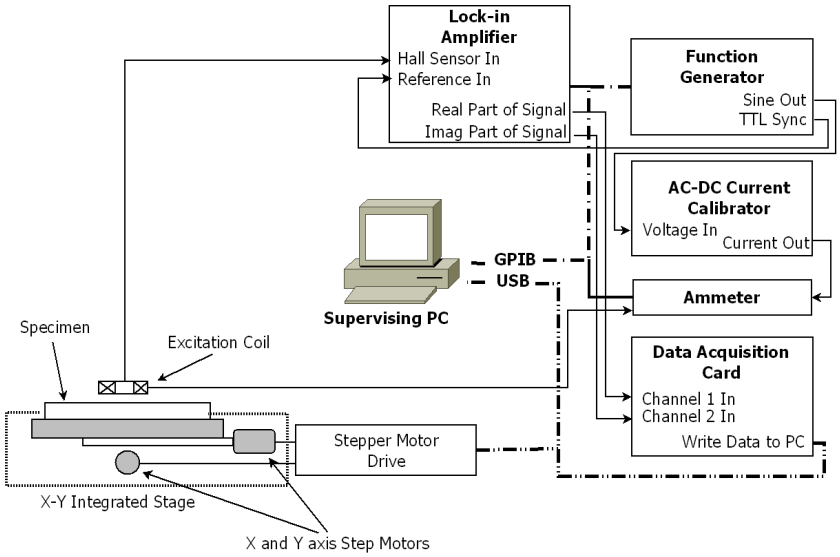

Figure 5.18 Block diagram of data acquisition system

The experimental measurements included two scans, one "across-the-defect" where the specimen was moved perpendicular to the direction of the defect (*x*-axis scan as shown in figure 5.19) and one "along-the-defect" where the specimen was moved in the direction of the defect (*y*-axis scan as shown in figure 5.19). Scanning in two directions is useful for defect quantification as these can provide information on both the length and width of the defect. Performing 2D scans also provides information relating to the orientation of the defect.

Both real and imaginary magnetic field measurements were recorded for the surface defect and subsurface defects (where the plate is turned over, with the defect on the reverse); here the amplitude of the magnetic field is compared, where the amplitude is calculated using equation (5.4).

$$B_z = \sqrt{\Re e(B_z)^2 + \Im m(B_z)^2} \qquad \textbf{(5.4)}$$

These experimental values will then be compared with the numerical simulation results.

© National Instruments Corporation

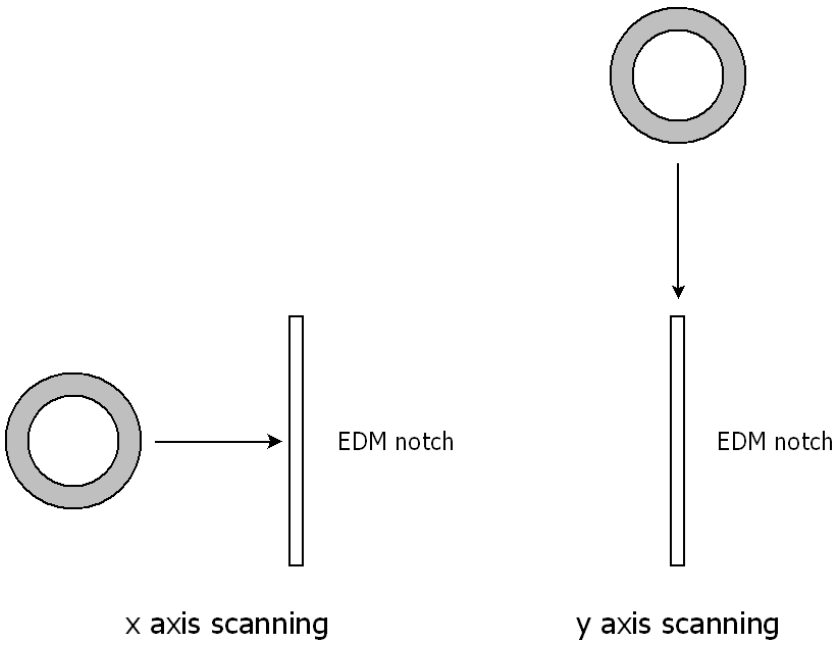

Figure 5.19 Scanning direction in relation to defect direction

5.5.3 Results and discussion

The FEM simulation results are compared with the experimental results from the X-Y scanner table. Figure 5.20 to figure 5.23 shows the amplitude of the magnetic field change due to the defect as a function of scan distance, which is the distance between the centre of the coil and the centre of the defect, for the following scenarios.

1. Scan across (*x*-axis in figure 5.19) a surface defect.

2. Scan across a subsurface defect.

3. Scan along (*y*-axis in figure 5.19) a surface defect.

4. Scan along a subsurface defect.

Where the change in magnetic field is calculated using equation (5.5).

$$B_{result} = B_{crack} - B_{no\ crack} \qquad \textbf{(5.5)}$$

The flat areas in the scans along the defect (in figure 5.22 and figure 5.23) are where the centre of the coil (i.e. inside the coil inner diameter) is moving over the ends of the crack [21]. Here the eddy current strength is zero, so the magnetic field does not change. This feature gives an indication of the length of the defect, in this case 30.086 mm.

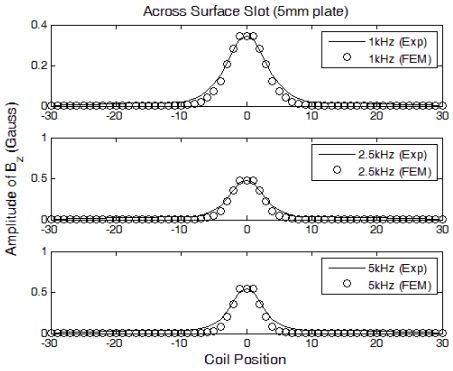

Figure 5.20 Scan across a surface defect

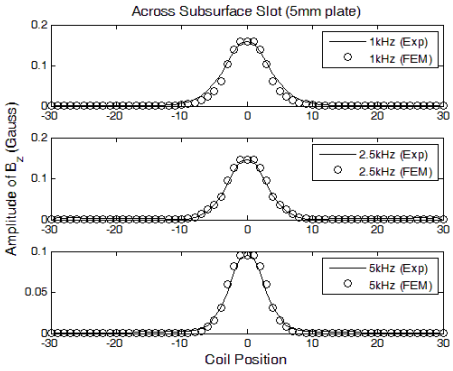

Figure 5.21 Scan across a subsurface defect

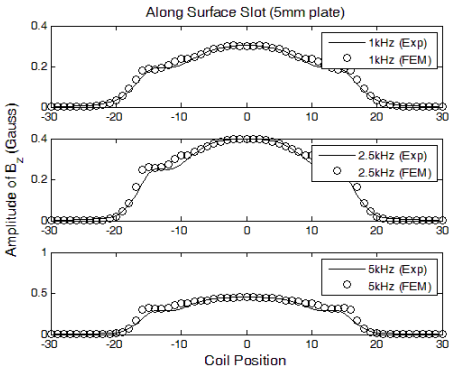

Figure 5.22 Scan along a surface defect

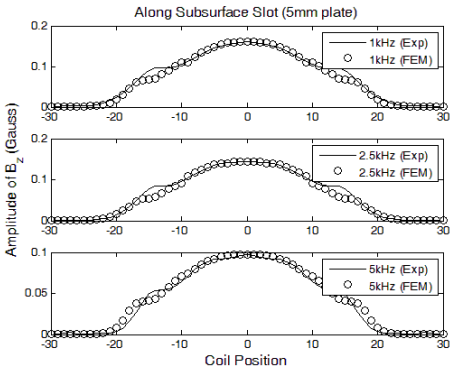

Figure 5.23 Scan along a subsurface defect

The correlation between the two sets of results is shown in figure 5.24 to figure 5.27, where the solid line indicates a match between the two sets of data.

The correlation values between the FEM simulated values and the experimental results are shown in table 5.4 (where larger indicates the better correlation). The correlation coefficient between experimental (e) and FEM (f) is given by equation (5.6).

$$r_{ef} = \frac{\sum_{i=1}^{n}(e_i - \bar{e})(f_i - \bar{f})}{\sqrt{\sum_{i=1}^{n}(e_i - \bar{e})^2 \sum_{i=1}^{n}(f_i - \bar{f})^2}} \qquad \textbf{(5.6)}$$

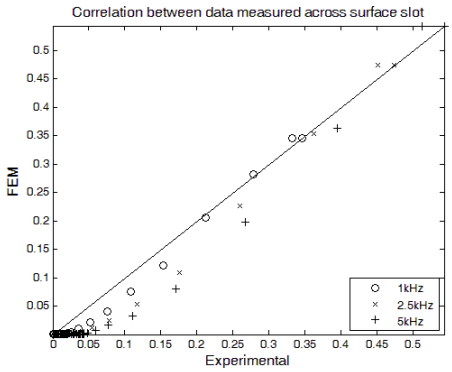

Figure 5.24 Correlation for scan across a surface defect

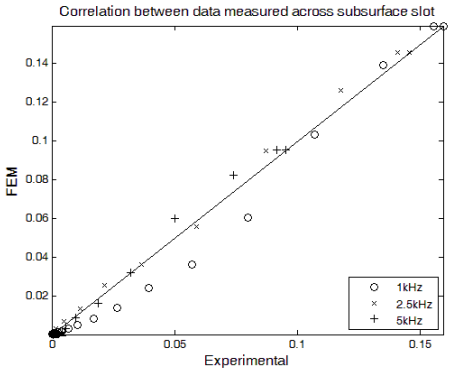

Figure 5.25 Correlation for scan across a subsurface defect

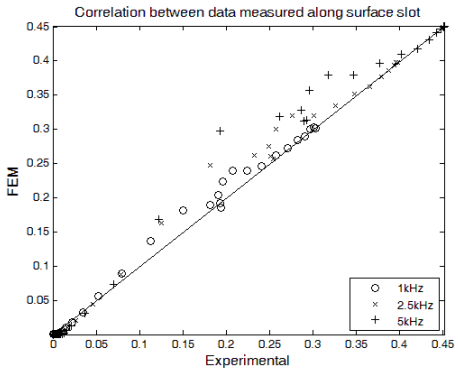

Figure 5.26 Correlation for scan along a surface defect

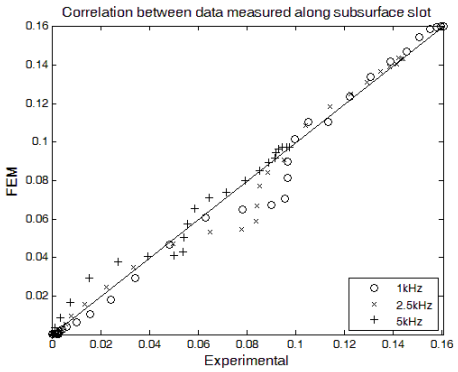

Figure 5.27 Correlation for scan along a subsurface defect

Frequency (kHz)	Across Surface Defect	Along Surface Defect	Across Subsurface Defect	Along Subsurface Defect
1	0.9942	0.9961	0.9914	0.9931
2.5	0.9901	0.9938	0.9980	0.9912
5	0.9853	0.9898	0.9969	0.9917

Table 5.4 Correlation coefficient between the experimental and FEM results

The results shown in figure 5.24 to figure 5.27 and table 5.4, show there is a good agreement between the experimental and simulation results.

5.6 Investigation of Complex Magnetic Field Measurements and Directional Excitation for Defect Mapping

Rectangular (directional) coils have advantages over circular coils as they generate directional eddy currents parallel with the sides of the coil [102]. Thus, directional eddy current flow will be interrupted in different ways depending on the orientation of the defect in relation to the direction of the eddy current flow. In contrast, circular coils generate eddy currents in the azimuthal direction, so the disruption to the eddy current will not be dependant on the orientation of the defect.

Various researchers have studied models of non-circular coils. Panas and Papayiannakis [103] used an elliptic coil for excitation, giving a more directional dependant field than a circular coil. Sadeghi and Salemi [104] and Lei *et al.* [105] present theoretical models for arbitrarily shaped coils. Both Theodoulidis and Kriezis [106] and also Fava and Ruch [107] present models for rectangular coils and Tian *et al.* [108] compared the responses for a parallel circular coil and perpendicular rectangular coil for surface scratch detection, where the rectangular coil gave superior results at higher lift-offs.

It is commonplace in eddy current NDE to study the change in impedance of the test probe as it is scanned over a specimen. The response (voltage in the coil) of this is a complex value relating the change in resistance with the change in reactance (impedance change). This work follows a similar concept in that the complex response is measured relating the change in the real value of the *z*-component of the magnetic field, $\Re e(B_z)$, with the change in the imaginary value of the *z*-component of the magnetic field, $\Im m(B_z)$.

Driven by the applications of defect mapping for complex geometrical shapes [109], a study and comparison is made of the response from a circular and rectangular shaped eddy current probe which is scanned over the surface of a specimen containing a defect using an X-Y scanning table.

5.6.1 Simulation study of complex magnetic field measurements

FEM simulations are performed for both a rectangular and circular coil being scanned over the area of a defect (crack). The scan orientation (for both the simulation and experimental work) is shown in figure 5.28.

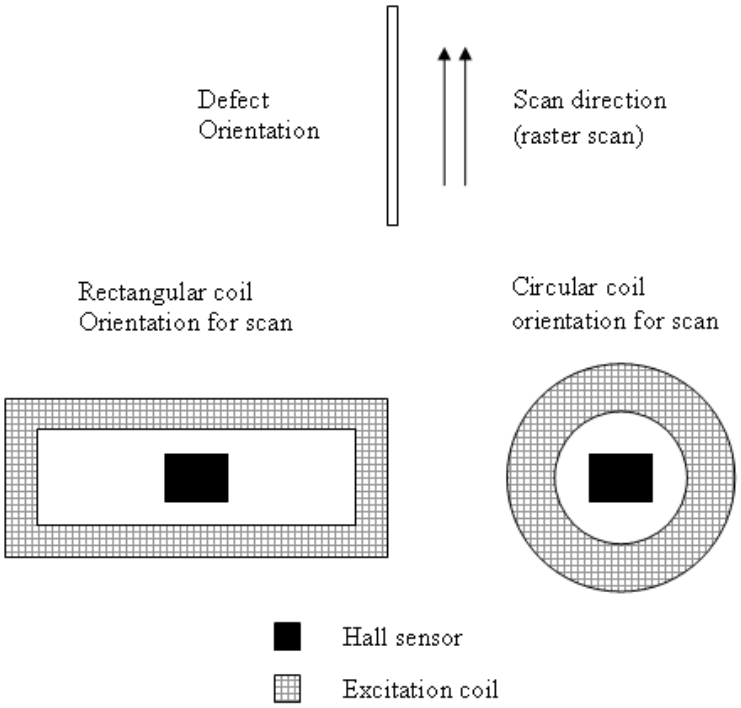

Figure 5.28 Experimental probe scan orientation

To compare the response for each case, $\Re e(B_z)$ and $\Im m(B_z)$ measurement for the circular and rectangular coil, plots showing the rate of change of magnetic field due to the presence of the defect, as the coil is scanned across the defect are shown in figure 5.29 and normalised in figure 5.30. These results show that the response of the rectangular coil is more closely related to the shape of the defect than the circular coil, also the $\Im m(B_z)$ response is also more closely related to the defect than $\Re e(B_z)$, which is quantified by the steeper slope.

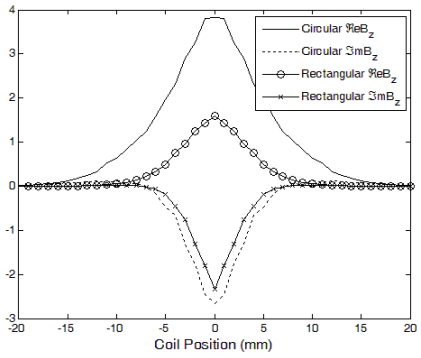

Figure 5.29 Complex magnetic field measurements from circular and rectangular coils (FEM model)

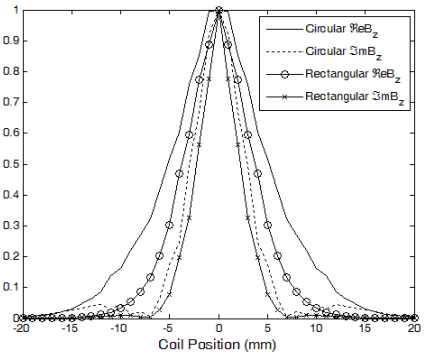

Figure 5.30 Normalised complex magnetic field measurements from circular and rectangular coils (FEM model)

5.6.2 Eddy current system transformer model

The equivalent mutual impedance between an excitation coil and a specimen has been developed in the area of eddy current testing for the purposes of verifying the interaction between an excitation coil and a specimen through experimental and numerical study. Impedance is the total opposition that a circuit presents to alternating current and may include resistance, R, and reactance, X. The presence of a defect, or indeed the presence of a conductive specimen will change the eddy current distribution causing a change in the impedance of the excitation coil [110]; this may be either a single excitation coil or the change in mutual impedance between a driver coil and a pickup coil. Bihan [111] developed a transformer model to characterise how plate thickness and coupling affected eddy current measurements. Tian *et al.* [112] used a transformer model to use the change in mutual impedance between the excitation coil and a conductive specimen to overcome inhomogeneity in eddy current proximity sensors. The transformer equivalent circuit is shown in figure 5.31 and figure 5.32.

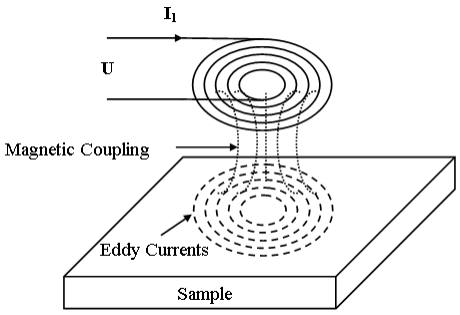

Figure 5.31 Eddy current probe over specimen

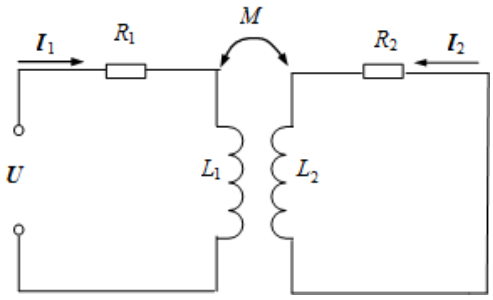

Figure 5.32 Transformer equivalent circuit

The magnetic field produced by the probe will intersect the specimen and create current flow. The induced current flow in the specimen will have its own magnetic field, which will interact with the magnetic field of the probe. The two self-inductances are represented by L_1 and L_2. The values of L_1 and L_2 depend on the geometry of the coil and the conductivity of the material. The magnetic flux linkage through the probe, Ψ_1, is given by equation (5.7) and the magnetic flux linkage in the specimen, Ψ_2, is given by equation (5.8).

$$\Psi_1 = L_1 I_1 + M I_2 \tag{5.7}$$

$$\Psi_2 = L_2 I_2 + M I_1 \tag{5.8}$$

Based on Kirchhoff's voltage law, the equations for the two circuits are given by equation (5.9) and equation (5.10), respectively.

$$I_1 R_1 + j\omega I_1 L_1 - j\omega I_2 M = U \tag{5.9}$$

$$I_2 R_2 + j\omega I_2 L_2 - j\omega I_1 M = 0 \tag{5.10}$$

Where R_1, L_1 is the resistance and inductance of coil of eddy current probe, respectively; R_2, L_2 is the equivalent resistance and inductance of the eddy current loop in specimen, respectively. L_2 reflects the eddy current flow, as the reactance will change as the distance the eddy currents flow around the defect changes, hence it will disclose the shape of defect. The work in [113] uses this phenomenon for defect depth estimation. U is the (alternating) probe excitation voltage; I_1 is the alternating current in the probe and I_2 is in induced eddy current in the specimen. M is the mutual

inductance (coupling coefficient) between the probe and the induced eddy currents, relating to the distance between the probe and the specimen (lift-off), which decreases with increasing lift-off. The impedance of the probe is given by equation (5.11).

$$Z_1 = R_1 + j\omega L_1 \tag{5.11}$$

The equivalent impedance for the probe and the specimen is given by equation (5.12).

$$Z_{eq} = \frac{U}{I_1} = \frac{I_1 R_1 + j\omega I_1 L_1 - j\omega I_2 M}{I_1} \tag{5.12}$$

Substituting $I_2 = \dfrac{j\omega I_1 M}{\left(R_2 + j\omega L_2\right)}$ into equation (5.12) gives equation (5.13).

$$Z_{eq} = \frac{I_1 R_1 + j\omega I_1 L_1 - j\omega M\left(j\omega I_1 M\right)}{I_1\left(R_2 + j\omega L_2\right)} = \frac{R_1 + j\omega L_1 + \omega^2 M^2}{R_2 + j\omega L_2} \tag{5.13}$$

This is simplified to equation (5.14).

$$Z_{eq} = Z_1 + \frac{\omega^2 M^2}{R_2 + j\omega L_2} \tag{5.14}$$

Expressing equation (5.14) as a complex number gives equation (5.15).

$$Z_{eq} = R_1 + \frac{\omega^2 M^2}{R_2{}^2 + \omega^2 L_2{}^2} R_2 + j\omega\left[L_1 - \frac{\omega^2 M^2}{R_2{}^2 + \omega^2 L_2{}^2} L_2 \right] \tag{5.15}$$

The equivalent resistance and reactance of the excitation coil and the specimen are given by equation (5.16) and equation (5.17), respectively

$$R_{eq} = R_1 + \frac{\omega^2 M^2}{R_2{}^2 + \omega^2 L_2{}^2} R_2 \tag{5.16}$$

$$L_{eq} = L_1 - \frac{\omega^2 M^2}{R_2{}^2 + \omega^2 L_2{}^2} L_2 \tag{5.17}$$

The induced eddy current increases the real part of the impedance and reduces the imaginary part of the impedance. The equivalent resistance R_{eq} is greater than the original resistance R_1 of the probe and the equivalent inductance L_{eq} is less than the original inductance L_1 of the probe. If the magnetic coupling is reduced (lower

magnetic flux linkage between the coil and specimen), there is less secondary magnetic field to oppose the primary magnetic field, increasing the reactance. This change in magnetic flux linkage can be detected using either impedance or magnetic field measurement.

5.6.3 Eddy current system and experimental work

The experiment uses an X-Y scanner to scan an eddy current probe (excitation coil with a Hall sensor to measure magnetic field) over an engineered defect (milled slot) in a conductive specimen. The dimensions of the two probes used in the experimental study are shown in table 5.5.

Rectangular Coil		**Circular Coil**	
Coil Length	24mm	Coil ID	8.3mm
Coil Width	10mm	Coil OD	14.3mm
Coil Height	10mm	Coil Height	10mm
Coil Thickness	2mm	Coil Thickness	3mm
Turns	250	Turns	500
Lift-Off	2mm	Lift-Off	1mm

Table 5.5 Dimensions of experimental eddy current probe coils

The specimen is a section of aluminium plate containing an engineered surface breaking defect. The parameters of the aluminium specimen and the defect are shown in table 5.6 and a photograph of the defect is shown in figure 5.33.

Plate Thickness	10mm
Defect (slot) Length	25mm
Defect (slot) Width	1mm
Defect (slot) Depth	2mm
Specimen Conductivity	27MS/m

Table 5.6 Experiment specimen details

Figure 5.33 Photograph of engineered slot defect

In this experiment, the probe is moved over the specimen using the X-Y scanner. The scanning system is a CNC-Technik High-Z S-400 CNC machine controlling four Nanotech ST5918L2008 stepper motors (two on the *x*-axis, and one each on the *y*-axis and *z*-axis). The scan step size for the acquisition is 1mm; with a scan length of 40mm and a scan width of 20mm, (800mm^2 scan area). The system is controlled using MATLAB R2009a Data Acquisition Toolbox©, which provides a control signal for the stepper motors, coil excitation for the QinetiQ TrecScan® system and stores the magnetic field measurement (both the real, $\Re e(B_z)$, and imaginary, $\Im m(B_z)$ values) at each point on the scan. The data acquisition code calculates these parameters by comparing the acquired data with a reference sine-wave to calculate the phase (lock-in). The magnetic field is measured using a Hall sensor (Honeywell SS495A). The X-Y scanner system is shown in figure 5.34 and figure 5.35.

© The Mathworks, Inc.

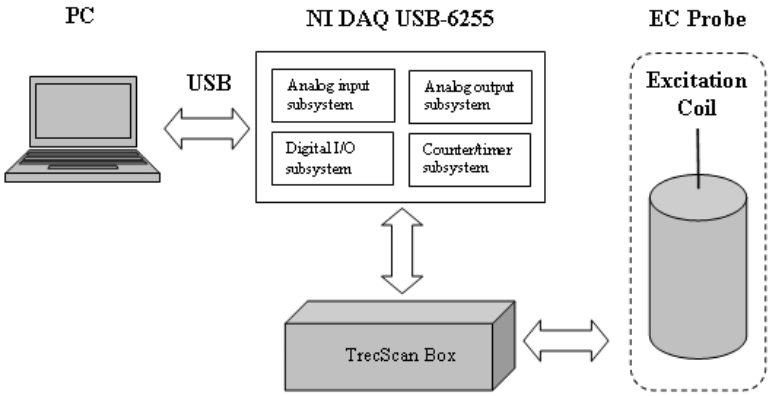

Figure 5.34 Scanning system setup

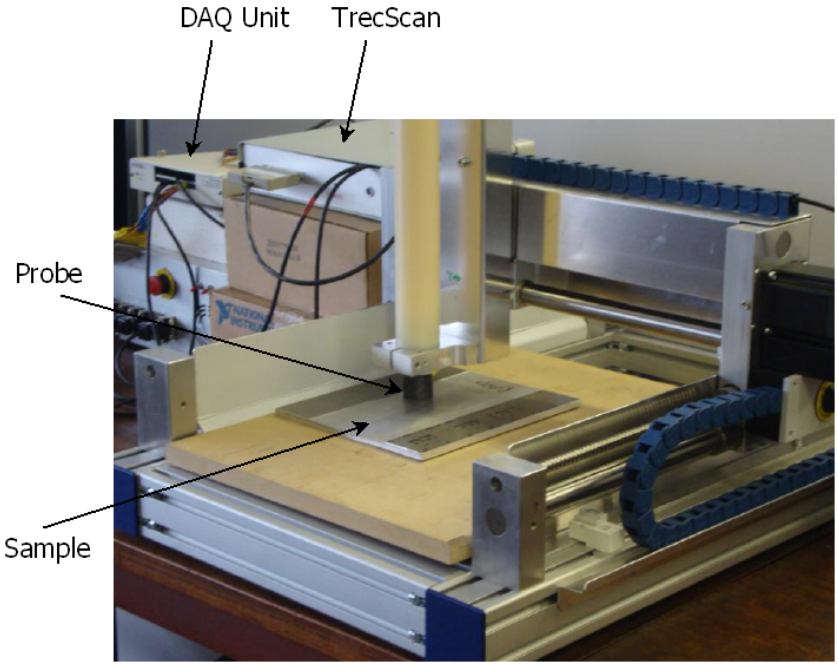

Figure 5.35 Photograph of X-Y scanning system

The stepper motors are controlled using digital pulses via a parallel port connection. The coil excitation and Hall sensor read-out is provided by a TrecScan® system, with a multi-frequency current-driven excitation (500Hz, and 1kHz). The TrecScan® system is designed for transient (pulsed) eddy currents and the excitation circuits contain low-pass filters for the square wave current excitation. This placed a restriction on the experimental frequencies used in the study, which are lower than conventional multi-frequency eddy current methods (can range up to 10MHz). Comparing the two sets of

results for 500Hz and 1kHz, the higher frequency gives a better correlation with defect shape (as expected due to the skin effect).

5.6.4 Results and discussion

The specimen in figure 5.33 has been scanned by the scanning system shown in figure 5.35. The magnetic field responses have been captured and visualised in the following figures. The response from a circular coil is given in figure 5.36 to figure 5.39 (real component, $\Re e(B_z)$, and imaginary component, $\Im m(B_z)$, at 500Hz and 1kHz excitation frequency). The response from a rectangular coil is given in figure 5.40 to figure 5.43 (real component, $\Re e(B_z)$, and imaginary component, $\Im m(B_z)$, at 500Hz and 1kHz excitation frequency).

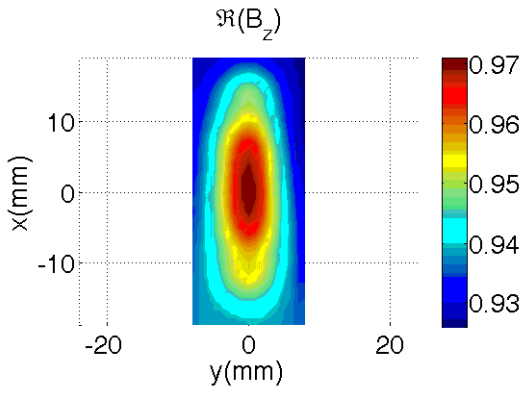

Figure 5.36 Experimental $\Re e(B_z)$ surface scan with circular coil (500Hz)

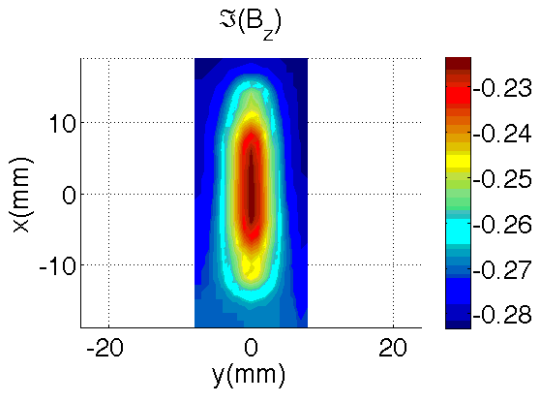

Figure 5.37 Experimental $\Im m(B_z)$ surface scan with circular coil (500Hz)

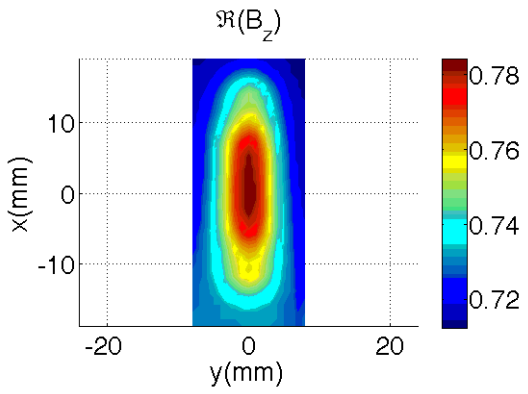

Figure 5.38 Experimental $\Re e(B_z)$ surface scan with circular coil (1kHz)

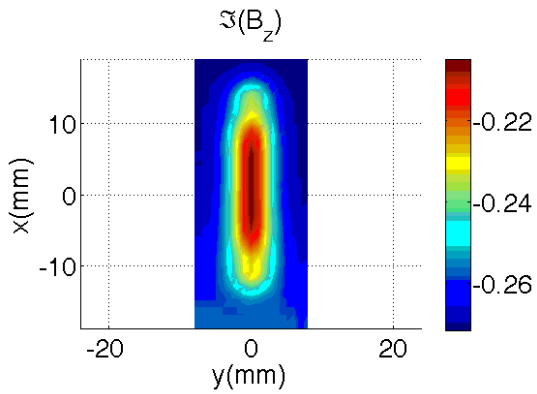

Figure 5.39 Experimental $\Im m(B_z)$ surface scan with circular coil (1kHz)

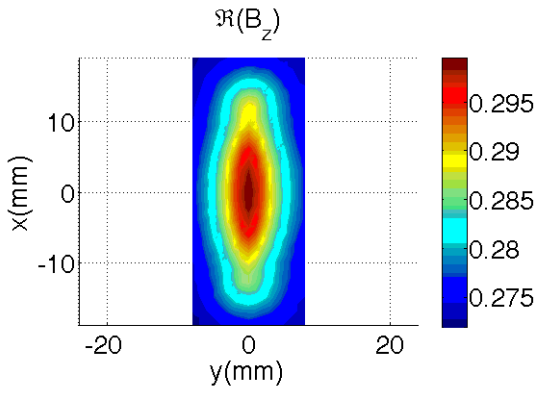

Figure 5.40 Experimental $\Re e(B_z)$ surface scan with rectangular coil (500Hz)

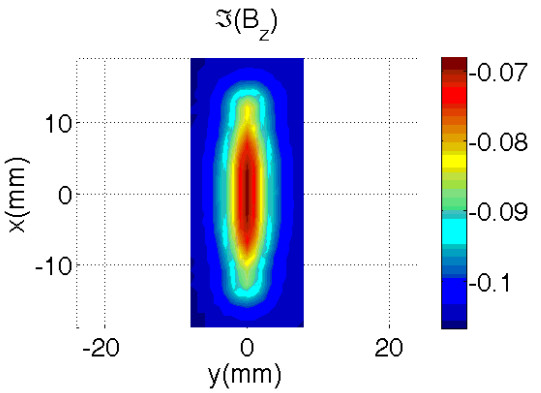

Figure 5.41 Experimental $\Im m(B_z)$ surface scan with rectangular coil (500Hz)

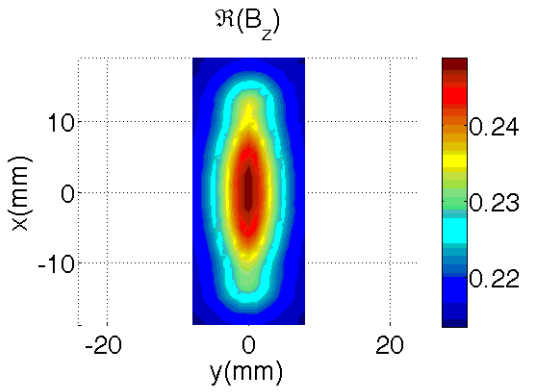

Figure 5.42 Experimental $\Re e(B_z)$ surface scan with rectangular coil (1kHz)

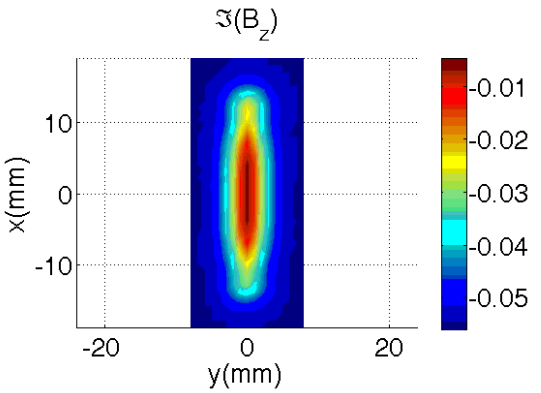

Figure 5.43 Experimental $\Im m(B_z)$ surface scan with rectangular coil (1kHz)

As illustrated in these experimental studies, the imaginary component, $\Im m(B_z)$, of the magnetic field has a faster rate of change (steeper slope) when compared to the real component, $\Re e(B_z)$, when scanned over a defect, which is similar to other experimental results [113]. In other words, the imaginary component measurements, $\Im m(B_z)$, can provide better correlation with the shape of the defect (defect dimensions, 25mm × 1mm, centred at (0, 0)), where the shape of the imaginary component response is similar in shape to the slot, i.e. more narrow and elongated due to a steeper slope, when compared with the real component, $\Re e(B_z)$, or the amplitude. To illustrate this, comparing the amplitude of the magnetic field measurement using a circular probe

(figure 5.44), similar to the measurements from the previous experimental study, with the complex magnetic field measurement, $\Im m(B_z)$, using the rectangular shaped probe (figure 5.45), it can be seen that the complex measurement gives an improved correlation with the shape of the defect (the outline of which is superimposed on each figure).

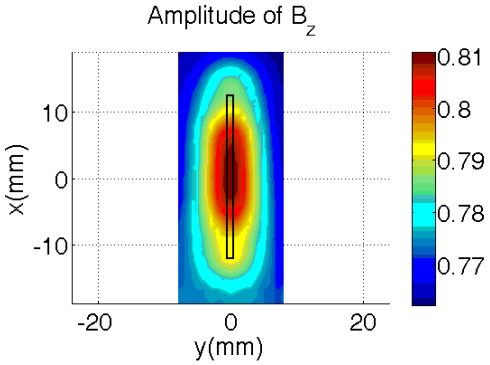

Figure 5.44 Experimental B_z measurements from surface scan with circular coil (showing outline of 25mmx1mm defect)

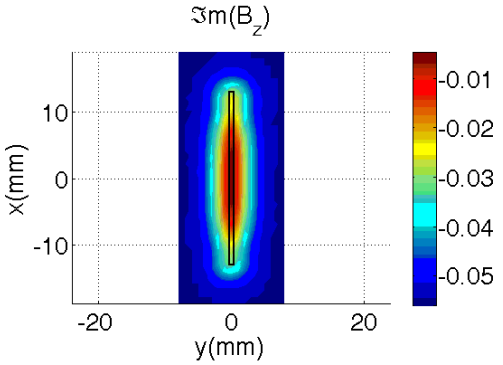

Figure 5.45 Experimental $\Im m(B_z)$ measurements from surface scan with rectangular coil (showing outline of 25mmx1mm defect)

To show the difference in slope between the real component, $\Re e(B_z)$, and imaginary component, $\Im m(B_z)$, the results for the circular coil (at 500Hz and 1kHz excitation frequency) are shown in figure 5.46 to figure 5.49 and the results for the rectangular coil (at 500Hz and 1kHz excitation frequency) in figure 5.50 to figure 5.53. These results show the normalised value of B_z in arbitrary units (au).

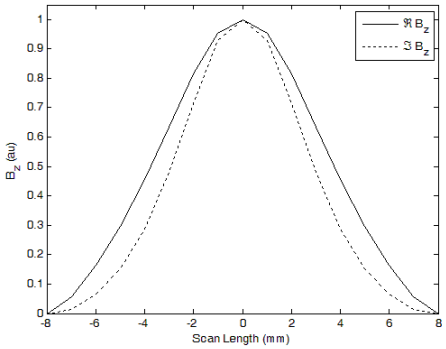

Figure 5.46 Comparison of experimental $\Re e(B_z)$ and $\Im m(B_z)$ for scan across the defect with a circular coil (500Hz)

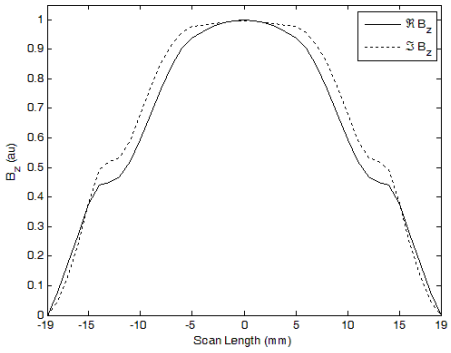

Figure 5.47 Comparison of experimental $\Re e(B_z)$ and $\Im m(B_z)$ for scan along the defect with a circular coil (500Hz)

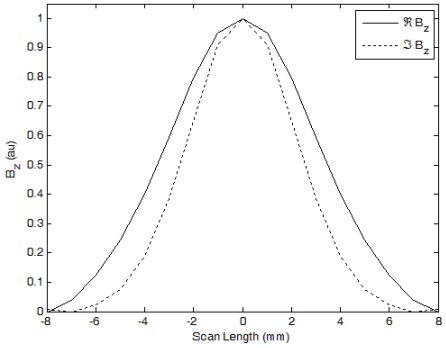

Figure 5.48 Comparison of experimental $\Re e(B_z)$ and $\Im m(B_z)$ for scan across the defect with a circular coil (1kHz)

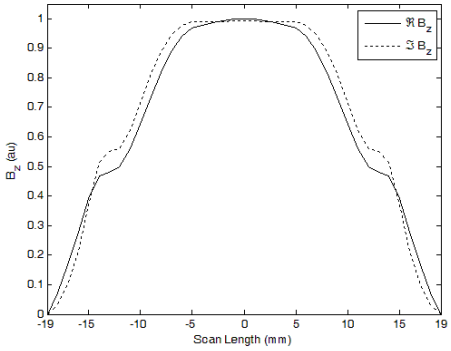

Figure 5.49 Comparison of experimental $\Re e(B_z)$ and $\Im m(B_z)$ for scan along the defect with a circular coil (1kHz)

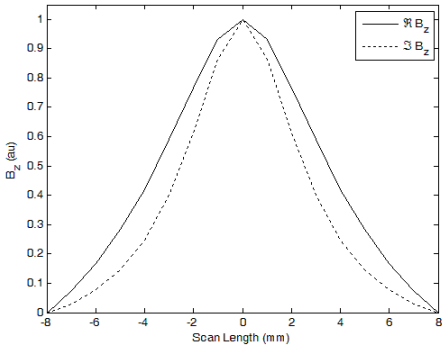

Figure 5.50 Comparison of experimental $\Re e(B_z)$ and $\Im m(B_z)$ for scan across the defect with a rectangular coil (500Hz)

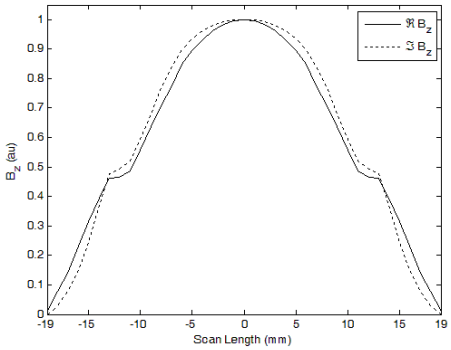

Figure 5.51 Comparison of experimental $\Re e(B_z)$ and $\Im m(B_z)$ for scan along the defect with a rectangular coil (500Hz)

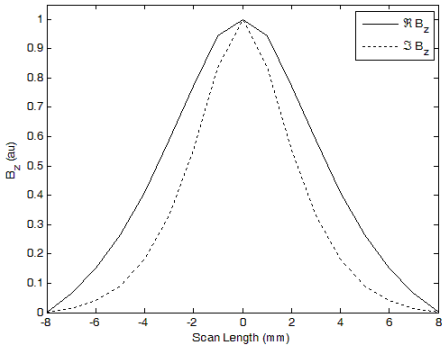

Figure 5.52 Comparison of experimental $\Re e(B_z)$ and $\Im m(B_z)$ for scan across the defect with a rectangular coil (1kHz)

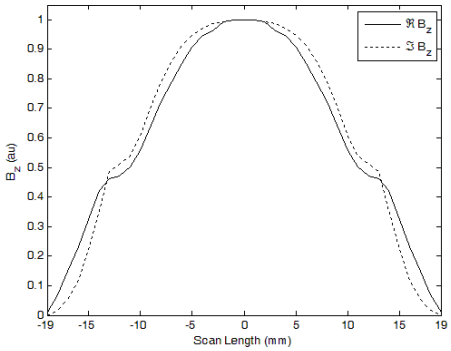

Figure 5.53 Comparison of experimental $\Re e(B_z)$ and $\Im m(B_z)$ for scan along the defect with a rectangular coil (1kHz)

To quantify these results, the gradient of each component, $\Re e(B_z)$ and $\Im m(B_z)$, for each of the scans has been calculated as shown in table 5.7. For each case, the gradient is larger (steeper slope) for the imaginary $\Im m[B_z(au)]$ component compared with the real component $\Re e[B_z(au)]$, additionally for each scan, the gradient is larger when using the rectangular coil, compared with the scan using the circular coil. In addition, as the excitation frequency is increased, the gradient is increased around the defect due to the skin effect (eddy currents are concentrated around the surfaces of the slot).

Scan	Parameter	Value		Ratio between the slope of $\Re e$ and $\Im m$ values	
		500Hz	1kHz	500Hz	1kHz
Across the defect with the circular coil	$\frac{d}{dx}\Re e[B_z(au)]$	0.18	0.20	1.30	1.33
	$\frac{d}{dx}\Im m[B_z(au)]$	0.23	0.27		
Along the defect with the circular coil	$\frac{d}{dy}\Re e[B_z(au)]$	0.10	0.11	1.31	1.38
	$\frac{d}{dy}\Im m[B_z(au)]$	0.14	0.16		
Across the defect with the rectangular coil	$\frac{d}{dx}\Re e[B_z(au)]$	0.18	0.19	1.45	1.53
	$\frac{d}{dx}\Im m[B_z(au)]$	0.25	0.28		
Along the defect with the rectangular coil	$\frac{d}{dy}\Re e[B_z(au)]$	0.09	0.10	1.37	1.39
	$\frac{d}{dy}\Im m[B_z(au)]$	0.13	0.13		

Table 5.7 Rate of change of magnetic field for each scan (Experimental results)

5.7 Sensor Array for Spatial Magnetic Field Measurement

This section gives an overview of the use of sensor arrays for magnetic field measurement. The sensor array will be used to experimentally measure the magnetic field distribution of an eddy current probe [114], which will then be verified using analytical and numerical models. Sensor arrays have been used in many applications, such as lap joint inspection in aircraft [115], measuring the spatial distribution of the impedance change due to a volumetric defect [116] and detection of subsurface defects [15], where Hall sensors and GMR sensors are commonly used [69]. Measuring

magnetic flux leakage from defects, specifically quantifying the defect volume using the rate of change of magnetic field was done using a sensor array, called a magnetic camera (used in this work) [64], updated with current sheet excitation [11]. Similar work has been performed using the "magnetovision" system [117].

5.7.1 Magnetic camera

The Magnetic camera contains an 8×8 array of 64 Hall Sensors (model Samsung HE12AF1U12) with a spatial resolution of 3.5mm, as shown in figure 5.54. The dimensions of the sensor array are 27.5mm × 27.5mm. This array of sensors can be used to produce an "image" of the z-component of the magnetic field, using the Hall voltage measured from the sensors.

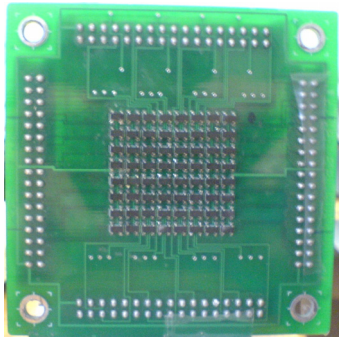

Figure 5.54 Magnetic camera

The Samsung HE12AF1U12 Hall sensors have a sensitivity of ~0.6mV/Gauss, the signal from the sensors pass through an amplification stage (gain ≈ 900), which gives an output of 0.52V/Gauss, The voltage is acquired using a National Instruments NI PCI-6255 data acquisition card and the data processing is performed using the MATLAB R2009a Data Acquisition Toolbox.

5.7.2 Visualisation and verification of eddy current probe magnetic field

The magnetic camera sensor array will be used to visualise and experimentally verify the magnetic field from an eddy current probe; the parameters of the probe are shown in table 5.8.

Coil ID	16.83mm
Coil OD	21.90mm
Coil Height	8.50mm
Turns	1700
Coil Lift-off	0.64mm
Excitation Current	22mA
Excitation Frequency	100Hz

Table 5.8 Probe coil specifications

The magnetic field is visualised by measuring the z-component of the magnetic field (B_z), as shown in figure 5.55. The measurement points for comparison with the modelling results are shown in figure 5.56.

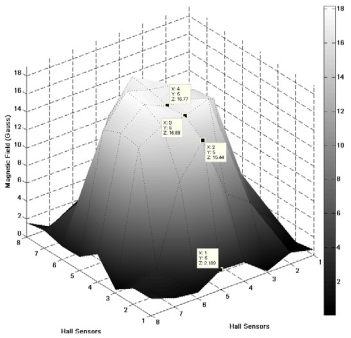

Figure 5.55 Visualisation of magnetic field (Experimental Measurements)

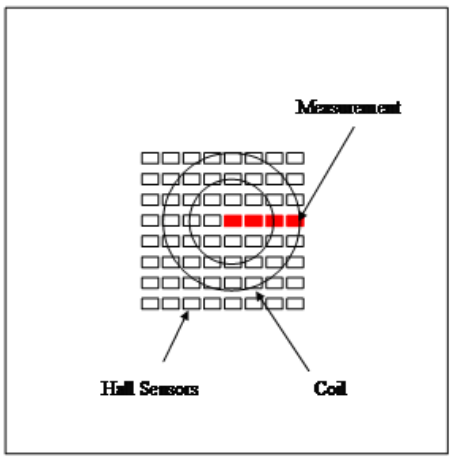

Figure 5.56 Measurement positions for comparison

These experimental results will be compared with numerical (FEM) and analytical (ETREE) models [30]. The ETREE model is extended from predicting the magnetic field at a single point, to modelling the magnetic field distribution due to an eddy current probe in air. By varying r in equation (5.18) to equation (5.20), the magnetic field at the point (r,z) over the surface of the coil can be acquired.

$$B^{(1)}(r,z) = \mu_0 i_0 \sum_{i=1}^{\infty} \left[J_1(q_i r)\hat{r} + J_0(q_i r)\hat{z} \right] \frac{\chi(q_i r_1, q_i r_2)}{\left[(q_i h) J_0(q_i h) \right]^2 q_i} \left(e^{q_i z_2} - e^{q_i z_1} \right) e^{-q_i z} \tag{5.18}$$

$$B^{(2)}(r,z) = \mu_0 i_0 \sum_{i=1}^{\infty} \left[-J_1(qr)\hat{r} + J_0(qr)\hat{z} \right] \frac{\chi(q_i r_1, q_i r_2)}{\left[(q_i h) J_0(q_i h) \right]^2 q_i} \left(e^{-qz_1} - e^{-qz_2} \right) e^{q_i z} \tag{5.19}$$

$$B^{(1-2)}(r,z) = \mu_0 i_0 \sum_{i=1}^{\infty} \begin{bmatrix} \left(e^{q_i (z-z_2)} - e^{-q_i (z-z_1)} \right) J_1(q_i r)\hat{r} \\ -\left(e^{q_i (z-z_2)} - e^{-q_i (z-z_1)} \right) J_0(q_i r)\hat{z} \end{bmatrix} \frac{\chi(q_i r_1, q_i r_2)}{\left[(q_i h) J_0(q_i h) \right]^2 q_i} \tag{5.20}$$

A comparison between the numerical, analytical and experimental results is shown in table 5.9.

Magnetic field measurement (Gauss)	**Measurement Position (mm)**			
	0	3.5	7	10.5
Magnetic Camera	16.77	16.89	15.44	2.19
FEM	16.60	16.93	16.47	2.41
TREE	16.61	16.95	16.50	2.49

Table 5.9 Experimental and modelling results

The experimentally measured magnetic field from the magnetic camera has been compared with an FEM simulation and the analytical ETREE model and gave good results.

5.8 Chapter Summary

This chapter introduces experimental techniques of eddy current defect detection, specifically magnetic field measurements. Discussions are included on the experimental study setup, specifically probe design and the operation of magnetic field sensors

The first experimental study compared experimental magnetic field measurements made using a Hall sensor with a numerical FEM simulation model. This work has investigated the magnetic field change due to the disruption of eddy currents around a surface and subsurface defect (area of zero conductivity). The comparative results of experimental studies and simulation models at different scan directions over the defects have been discussed.

The second experimental study extends the results from a single line scan to a scan over the area of a defect. This case is useful for defects having complex shapes. As well as the area scan, the use of directional (rectangular) coils in eddy current probes and the use of complex (real and imaginary) magnetic field measurements for defect mapping has been discussed. Measuring the real and imaginary components of the magnetic field is in contrast to the traditional impedance plane method, which measures the resistance (real component), and reactance (imaginary component) of the impedance. The theory behind complex measurements in eddy current testing is described using the transformer model.

The response for both a circular and rectangular eddy current probe have been compared. Investigating the slope of the magnetic field change due to the defect, the following has been observed.

1. The slope of the imaginary component of the magnetic field response is steeper than the real component.

2. The slope of the magnetic field response is steeper when using a rectangular coil than using a circular coil.

3. The slope of the magnetic field increases with increasing frequency (due to skin depth concentrating the field on the edge of the crack).

When looking at the surface scan of the magnetic field response, the shape of the defect is more closely related to the measurements with the steepest slope.

The use of sensor arrays for the visualisation of magnetic field distribution has been investigated. This allows the measurement of the spatial variation in magnetic field as opposed to a measurement at a single point. This has been applied to measuring the magnetic field developed by an eddy current probe (coil). The experimental measurements have been verified using modelling methods and found to be in good agreement.

Chapter 6 Defect Profile Reconstruction using PEC Measurements

6.1 Chapter Introduction

In this chapter, methods to reconstruct the profile of defects based on simulated measurements (FEM modelling) will be discussed, where a function will be established to map features of the PEC response to the profile (height and width) of the defect. The characterisation of the shape and geometrical dimensions of the defects are a key part of quantitative NDE and lifetime prediction [118].

A recent development in eddy current NDE, is the emergence of PEC techniques. This, in contrast to the conventional eddy current techniques mentioned in the previous chapters that use a single frequency sinusoidal excitation, uses a pulsed excitation. The pulsed excitation is comprised of a spectrum of frequencies, which allows simultaneous inspection to different depths of the sample. In addition, here the transient magnetic field response is measured, where time-of-flight measurements can be made to investigate different penetration depths [24], or frequency measurement through the spectrum analysis of the pulse [119]. PEC has also been used for defect detection in various applications, such as aircraft lap-joints [82].

6.2 Defect Profile Reconstruction

Current work on defect reconstruction uses inverse modelling where the reconstruction is performed using iterative machine learning methods such as neural networks [120] and or genetic algorithms [121]. In the work, an alternative to inverse modelling is presented, where a relationship vector is developed to map the PEC response to the defect profile.

Two different models based on features of the transient response will be used for defect reconstruction.

1. Frequency spectrum measurement.

2. Transient measurement.

The defect profile reconstruction will be performed by establishing a relationship as shown in equation (6.1).

$$\mathbf{P} = \mathbf{C} \cdot \mathbf{R} \qquad \textbf{(6.1)}$$

Where $\mathbf{P}$ is the defect profile, $\mathbf{C}$ is the frequency components or transient response and $\mathbf{R}$ is the relationship vector between the defect profile and the response. The PEC measurements are acquired from a numerical (FEM) simulation, the schematic of which are shown in figure 4.2.

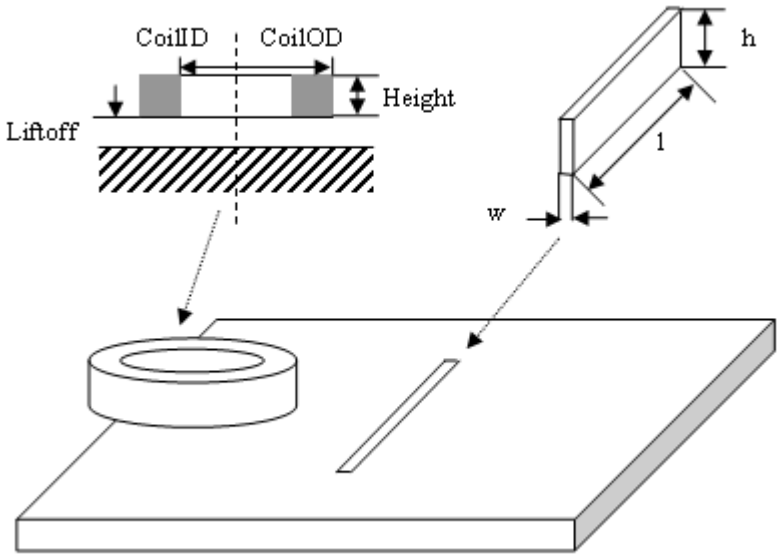

Figure 6.1 PEC defect reconstruction schematic layout

Details of the model setup are shown in table 4.2.

Scan	
Scan Step Size (mm)	0.5
Specimen	
Specimen Size (mm)	40×40×20
Specimen Conductivity (MS/m)	30
Defect Length (mm)	30
Probe	
Excitation Current (mA)	60
Coil ID (mm)	9.65
Coil OD (mm)	14.02
Coil Height (mm)	3
Coil Turns	123

Table 6.1 PEC defect reconstruction model setup

The defect width and height are varied, depending upon defect profile. The pulse excitation is a damped square wave, $\left[1-\exp\left(-time/\tau\right)\right]$, where τ is the coil time constant $\left(\approx 8\times10^{-5}\ \text{sec}\right)$.

In the PEC response, B_{REF} is the reference signal obtained on a non-defect area; B is the total signal. To reconstruct the defect profile, the differential signal $\left(\Delta B\right)$ is used as shown in equation (6.2).

$$\Delta B = B - B_{REF} \qquad \textbf{(6.2)}$$

6.2.1 Defect profile reconstruction based on spectrum measurements

In case of single frequency excitation, the depth of eddy current penetration is determined by skin depth. In other words, different depths can be investigated with different excitation frequencies. As the pulse waveform contains a wide range of excitation frequencies, it will cover a broad range of penetration depths.

The model for defect profile reconstruction using spectrum measurement follows the functional steps.

1. Setup

A defect with a known profile is used to establish a relationship, $\mathbf{R}$, between the spectrum components, $\mathbf{F}$, of the PEC response, ΔB, and the defect profile, $\mathbf{P}$. The defect profile, $\mathbf{P}$, is given by equation (6.3).

$$\mathbf{P} = \begin{bmatrix} p_1(z) & p_2(z) & p_3(z) & \cdots & p_M(z) \end{bmatrix} \tag{6.3}$$

Where $p_m(z)$ is the defect profile function (in the *z*-direction) at the m^{th} scanning position. This is shown in figure 6.2.

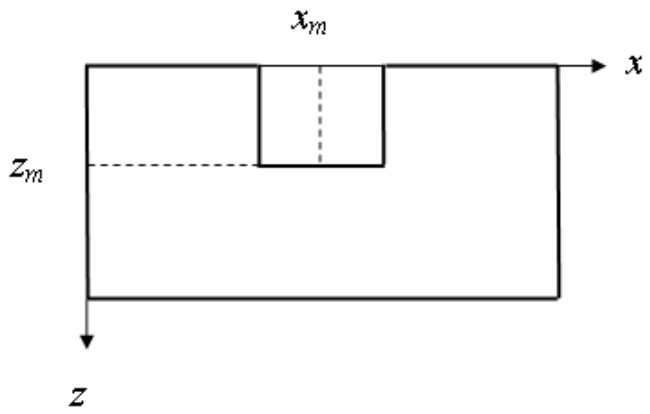

Figure 6.2 Profile representation of slot

The frequency spectrum components matrix $\mathbf{F}$, is given by equation (6.4).

$$\mathbf{F} = \begin{bmatrix} f(p_1 s_1) & f(p_1 s_2) & f(p_1 s_3) \ldots & f(p_1 s_N) \\ f(p_2 s_1) & f(p_2 s_2) & f(p_2 s_3) \ldots & f(p_2 s_n) \\ f(p_3 s_1) & f(p_3 s_2) & f(p_3 s_3) \ldots & f(p_3 s_N) \\ \vdots & \vdots & \vdots \ddots & \vdots \\ f(p_M s_1) & f(p_M s_2) & f(p_M s_3) \ldots & f(p_M s_N) \end{bmatrix} \tag{6.4}$$

Where $f(p_m s_n)$ is the n^{th} spectrum component of the PEC response at scanning position *m*, *M* is the total number of scanning positions, and *N* is the highest order of frequency

component used for defect reconstruction. To create this matrix from the PEC transient response, it is converted to the frequency domain using the Fast Fourier Transform (MATLAB function *fft*).

The relationship vector, $\mathbf{R}$, is given by equation (6.5).

$$\mathbf{R} = \begin{bmatrix} r(s_1) & r(s_2) & r(s_3) & \cdots & r(s_N) \end{bmatrix} \quad \textbf{(6.5)}$$

The term $r(s_n)$ is the relationship function between the n^{th} harmonic frequency and the defect profile.

2. Training

A known defect profile with a known PEC response is used to build the initial relationship vector, $\mathbf{R}$. The FEM simulation, shown in figure 4.2 and table 4.2, is used to model the eddy current probe being scanned across the defect and the PEC response is measured. As both $\mathbf{F}$ and $\mathbf{P}$ are now known we can calculate the relationship vector $\mathbf{R}$. This is calculated as follows.

```
for j = start frequency harmonic to end frequency harmonic
(N)
     for k = start position to end position (M)
          F(j,k) = fft(PEC response(k,j))
     end
end
R = P / F
```

3. Reconstruction

Now we have the relationship vector $\mathbf{R}$, we can reconstruct the unknown defect profile for a given PEC response, using the amplitude of the frequency components of the PEC differential response, ΔB.

```
Profile Reconstruction = R × Reconstruction PEC Response
```

To test the profile reconstruction procedure, the following scenarios are considered.

1. Training Slot	3mm x 5mm
2. Reconstructed Slots	2mm x 3mm
	2mm x 5mm

The reconstruction of the slots is shown in figure 6.3 and figure 6.4.

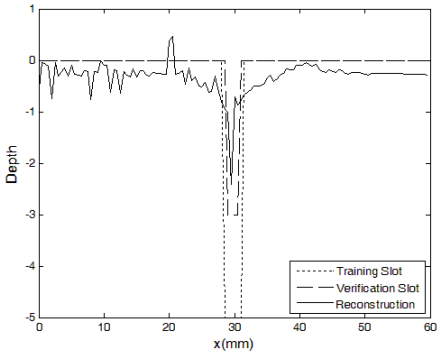

Figure 6.3 Profile reconstruction from frequency measurement of 2mm x 3mm slot

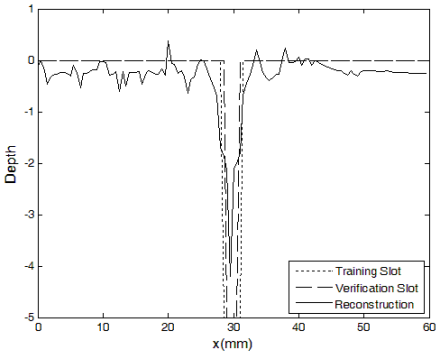

Figure 6.4 Profile reconstruction from frequency measurement of 2mm x 5mm slot

The reconstruction error is calculated using the mean squared error (MSE) between the verification slot (crack profile to find) and reconstructed slot, as shown in equation (6.6).

$$MSE = \frac{1}{n}\sum_{i=1}^{n}\left(\text{reconstruction} - \text{crack shape}\right)^2 \qquad \textbf{(6.6)}$$

The MSE for the profile reconstructions shown in figure 6.3 and figure 6.4 are shown in table 6.2.

Verification slot	MSE
2mm x 3mm	0.2355
2mm x 5mm	0.3663

Table 6.2 PEC spectrum reconstruction error

To investigate the effect of using the complex components (the real and imaginary values) of the frequency spectrum as opposed to the amplitude used in this example, the reconstruction MSE for a 2mm x 3mm slot is calculated for each component, the results of which are shown in table 6.3. This shows that using the amplitude of the frequency components gives the most accurate reconstruction in this case.

Verification slot	MSE (Amplitude)	MSE (Real)	MSE (Imag)
2mm x 3mm	0.2355	1.2774	0.3862

Table 6.3 PEC spectrum reconstruction error comparison

To investigate the effect of changing the number of frequency components (harmonics in the reconstruction), the reconstruction MSE, shown in equation (6.6), for a 2mm x 3mm slot is calculated for each harmonic, the results of which are shown in figure 6.5.

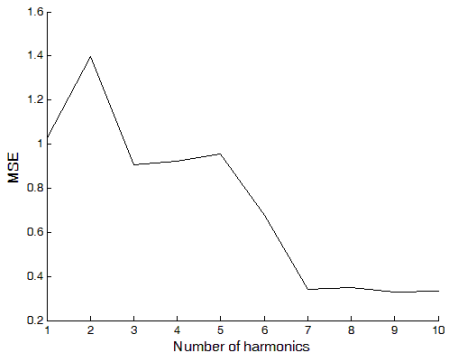

Figure 6.5 MSE of profile reconstruction with spectrum components

This shows that using seven harmonics gives the most accurate reconstruction in this case.

6.2.2 Defect profile reconstruction based on transient measurements

In a similar manner to frequency measurements, Panaitov *et al.* [122] demonstrated that the penetration depth of the PEC signal corresponds to the time in the transient response, which can be calculated as shown in equation (6.7).

$$\delta = \sqrt{\frac{t}{\pi\mu\sigma}} \tag{6.7}$$

Where t is the time. The response over time contains different depth information of the specimen under test. As with the spectrum response, the differential signal, ΔB, as shown in equation (6.2), is used to reconstruct the defect profile. The model for defect profile reconstruction using transient measurement follows the functional steps.

1. Setup

A defect with a known profile is used to establish a relationship, $\mathbf{R}$, between the transient response, $\mathbf{T}$ of the PEC response, ΔB, and the defect profile, $\mathbf{P}$. The defect profile $\mathbf{P}$, is given in the frequency domain section, by equation (6.3) and figure 6.2. The transient components matrix, $\mathbf{T}$, is shown in equation (6.8).

$$\mathbf{T} = \begin{bmatrix} t(p_1 s_1) & t(p_1 s_2) & t(p_1 s_3) \ldots & t(p_1 s_N) \\ t(p_2 s_1) & t(p_2 s_2) & t(p_2 s_3) \ldots & t(p_2 s_n) \\ t(p_3 s_1) & t(p_3 s_2) & t(p_3 s_3) \ldots & t(p_3 s_N) \\ \vdots & \vdots & \vdots \ddots & \vdots \\ t(p_M s_1) & t(p_M s_2) & t(p_M s_3) \ldots & t(p_M s_N) \end{bmatrix} \tag{6.8}$$

Where $t(p_m s_n)$ is the n^{th} time point in the differential response, $\Delta B_m(t)$, at scanning position m, M is the total number of scanning positions, and N is the end of the response. This is shown in figure 6.6, where $t_1 \ldots t_9$ are the points in the response used for reconstruction.

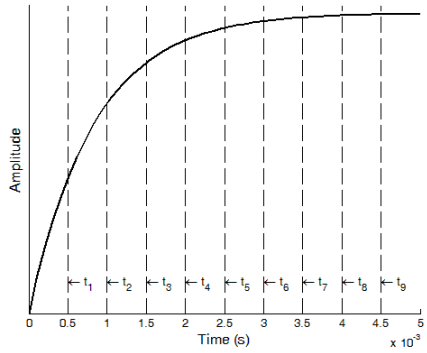

Figure 6.6 Transient points in PEC response for reconstruction

The relationship vector $\mathbf{R}$, is given by equation (6.9).

$$\mathbf{R} = \begin{bmatrix} r(s_1) & r(s_2) & r(s_3) & \cdots & r(s_N) \end{bmatrix} \quad \textbf{(6.9)}$$

The term $r(s_n)$ is the relationship function between the n^{th} time point and the defect profile.

2. Training

A known defect profile with a known PEC response is used to build the initial relationship vector, $\mathbf{R}$. Again, the FEM simulation shown in figure 4.2 and table 4.2, is used to model the eddy current probe being scanned across the defect and the PEC response is measured. As both $\mathbf{T}$ and $\mathbf{P}$ are now known we can calculate the relationship vector, $\mathbf{R}$, for the probe being scanned over this material. This is calculated as follows.

```
for j = start time to end time (N)
     for k = start position to end position (M)
          T(j,k) = PEC response(k,j))
     end
end
R = P / T
```

3. Reconstruction

Now we have the relationship vector, $\mathbf{R}$, we can now construct an unknown defect profile for a given PEC response.

$$\text{Profile Reconstruction} = \mathbf{R} \times \text{Reconstruction PEC Response}$$

The following scenarios are considered.

1. Training Slot	3mm x 5mm
2. Reconstructed Slots	2mm x 3mm
	2mm x 5mm

The reconstruction of the slots is shown in figure 6.7 and figure 6.8.

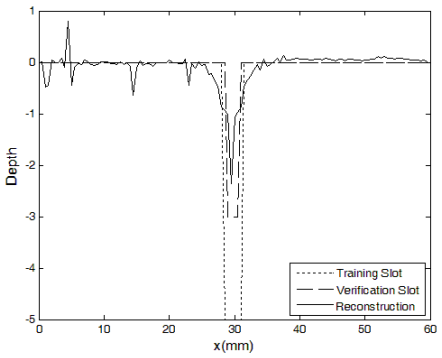

Figure 6.7 Profile reconstruction from transient measurement of 2mm x 3mm slot

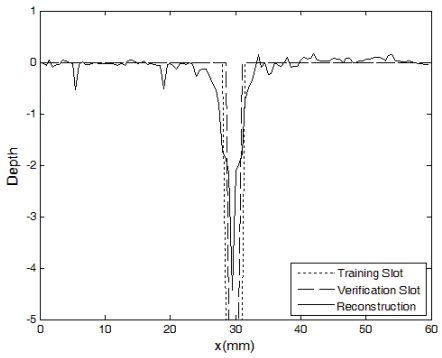

Figure 6.8 Profile reconstruction from transient measurement of 2mm x 5mm slot

As with the frequency reconstruction, the reconstruction error is calculated using the mean squared error (MSE) between the verification slot (to find) and reconstructed slot as shown in equation (6.6). The MSE for the reconstruction shown in figure 6.7 and figure 6.8 is shown in table 6.4.

Verification slot	MSE
2mm x 3mm	0.1478
2mm x 5mm	0.3237

Table 6.4 PEC transient reconstruction error

6.3 Chapter Summary

This chapter has given two linear reconstruction models based on spectrum components and time points of the PEC response, ΔB, when a probe is scanned over a defect. The model was trained by scanning over a "known" defect, then validated using the response from scanning other defects, both using an FEM simulation model. In summary, both the reconstruction using transient and spectrum components reconstruct the slot profile (slot and width) accurately as shown in figure 6.9 and figure 6.10.

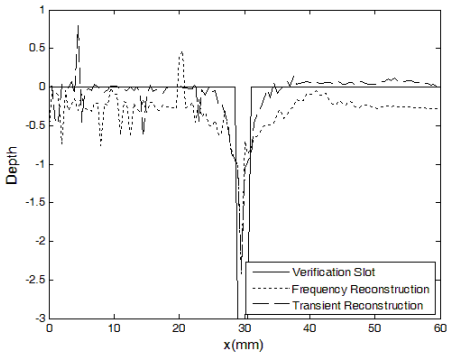

Figure 6.9 Profile reconstruction comparison using transient and frequency measurements of 2mm x 3mm slot

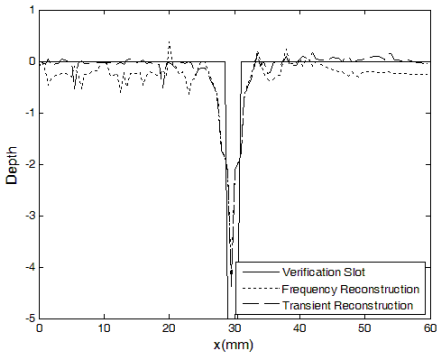

Figure 6.10 Profile reconstruction comparison using transient and frequency measurements of 2mm x 5mm slot

A drawback of this approach is that the data used to train the function, and create the mapping, must be similar to the actual data or the mapping will fail as the relationship vector is a linear relationship.

Chapter 7 Conclusions and Future Work

7.1 Chapter Introduction

In this chapter, the research work presented in previous chapters will be summarised. The contribution of the work to research in eddy current NDE will be highlighted. Based on the research outcome, options for further work will be addressed.

7.2 Discussion of Research

This thesis focuses on the theoretical and experimental investigation of eddy current inspection techniques, specifically investigating the magnetic field response to the presence of defects. The following work has been presented.

(1) A literature survey on eddy current NDE and an overview of analytical and numerical modelling methods for eddy current NDE problems;

(2) Discussion of analytical modelling methods based on integral or series expressions and numerical modelling using both 2D and 3D Finite Element Method (FEM) models;

(3) Numerical simulation of the magnetic field response to defects;

(4) Experimental investigation of the magnetic field response to defects;

(5) Defect reconstruction using eddy current measurements;

7.2.1 Numerical simulation of eddy current NDE

Numerical simulation results are useful in predicting the response of magnetic field measurements in eddy current inspection and defect detection. This has included the simulation of a probe being moved over a defect and simulating the acquired magnetic field change due to the defect. This provides an understanding of the underlying phenomena of how the eddy currents induced in the specimen are diverted due to the

defect and the resulting change in magnetic field. Numerical FEM simulations have been found to be versatile in solving the forward models discussed in this thesis, for both sinusoidal excitation (in the experimental study) and transient excitation (for defect reconstruction).

7.2.2 Analytical modelling of eddy current NDE

Analytical models are useful in the solution of eddy current problems with simple (canonical) geometries. The analytical model is an order of magnitude faster to solve than the numerical (FEM) model. These types of models have progressed from integral methods to a faster truncated method, which allows the calculation of magnetic field in a variety of eddy current inspection scenarios.

7.2.3 Experimental investigation of magnetic field response to defects

Experimental work has been performed to measure the magnetic field response to simulated defects in conductive specimens. This work consisted of two parts.

1. The amplitude of magnetic field change due to surface and subsurface defects was measured.

   In this work, a numerical (FEM) model was developed to predict the change in magnetic field as an eddy current probe was scanned in parallel or perpendicular to the orientation of surface and subsurface defects. These results were then compared to experimental measurements of a probe being scanned over an EDM slot. There was good agreement between the two sets of measurements, verified by measuring the correlation coefficient between the sets of results. This showed that the magnetic field measurement was a useful indicator for the presence of defects, including when subsurface defects are examined.

   Further FEM simulations also show that the measurements could be used to quantify the defect geometry based on the shape of the magnetic field response.

2. Complex magnetic field measurements for defect quantification.

   In this work, an experimental study was performed to investigate the effect of complex magnetic field measurements and the use of directional coils for defect quantification.

It was found that the directional coil produced an output, which corresponded more with the shape of the defect than the circular probe. This is because the rectangular probe generates eddy current along the direction of the defect giving a greater concentration along the edge of the defect.

A further comparison was performed to investigate the use of the complex components of the magnetic field measurements (real, $\Re e(B_z)$, and imaginary, $\Im m(B_z)$, components). The imaginary component, $\Im m(B_z)$, had a greater correlation with the shape of the defect than using other measurements.

7.2.4 Defect reconstruction using pulsed eddy current measurements

In this work, both the frequency and transient components from a PEC measurement are used for defect profile reconstruction. The frequency spectrum response uses measurements from different frequency harmonics of the differential pulse response to reconstruct the defect shape. The transient response uses measurements from different points in time of the differential pulse response to reconstruct the defect shape. FEM simulations of a probe being scanned across a slot type defect have been performed to acquire the PEC response. The profile of an unknown shaped slot has been reconstructed using both methods. The use of the forward model to map between the measurement and defect profile is more efficient than standard inverse modelling approaches as the iterative solution of forward models are not required.

7.3 Research Contribution

The contributions of the research are as follows.

1. Investigation of the magnetic field response to defects through experimental work and numerical modelling.

   This method provides a useful indication of the presence of both surface and subsurface defects. For improved defect evaluation, the use of complex (real and imaginary) magnetic field measurements with a combination of circular and rectangular probes has also been investigated. The imaginary component of the magnetic field has a faster rate of change (steeper slope) when compared to the real component when scanned over a defect, providing an improved correlation with the

shape of the defect. It has the potential for modelling and simulation of complex geometrical shaped defects;

2. Defect reconstruction using PEC measurements.

   The profiles of a slot defect (width and height) are reconstructed using frequency components and transient responses from PEC measurements.

7.4 Future Work

Based on the current research work in analytical and numerical modelling and experimental study, further study includes evaluation of various types of specimens found in industrial applications (stress corrosion cracks and composite materials), as well as novel inspection methods such as PEC thermography, for improved defect detection capability.

7.4.1 3D eddy current measurements for complex geometry defects

The use of 3D eddy current measurements, measuring B_x, B_y and B_z, is useful for the inspection of complex geometrical shaped defects (such as stress corrosion cracks, thermal and rolling fatigue damage) [83, 123].

7.4.2 Modelling of complex problems

Solving problems such as PEC thermography, which deals with electromagnetics and heat transfer, requires heavy computational requirements when using numerical models. Analytical models will be investigated for the solutions to these types of problems.

7.4.3 Analytical models for magnetic field response to defects

Recent work has been performed [45] to predict the impedance change due to a defect, where the TREE method has been used in conjunction with the Boundary Element Method. This could be extended to use the magnetic field from the dipole, rather than the electric field from the dipole, to predict the magnetic field response to defects.

7.4.4 The use of sensor arrays for defect detection

The magnetic camera sensor array has been used for magnetic field visualisation [114] and lift-off calculations [124]. As sensor arrays allow for the simultaneous measurement of the spatial variation in magnetic field over an area, this will lead to improved QNDE of defects, as an "image" of the defect can be produced from a single measurement, which is quicker than traditional scanning methods.

7.5 Chapter Summary

This chapter have given a summary of the research results in this thesis, with contributions made and possible suggestions for future work.

Bibliography

[1] J. C. Maxwell, *A Treatise on Electricity and Magnetism*. London: Clarendon Press, 1873.

[2] C. V. Dodd and W. E. Deeds, "Analytical Solutions to Eddy-Current Probe-Coil Problems," *Journal of Applied Physics,* vol. 39, pp. 2829-2838, 1968.

[3] T. Theodoulidis and E. Kriezis, "Series expansions in eddy current nondestructive evaluation models," *Journal of Materials Processing Technology,* vol. 161, pp. 343-347, 2005.

[4] T. P. Theodoulidis and E. E. Kriezis, *Eddy Current Canonical Problems (with Applications to Nondestructive Evaluation)*. Forsyth, GA: Tech Science Press, 2006.

[5] R. Clark, "Rail flaw detection: overview and needs for future developments," *NDT&E International,* vol. 37, pp. 111-118, 2004.

[6] T. Dogaru, S. T. Smith, C. H. Smith, and R. W. Schneider, "Eddy Current Inspection for Deep Crack Detection around Fastener Holes in Airplane Multi-Layered Structures," in *111 Pan-American Conference for Nondestructive Testing* Rio de Janeiro, Brazil, 2003.

[7] M. M. U. Khanz, "Detection of defect on Aircraft Multi-layered Structure by Eddy Current technique," in *15th World Conference on Non-Destructive Testing* Rome, Italy, 2000.

[8] O. Postolache, M. D. Pereira, H. G. Ramos, and A. L. Ribeiro, "NDT on Aluminum Aircraft Plates based on Eddy Current Sensing and Image Processing," in *Instrumentation and Measurement Technology Conference* Victoria, BC: IEEE, 2008.

[9] J. B. Nestleroth and R. J. Davis, "Application of eddy currents induced by permanent magnets for pipeline inspection," *NDT & E International,* vol. 40, pp. 77-84, 2007.

[10] J. Hwang, J. Lee, J. Jun, R. Wang, S. Choi, and S. Hong, "Scan Type Magnetic Camera Images with a High Spatial Resolution for NDT Obtained By Using a Linearly Integrated Hall Sensors Array," in *IEEE International Workshop on Imaging Systems and Techniques - IST 2007* Krakow, Poland, 2007.

[11] J. Jun, J. Hwang, and J. Lee, "Quantitative Nondestructive Evaluation of the Crack on the Austenite Stainless Steel Using the Induced Eddy Current and the Hall Sensor Array," in *Instrumentation and Measurement Technology Conference Proceedings, 2007 IEEE*, 2007, pp. 1-6.

[12] A. Oota, T. Ito, K. Kawano, D. Sugiyama, and H. Aoki, "Magnetic detection of cracks by fatigue in mild steels using a scanning Hall-sensor microscope," *Review of Scientific Instruments,* vol. 70, pp. 184-186, 1999.

[13] C. Schott, R. S. Popovic, S. Alberti, and M. Q. Tran, "High accuracy magnetic field measurements with a Hall probe," *Review of Scientific Instruments,* vol. 70, pp. 2703-2707, 1999.

[14] H. Sun, R. Ali, M. Johnson, and J. R. Bowler, "Enhanced Flaw Detection using an Eddy Current Probe with a Linear Array of Hall Sensors," in *Review of Quantitative Nondestructive Evaluation*, D. O. Thompson and D. E. Chimenti, Eds.: American Institute of Physics, 2005.

[15] G. Y. Tian, A. Sophian, D. Taylor, and J. Rudlin, "Multiple sensors on pulsed eddy-current detection for 3-D subsurface crack assessment," *IEEE Sensors Journal,* vol. 5, pp. 90-96, 2005.

[16] T. Dogaru and S. T. Smith, "Giant Magnetoresistance-Based Eddy-Current Sensor," *IEEE Transactions on Magnetics,* vol. 37, pp. 3831-3838, 2001.

[17] R. Hamia, C. Cordier, S. Saez, and C. Dolabdjian, "Eddy-Current Nondestructive Testing Using an Improved GMR Magnetometer and a Single Wire as Inducer: A FEM Performance Analysis," *IEEE Transactions on Magnetics,* vol. 46, pp. 3731-3737, 2010.

[18] J.-T. Jeng, G.-S. Lee, W.-C. Liao, and C.-L. Shu, "Depth-resolved eddy-current detection with GMR magnetometer," *Journal of Magnetism and Magnetic Materials,* vol. 304, pp. e470-e473, 2006.

[19] A. V. Nazarov, F. C. S. da Silva, and D. P. Pappas, "Arrays of magnetoresistive sensors for nondestructive testing," *Journal of Vacuum Science Technology A: Vacuum, Surfaces, and Films,* vol. 22, pp. 1375-1378, 2006.

[20] J. D. Achenbach, "Quantitative nondestructive evaluation," *International Journal of Solids and Structures,* vol. 37, pp. 13-27, 2000.

[21] B. A. Auld and J. C. Moulder, "Review of Advances in Quantitative Eddy Current Nondestructive Evaluation," *Journal of Nondestructive Evaluation,* vol. 18, pp. 3-36, 1999.

[22] Y. A. Plotnikov, S. C. Nath, and C. W. Rose, "Defect characterization in multi-layered conductive components with pulsed eddy current," in *Quantitative Nondestructive Evaluation*. vol. 615 Brunswick, Maine: American Institute of Physics, 2002, pp. 1976-1983.

[23] C. H. Smith, R. W. Schneider, T. Dogaru, and S. T. Smith, "Eddy-Current Testing with GMR Magnetic Sensor Arrays," in *Quantitative Nondestructive Evaluation Conference*. vol. 2323, D. O. Thompson and D. E. Chimenti, Eds. Green Bay, WI: American Institute of Physics, 2003, pp. 406-413.

[24] R. A. Smith and D. J. Harrison, "Hall sensor arrays for rapid large-area transient eddy current inspection," *Insight - Non-Destructive Testing and Condition Monitoring,* vol. 46, pp. 142-146, 2004.

[25] P. Huang, Z. Zhou, and Z. Wu, "Quantifying hidden defect in multi-layered structures by using eddy current system combined with a scanner," *Journal of Physics: Conference Series,* vol. 13, pp. 385-388, 2005.

[26] S. Tumanski and A. Liszka, "The methods and devices for scanning of magnetic fields," *Journal of Magnetism and Magnetic Materials,* vol. 242-245, pp. 1253-1256, 2002.

[27] T. P. Theodoulidis and J. R. Bowler, "Eddy current coil interaction with a right-angled conductive wedge," *Proceedings of the Royal Society A: Mathematical, Physical and Engineering Sciences,* vol. 461, pp. 3123-3139, 2005.

[28] J. R. Bowler and T. P. Theodoulidis, "Coil impedance variation due to induced current at the edge of a conductive plate," *Journal of Physics D: Applied Physics,* vol. 39, pp. 2862-2868, 2006.

[29] S. K. Burke, J. R. Bowler, and T. P. Theodoulidis, "An Experimental and Theoretical Study of Eddy-Current End Effects In Finite Rods and Finite Length Holes," in *American Institute of Physics*, 2006, pp. 361-368.

[30] Y. Li, T. Theodoulidis, and G. Y. Tian, "Magnetic Field-Based Eddy-Current Modeling for Multilayered Specimens," *IEEE Transactions on Magnetics,* vol. 43, pp. 4010-4015, 2007.

[31] M. L. Burrows, "A Theory of Eddy-Current Flaw Detection." vol. PhD: University of Michigan, 1964.

[32] A. P. Raiche and J. H. Coggon, "Analytic Green's Tensors for Integral Equation Modelling," *Geophysical Journal of the Royal Astronomical Society,* vol. 42, pp. 1035-1038, 1975.

[33] A. P. Raiche, "An integral equation approach to three-dimensional modelling," *Geophysical Journal of the Royal Astronomical Society,* vol. 36, pp. 363-376, 1974.

[34] W. S. Dunbar, "The Volume Integral Method of Eddy Current Modeling," *Journal of Nondestructive Evaluation,* vol. 5, pp. 9-14, 1985.

[35] W. S. Dunbar, "The Volume Integral Method of Eddy-Current Modeling: Verification," *Journal of Nondestructive Evaluation,* vol. 7, pp. 43-54, 1988.

[36] D. McA McKirdy, "Recent improvements to the application of the volume integral method of eddy current modeling," *Journal of Nondestructive Evaluation,* vol. 8, pp. 45-52, 1989.

[37] J. R. Bowler, L. D. Sabbagh, and H. A. Sabbagh, "A Theoretical and Computational Model of Eddy-Current Probes Incorporating Volume Integral and Conjugate Gradient Methods," *IEEE Transactions on Magnetics,* vol. 25, pp. 2650-2664, 1989.

[38] J. R. Bowler, "Eddy-current interaction with an ideal crack. I. The forward problem," *Journal of Applied Physics,* vol. 75, pp. 8128–8137, 1994.

[39] J. R. Bowler, S. J. Norton, and D. J. Harrison, "Eddy current interaction with an ideal crack, Part II: The inverse problem," *Journal of Applied Physics,* vol. 75, pp. 8138-8144, 1994.

[40] C. Dezhi, K. R. Shao, S. Jianni, and Y. Weili, "Eddy Current Interaction with a Thin-Opening Crack in a Plate Conductor," *IEEE Transactions on Magnetics,* vol. 36, pp. 1745-1749, 2000.

[41] N. Harfield and J. R. Bowler, "Theory of thin-skin eddy-current interaction with surface cracks," *Journal of Applied Physics,* vol. 82, pp. 4590-4603, 1997.

[42] J. R. Bowler and N. Harfield, "Evaluation of Probe Impedance Due to Thin-Skin Eddy-Current Interaction with Surface Cracks," *IEEE Transactions on Magnetics,* vol. 34, pp. 515-523, 1998.

[43] J. R. Bowler and N. Harfield, "Thin-Skin Eddy-Current Interaction with Semielliptical and Epicyclic Cracks," *IEEE Transactions on Magnetics,* vol. 36, pp. 281-291, 2000.

[44] J. R. Bowler, "Thin-skin eddy-current inversion for the determination of crack shapes," *Inverse Problems,* vol. 18, pp. 1891-1905, 2002.

[45] T. Theodoulidis, N. Poulakis, and A. Dragogias, "Rapid computation of eddy current signals from narrow cracks " *NDT&E International,* vol. 43, pp. 13-19, 2010.

[46] T. Theodoulidis, "Developments in efficiently modelling eddy current testing of narrow cracks," *NDT&E International,* vol. 43, pp. 591-598, 2010.

[47] L. Xing, "Rapid calculation of eddy current field Green's function using matrix pencil method," *NDT&E International,* vol. 42, pp. 85-91, 2009.

[48] T. Kincaid and M. Chari, "The application of finite element method analysis to eddy current nondestructive evaluation," *IEEE Transactions on Magnetics,* vol. 15, pp. 1956-1960, 1979.

[49] J. Jin, *The Finite Element Method in Electromagnetics*. New York: John Wiley & Sons Inc., 2002.

[50] A. C. Polycarpou, "Introduction to the Finite Element Method in Electromagnetics," Morgan & Claypool Publishers, 2006.

[51] R. Palanisamy and W. Lord, "Finite element analysis of eddy current phenomena," *Material Evaluation,* vol. 38, pp. 39-43, 1980.

[52] N. Ida, "Three Dimensional Finite Element Modeling of Electromagnetic Nondestructive Testing Phenomena." vol. PhD Colorado: Colorado State University, 1983.

[53] Z. Chen, K. Aoto, and K. Miya, "Reconstruction of cracks with physical closure from signals of eddy current testing," *IEEE Transactions on Magnetics,* vol. 36, pp. 1018-1022, 2000.

[54] W. Cheng, K. Miya, and Z. Chen, "Reconstruction of Cracks with Multiple Eddy Current Coils Using a Database Approach," *Journal of Nondestructive Evaluation,* vol. 18, pp. 149-160, 1999.

[55] V. Monebhurrun, B. Duchne, and D. Lesselier, "Three-dimensional inversion of eddy current data for non-destructive evaluation of steam generator tubes," *Inverse Problems,* vol. 14, pp. 707-724, ///1998 1998.

[56] S. J. Norton and J. R. Bowler, "Theory of eddy current inversion," *Journal of Applied Physics,* vol. 73, pp. 501-512, 1993.

[57] H. Sabbagh and L. Sabbagh, "An eddy-current model for three-dimensional inversion," *IEEE Transactions on Magnetics,* vol. 22, pp. 282-291, 1986.

[58] B. Ye, G. Zhang, P. Huang, M. Fan, S. Zheng, and Z. Zhou, "Quantifying Geometry Parameters of Defect in Multi-layered Structures from Eddy Current Nondestructive Evaluation Signals by Using Genetic Algorithm," in *The Sixth World Congress on Intelligent Control and Automation, 2006. WCICA 2006.* vol. 2, 2006, pp. 5358-5362.

[59] T. Chady, M. Enokizono, and R. Sikora, "Neural network models of eddy current multi-frequency system for nondestructive testing," *IEEE Transactions on Magnetics,* vol. 36, pp. 1724-1727, 2000.

[60] M. Ravan, S. H. H. Sadeghi, and R. Moini, "Using a wavelet network for reconstruction of fatigue crack depth profile from AC field measurement signals," *NDT & E International,* vol. 40, pp. 537-544, 2007/10 2007.

[61] R. Sikora, T. Chady, S. Gratkowski, and M. Komorowski, "Identification of flaws using eddy current testing," *COMPEL : The International Journal for Computation and Mathematics in Electrical and Electronic Engineering,* vol. 17, pp. 516-527, ///22 July 1998 1998.

[62] M. Wrzuszczak and J. Wrzuszczak, "Eddy current flaw detection with neural network applications," *Measurement,* vol. 38, pp. 132-136, 2005/9 2005.

[63] Y. Li, G. Y. Tian, and A. Simm, "Fast analytical modelling for pulsed eddy current evaluation," *NDT&E International,* vol. 41, pp. 477-483, 2008.

[64] J.-S. Hwang and J. Lee, "A Study of Nondestructive Evaluation Using Scan type Magnetic Camera," in *ICCAS2005* Gyeonggi-Do, Korea, 2005.

[65] I. M. Z. Abidin, "Modelling and experimental investigation of eddy current distribution for angular defect characterisation," in *Electrical, Electronic and Computer Engineering*. vol. PhD Newcastle upon Tyne: Newcasltle Univeristy, 2010.

[66] S. S. Udpa and P. O. Moore, "Nondestructive Testing Handbook," 3rd ed. vol. 5: Electromagnetic Testing: American Society for Nondestructive Testing, Inc., 2004.

[67] D. J. Hagemaier, *Fundamentals of eddy current testing*. Columbus, OH: The American Society for Nondestructive Testing, Inc., 1990.

[68] D. Minkov, Y. Takeda, T. Shoji, and J. Lee, "Estimating the sizes of surface cracks based on Hall element measurements of the leakage magnetic field and a dipole model of a crack," *Applied Physics A: Materials Science & Processing,* vol. 74, pp. 169-176, 2002.

[69] C. Christides, I. Panagiotopoulos, D. Niarchos, and G. Jones, "Fast magnetic field mapping of permanent magnets with GMR bridge and Hall-probe sensors," *Sensors and Actuators A,* vol. 106, pp. 243-245, 2003.

[70] Y. Hatsukade, A. Kosugi, K. Mori, and S. Tanaka, "Detection of micro-flaws on thin copper tubes using SQUID-NDI system based on eddy current technique," *Physica C,* vol. 2005, pp. 426-431, 2005.

[71] M. v. Kreutzbruck, K. Allweins, T. Ruhl, M. Muck, C. Heiden, H.-J. Krause, and R. Hohmann, "Defect detection and classification using a SQUID based multiple frequency eddy current NDE system," *IEEE Transactions on Applied Superconductivity,* vol. 11, pp. 1032-1037, 2001.

[72] A. Ruosi, M. Valentino, G. Pepe, V. Monebhurrun, D. Lesselier, and B. Duchene, "High Tc SQUIDs and eddy-current NDE: a comprehensive investigation from real data to modelling," *Measurement Science and Technology,* vol. 11, pp. 1639-1648, 2000.

[73] J. T. Jeng, H. E. Horng, H. C. Yang, J. C. Chen, and J. H. Chen, "Simulation of the magnetic field due to defects and verification using high-Tc SQUID," *Physica C,* vol. 2002, pp. 298-302, 2002.

[74] M. Pattabiraman, R. Nagendrana, and M. P. Janawadkar, "Rapid flaw depth estimation from SQUID-based eddy current nondestructive evaluation " *NDT&E International,* vol. 40, pp. 289-293, 2007.

[75] N. Poulakis and T. Theodoulidis, "The use of a SQUID for quantitative magnetic field measurements in the nanoTesla region for eddy current NDE," in *Hellenic Society for NDT. 4th International Conference on NDT* Crete, 2007.

[76] D. McA McKirdy, S. Cochran, G. B. Donaldson, and A. McNab, "Theoretical Consideration of Fatigue Crack Detection and Characterisation using SQUID Sensors," in *International Workshop on Electromagnetic NDE (ENDE 95)* London, 1995.

[77] N. Kasai, Y. Hatsukade, and H. Takashima, "Non-Destructive Detection of Defects in Carbon Fiber-Reinforced Carbon Matrix Composites Using SQUID," *IEICE Transactions on Electronics,* vol. E88-C, 2005.

[78] J. M. Liu and S. N. Vernon, "A Multi-Frequency Eddy Current Testing Technique for Inhomogeneous Metallic Materials," *Nondestructive Testing and Evaluation,* vol. 2, pp. 141-153, 1986.

[79] G. Y. Tian and A. Sophian, "Study of magnetic sensors for pulsed eddy current techniques," *Insight - Non-Destructive Testing and Condition Monitoring,* vol. 47, pp. 277-279, 2005.

[80] G. Y. Tian and A. Sophian, "Pulsed Eddy Current Sensors," *Encyclopaedia of Sensors,* vol. 8, pp. 347-366, 30 April 2007 2006.

[81] H.-C. Yang and C.-C. Tai, "Pulsed eddy-current measurement of a conducting coating on a magnetic metal plate," *Measurement Science and Technology,* vol. 13, pp. 1259-1265, 2002.

[82] A. Sophian, G. Y. Tian, D. Taylor, and J. Rudlin, "Design of a pulsed eddy current sensor for detection of defects in aircraft lap-joints," *Sensors and Actuators A,* vol. 101, pp. 92-98, 2002.

[83] Y. Li, J. Wilson, and G. Y. Tian, "Experiment and simulation study of 3D magnetic field sensing for magnetic flux leakage defect characterisation," *NDT&E International,* vol. 40, pp. 179-184, 2007/3 2007.

[84] A. R. Ramirez, J. S. D. Mason, and N. Pearson, "Experimental study to differentiate between top and bottom defects for MFL tank floor inspections," *NDT & E International,* vol. 42, pp. 16-21, 2009.

[85] M. P. Papaelias, C. Roberts, and C. L. Davis, "A review on non-destructive evaluation of rails: state-of-the-art and future development," *Proceedings of the Institution of Mechanical Engineers, Part F: Journal of Rail and Rapid Transit,* vol. 222, pp. 367-384, 2008.

[86] L. Chen, P.-W. Que, and T. Jin, "A Giant-Magnetoresistance Sensor for Magnetic-Flux-Leakage Nondestructive Testing of a Pipeline," *Russian Journal of Nondestructive Testing,* vol. 41, pp. 462-465, 2005.

[87] X.-B. Li, X. Li, L. Chen, P.-F. Feng, H.-D. Wang, and Z.-Y. Huang, "Numerical simulation and experiments of magnetic flux leakage inspection in pipeline steel," *Journal of Mechanical Science and Technology,* vol. 23, pp. 109-113, 2009.

[88] Z. Liu, Y. Kang, X. Wu, and S. Yang, "Study on local magnetization of magnetic flux leakage testing for storage tank floors," *Insight - Non-Destructive Testing and Condition Monitoring,* vol. 45, pp. 328-331, 2003.

[89] N. Ida, *Microwave NDT*. Dordrecht: Kluwer Academic Publishers, 1992.

[90] S. I. Ganchev, J. Bhattacharyya, S. Bakhtiari, N. Qaddoumi, D. Brandenburg, and R. Zoughi, "Microwave diagnosis of rubber compounds," *IEEE Transactions on Microwave Theory and Techniques,* vol. 42, pp. 18-24, 1994.

[91] M. T. Ghasr, S. Kharkovsky, R. Zoughi, and R. Austin, "Comparison of Near-Field Millimeter-Wave Probes for Detecting Corrosion Precursor Pitting Under Paint," *IEEE Transactions on Instrumentation and Measurement,* vol. 54, pp. 1497-1504, 2005.

[92] M. T. Ghasr, S. Kharkovsky, R. Zoughi, M. O'Keefe, and D. Palmer, "Millimeter Wave Imaging of Corrosion under Paint: Comparison of Two Probes," in *Review of Quantitative Nondestructive Evaluation*, D. O. Thompson and D. E. Chimenti, Eds.: American Institute of Physics, 2006, pp. 447-454.

[93] J. Wilson, G. Y. Tian, I. Z. Abidin, S. Yang, and D. Almond, "Pulsed eddy current thermography: system development and evaluation," *Insight,* vol. 52, pp. 87-90, 2010.

[94] N. Ida, *Numerical Modelling for Electromagnetic Nondestructive Evaluation*. London: Chapman & Hall, 1995.

[95] N. Ida and W. Lord, "A finite element model for three-dimensional Eddy current NDT phenomena," *IEEE Transactions on Magnetics,* vol. 21, pp. 2635-2643, 1985.

[96] L. S. Udpa, N. Ida, J. R. Bowler, and T. Theodoulidis, "Chapter 4: Modeling of Electromagnetic Testing," in *Nondestructive Testing Handbook. Volume 5: Electromagnetic Testing*, Third Edition ed, S. S. Udpa and P. O. Moore, Eds. Columbus, OH: American Society for Nondestructive Testing, Inc., 2004.

[97] Y. Li, T. P. Theodoulidis, and G. Y. Tian, "Fast analytical method for pulsed eddy current evaluation," in *Proceedings of the 45th annual British conference on NDT* Stratford-upon-Avon, United Kingdom: British Institute of Non-Destructive Testing, 2006, pp. 1-12.

[98] M. Gramz and T. Stepinski, "Eddy current imaging, array sensors and flaw reconstruction," *Research in Nondestructive Evaluation,* vol. 5, pp. 157-174, 1994.

[99] J. Blitz, *Electrical and Magnetic Methods of Nondestructive Testing*. Bristol: IOP Publishing Ltd, 1991.

[100] S. Udpa, N. Ida, G. L. Fitzpatrick, T. Hiroshima, M. L. Mester, W. C. L. Shih, R. K. Stanley, and L. Udpa, "Chapter 5: Probes for Electromagnetic Testing," in *Nondestructive Testing Handbook. Volume 5: Electromagnetic Testing*, Third Edition ed, S. S. Udpa and P. O. Moore, Eds. Columbus, OH: American Society for Nondestructive Testing, Inc., 2004.

[101] COMSOL AB, *AC/DC Module User's Guide*, 2007.

[102] R. J. Ditchburn and S. K. Burke, "Planar Rectangular spiral coils in eddy-current non-destructive inspection," *NDT&E International,* vol. 38, pp. 690-700, 2005.

[103] S. M. Panas and A. G. Papayiannakis, "Eddy Currents in an Infinite Slab due to an Elliptic Current Excitation," *IEEE Transactions on Magnetics,* vol. 21, pp. 4328-4337, 1991.

[104] S. H. H. Sadeghi and A. H. Salemi, "Electromagnetic field distributions around conducting slabs, produced by eddy-current probes with arbitrary shape current-

carrying excitation loops," *IEE Proceedings Science, Measurement and Technology,* vol. 148, pp. 187-192, 2001.

[105] H. Lei, L.-Z. Wang, and Z.-N. Wu, "Integral Analysis of a Magnetic Field for an Arbitrary Geometry Coil With Rectangular Cross Section," *IEEE Transactions on Magnetics,* vol. 38, pp. 3589-3593, 2002.

[106] T. P. Theodoulidis and E. E. Kriezis, "Impedance evaluation of rectangular coils for eddy current testing of planar media," *NDT&E International,* vol. 35, pp. 407-414, 2002.

[107] J. O. Fava and M. C. Ruch, "Calculation and simulation of impedance diagrams of planar rectangular spiral coils for eddy current testing," *NDT&E International,* vol. 39, pp. 414-424, 2006.

[108] H. Tian, S. Yamada, M. Iwahara, and H. Watanabe, "Scratch Detection by Eddy-Current Testing with a High Lift-Off Height," *Journal of the Magnetics Society of Japan,* vol. 30, pp. 435-438, 2006.

[109] I. Mukriz, G. Y. Tian, and Y. Li, "3D transient magnetic field mapping for angular slots in aluminium," *Insight - Non-Destructive Testing and Condition Monitoring,* vol. 51 pp. 21-24, 2009.

[110] S. K. Burke and M. E. Ibrahim, "Mutual impedance of air-cored coils above a conducting plate," *Journal of Physics D: Applied Physics,* vol. 37, pp. 1857-1868, 2004.

[111] Y. L. Bihan, "Study on the transformer equivalent circuit of eddy current nondestructive evaluation," *NDT & E International,* vol. 36, pp. 297-302, 2003.

[112] G. Y. Tian, Z. X. Zhao, and R. W. Baines, "The research of inhomogeneity in eddy current sensors," *Sensors and Actuators A,* vol. 69, pp. 148-151, 1998.

[113] D. Lamtenzan, G. Washer, and M. Lozev, "Detection and Sizing of Cracks in Structural Steel Using the Eddy Current Method," U.S. Department of Transportation, Federal Highway Administration, 2000.

[114] A. Simm, Y. Li, G. Y. Tian, and T. Theodoulidis, "Verification of an eddy current probe magnetic field," in *NDT 2008* Macclesfield, Cheshire, UK: The British Institute of Non-Destructive Testing, 2008.

[115] R. A. Smith, J. M. Bending, L. D. Jones, T. R. C. Jarman, and D. I. A. Lines, "Rapid ultrasonic inspection of ageing aircraft," *Insight - Non-Destructive Testing and Condition Monitoring,* vol. 45, pp. 174-177, 2003.

[116] C. Abbate, M. Morozov, G. Rubinacci, A. Tamburrino, and S. Ventre, "A Probe Array for Fast Quantitative Eddy Current Imaging," in *Electromagnetic*

Nondestructive Evaluation (X). vol. 28, S. Takahashi and H. Kikuchi, Eds. Amsterdam: IOS Press, 2007, pp. 75-82.

[117] S. Tumanski and M. Stabrowski, "The magnetovision method as a tool to investigate the quality of electrical steel," *Measurement Science and Technology,* vol. 9, pp. 488-495, 1998.

[118] Z. Chen and K. Miya, "ECT Inversion Using a Knowledge-Based Forward Solver," *Journal of Nondestructive Evaluation,* vol. 17, pp. 167-175, 1998.

[119] Y. Z. He, M. C. Pan, F. L. Luo, and G. Y. Tian, "Pulsed eddy current imaging and frequency spectrum analysis for hidden defect nondestructive testing and evaluation," *NDT & E International,* vol. 44, pp. 344-352, 2011.

[120] A. Bernieri, L. Ferrigno, M. Laracca, and M. Molinara, "Crack shape reconstruction in eddy current testing using machine learning systems for regression," *IEEE Transactions on Instrumentation and Measurement,* vol. 57, pp. 1958-1968, 2008.

[121] R. Sikora and P. Baniukiewicz, "Reconstruction of Cracks from Eddy Current Signals Using Genetic Algorithm and Fuzzy Logic," in *Quantitative Nondestructive Evaluation* Brunswick, Maine (USA): American Institute of Physics, 2005.

[122] G. Panaitov, H.-J. Krause, and Y. Zhang, "Pulsed eddy current transient technique with HTS SQUID magnetometer of non-destructive evaluation," *Physica C: Superconductivity,* vol. 372-376, pp. 278-281, 2002.

[123] J. W. Wilson and G. Y. Tian, "3D magnetic field sensing for magnetic flux leakage defect characterisation," *Insight - Non-Destructive Testing and Condition Monitoring,* vol. 48, pp. 357-359, 2006.

[124] Y. Li, A. Simm, and G. Y. Tian, "Investigation of lift-off intersection characteristics in eddy current evaluation using magnetic camera," in *NDT 2008* Macclesfield, Cheshire, UK: The British Institute of Non-Destructive Testing, 2008.